Effects on Dopaminergic Neurons Are Secondary in COX-Deficient Locomotor Dysfunction in Drosophila

Yalgin, Cagri

2020-08-21

Yalgin , C , Rovenko , B , Andjelkovic , A , Neefjes , M , Oymak , B , Dufour , E , Hietakangas , V & Jacobs , H T 2020 , ' Effects on Dopaminergic Neurons Are Secondary in COX-Deficient Locomotor Dysfunction in Drosophila ' , iScience , vol. 23 , no. 8 , 101362 . https://doi.org/10.1016/j.is

http://hdl.handle.net/10138/319506
https://doi.org/10.1016/j.isci.2020.101362

iScience

CellPress
OPEN ACCESS

Article

Effects on Dopaminergic Neurons Are Secondary in COX-Deficient Locomotor Dysfunction in *Drosophila*

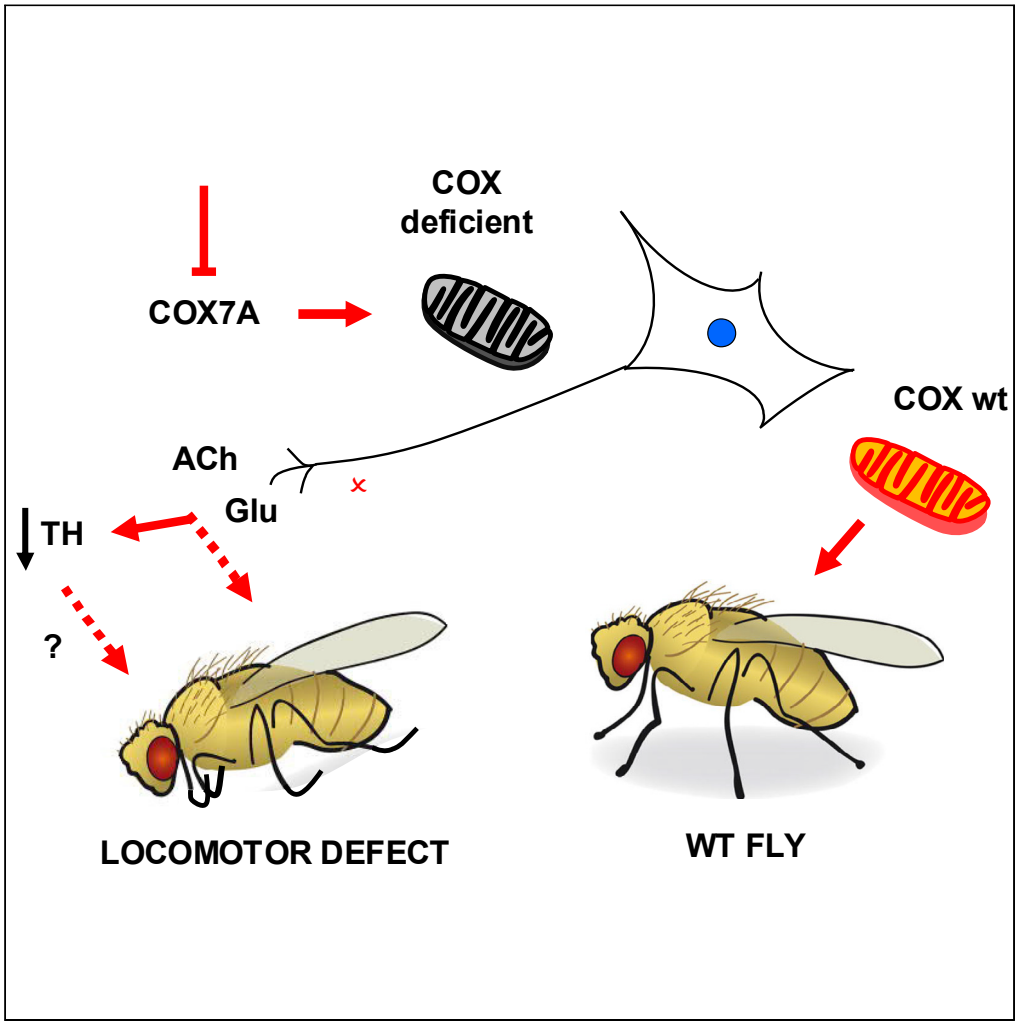

Cagri Yalgin, Bohdana Rovenko, Ana Andjelković, ..., Eric Dufour, Ville Hietakangas, Howard T. Jacobs

howard.jacobs@tuni.fi

HIGHLIGHTS

Neuronal knockdown of a COX subunit produces locomotor defect in flies

Specific subsets of cholinergic and glutamatergic (not DA) neurons are vulnerable

Decreased tyrosine hydroxylase is a secondary or side effect

Extensive neuronal cell death is not involved in the phenotype

Yalgin et al., iScience *23*, 101362
August 21, 2020
https://doi.org/10.1016/j.isci.2020.101362

iScience

CellPress
OPEN ACCESS

Article

Effects on Dopaminergic Neurons Are Secondary in COX-Deficient Locomotor Dysfunction in *Drosophila*

Cagri Yalgin,[1,2] Bohdana Rovenko,[2,3] Ana Andjelković,[1,4] Margot Neefjes,[1,2,5] Burak Oymak,[2,6] Eric Dufour,[1] Ville Hietakangas,[2,3] and Howard T. Jacobs[1,7,*]

SUMMARY

Dopaminergic (DA) neurons have been implicated as key targets in neurological disorders, notably those involving locomotor impairment, and are considered to be highly vulnerable to mitochondrial dysfunction, a common feature of such diseases. Here we investigated a *Drosophila* model of locomotor disorders in which functional impairment is brought about by pan-neuronal RNAi knockdown of subunit COX7A of cytochrome oxidase (COX). Despite minimal neuronal loss by apoptosis, the expression and activity of tyrosine hydroxylase was decreased by half. Surprisingly, COX7A knockdown specifically targeted to DA neurons did not produce locomotor defect. Instead, using various drivers, we found that COX7A knockdown in specific groups of cholinergic and glutamatergic neurons underlay the phenotype. Based on our main finding, the vulnerability of DA neurons to mitochondrial dysfunction as a cause of impaired locomotion in other organisms, including mammals, warrants detailed investigation.

INTRODUCTION

Mitochondrial stress, whether resulting from impaired respiration, oxidative damage, or defective protein quality control, has been proposed as a major underlying process in neurological diseases, notably those where locomotion is impaired, such as Parkinson's disease (PD; recently reviewed by Ge et al., 2020). The main pathological target in such diseases is dopaminergic (DA) neurons (Lees et al., 2009), and these are believed to be specifically sensitive to mitochondrial dysfunction (Bose and Beal, 2016), whether induced by toxins (Terron et al., 2018), genetic predisposition (Deng et al., 2018), or somatic accumulation of genetic damage, such as to mitochondrial DNA (Bender et al., 2006; Kraytsberg et al., 2006). Many questions remain open, as to why DA neurons are especially sensitive to mitochondrial dysfunction and how this results in loss of function and eventually produces disease.

The fruit fly *Drosophila melanogaster* has emerged as a useful animal model for studying pathological processes and possible treatment options for neurological disorders (Jeibmann and Paulus, 2009; McGurk et al., 2015), including the role of mitochondria (Guo, 2012). DA neurons in *Drosophila* have been implicated in a number of behavioral processes, including feeding, sleep, and locomotion, and fly models of locomotor dysfunction strongly support a role for mitochondrial stress in the phenotype.

In the *Drosophila* brain there are rather few DA neurons, mostly located in anatomically distinct clusters specified during embryogenesis (Hartenstein et al., 2017). Because of their functional and anatomical similarities with DA neurons in vertebrates, they are of great interest in the fields of neurodegeneration and other neurological disorders, both movement related and psychiatric (White et al., 2010). In addition to the panoply of genetic tools available to probe cellular and physiological processes in the fly, a number of simple, quantifiable behavioral paradigms are well established in *Drosophila*. Prominent among them is the negative geotaxis (climbing) assay, which has been widely used to measure locomotor competence in adults. It is frequently considered a marker for neurodegeneration, especially when used to score the effects of manipulating genes implicated in human neurodegenerative disease (Fernius et al., 2017). These include, for example, the Alzheimer-associated beta-amyloid peptide (Marcora et al., 2014), the familial PD gene *Pink1* (Guo, 2012), or the *Drosophila* homologue of *FUS* (*cabeza*), implicated in one form of ALS (Frickenhaus et al., 2015).

[1]Faculty of Medicine and Health Technology, FI-33014 Tampere University, Finland

[2]Institute of Biotechnology, FI-00014 University of Helsinki, Finland

[3]Faculty of Biological and Environmental Sciences, FI-00014 University of Helsinki, Finland

[4]Present address: Faculty of Biological and Environmental Sciences, FI-00014 University of Helsinki, Finland

[5]Present address: Department of Experimental Rheumatology, Radboud University Medical Center, 6500 HB Nijmegen, Netherlands

[6]Present address: Erzurum Regional Training and Research Hospital, Erzurum, Turkey

[7]Lead Contact

*Correspondence: howard.jacobs@tuni.fi

https://doi.org/10.1016/j.isci.2020.101362

In a previous study, we observed that pan-neuronal RNAi-mediated knockdown of various different subunits of cytochrome oxidase (COX, respiratory complex IV, cIV), the terminal enzyme of the mitochondrial respiratory chain, results in a severe locomotor impairment as measured by the negative geotaxis assay (Kemppainen et al., 2014). The phenotype was most severe when "core" subunits of the complex, such as COX4, were targeted, with all flies dying at the early larval stages. However, when peripheral subunit COX7A was targeted specifically, flies generally died as pupae, and even eclosed as adults if COX7A knockdown was confined to neurons, or if the alternative oxidase (AOX) from *Ciona intestinalis* was expressed to provide a metabolic bypass for cIV (Kemppainen et al., 2014; Andjelković et al., 2015).

The functional role of the COX7A subunit is not fully known, although it is clearly required for cIV assembly and full COX activity (reviewed by Mansilla et al., 2018). One mammalian paralog, Scafi (also known as COX7A-related protein, COX7RP, or COX7AL2), has been implicated in the formation of respiratory supercomplexes (Lapuente-Brun et al., 2013; Ikeda et al., 2013).

In addition to the canonical COX7A gene, the *Drosophila* genome has two homologs thereof, namely, COX7AL, expressed only in testis, and CG34172, expressed mainly in adult carcass and other muscle-containing tissues (heart, gut), with all three showing greater similarity to the two mammalian COX7A isoforms, COX7A1 (heart) and COX7A2 (liver) than to Scafi, and therefore considered as standard subunits of cIV. Given that CG34172 is only minimally expressed in the nervous system, combined with the specificity of available GAL4 drivers, this affords an opportunity to study the biological effects of neural knockdown of COX without having a major effect on muscle or any other tissues.

Given the prevailing view in the field that DA neurons are especially vulnerable to mitochondrial dysfunction, we set out to investigate how COX deficiency impacts them in the fly, taking as our starting point the previous observations on pan-neuronal COX7A knockdown (Kemppainen et al., 2014; Andjelković et al., 2015). Although we observed a clear decrease in the level of the key DA biosynthetic enzyme tyrosine hydroxylase (TH), these effects were found to be secondary in nature. Although such findings cannot be directly translated to mammals, they highlight the need to re-examine thoroughly the link between mitochondrial dysfunction, DA neuron degeneration, and locomotor impairment in other contexts.

RESULTS

Pan-Neuronal Knockdown of COX7A Decreases TH Expression in DA Neurons

We first confirmed the effectiveness of RNAi directed against COX7A, using VDRC (RRID:SCR_013805) line 106661 plus the pan-neuronal *elav-GAL4^{C155}* driver, in combination with *UAS-Dcr2* to potentiate its effects on locomotion. The driver and *UAS-Dcr-2* alone produced no locomotor impairment (Andjelković et al., 2015), so this was included as a control in the experiments to profile the effects of knockdown. Western blots showed that pan-neuronal COX7A knockdown resulted in an ~50% decrease in the amount of COX4 protein in fly heads (Figure S1A), a proxy for assembled cIV, and a similar decrease in respiratory function (Figure S1B), showing clearly that the phenotype obtained is associated with mitochondrial dysfunction.

Previous studies (Kemppainen et al., 2014) found no gross anatomical abnormalities from COX knockdown during development, implying that it does not result in substantial cell death. To profile ongoing cell death in the brains of flies with pan-neuronal COX7A knockdown, we used two approaches. TUNEL staining revealed a very low number of apoptotic cells, despite strong signals in the positive control (Figure S1C). However, although low, the number of TUNEL-positive cells in knockdown brains was significantly higher than in controls (Figure S2A) and included both neuronal and glial cells (Figure S2B). Using the Apoliner reporter system (Bardet et al., 2008), in which apoptotic cells are marked by the nuclear translocation of GFP, we observed only very few such examples (Figures S3 and S4). We also observed no increase in signal compared with controls, when knockdown brains were stained with dihydroethidium (Figure S5) as a crude marker for superoxide production.

Pan-neuronal COX7A knockdown produced no obvious difference in the number of TH-positive neurons but nevertheless revealed a marked decrease in TH signal (Figure 1A). To quantify the effect, we focused on a specific cluster of DA neurons, the PAL (protocerebral anterior lateral) cluster, avoiding issues arising from the differing signal intensities from different such clusters (Mao and Davis, 2009). The average signal intensity, whether computed per brain or per cell (Figure 1B), showed a significant (~50%) decrease in

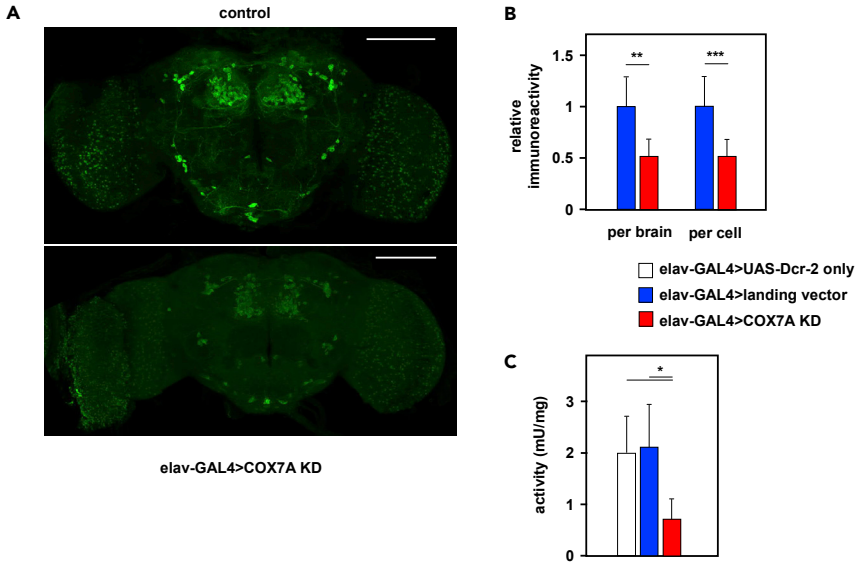

Figure 1. Pan-Neuronal Knockdown of COX7A Leads to TH Deficiency

(A) Immunohistochemistry for TH on brains from male flies with and without pan-neuronal knockdown of COX7A (representative images). Genotypes as follows–control (designated as elav-GAL4>landing vector in B and C): *elav-GAL4^{C155}*, *UAS-Dcr-2* / Y; *P{attP, y^{+}, w^{3}}/+*. elav-GAL4>COX7A KD: *elav-GAL4^{C155}*, *UAS-Dcr-2* / Y; *UAS-RNAi^{COX7A}* / +, where *UAS-RNAi^{COX7A}* denotes the dsRNA-encoding insertion in VDRC line 106661. Rabbit anti-TH antibody, 1:500, used with Alexa 488 goat anti-rabbit secondary antibody, 1:500. Scale bars, 100 μm. Note that batches of control and knockdown brains were processed in parallel using the same reagents. Counterstaining for Elav (Figure S6) indicated that low TH signal was not due to a general issue with antibody penetration. The range of staining intensities likely reflects both technical variability in sample preparation and visualization, as well as biological variation.

(B) Quantitation of TH signal from immunohistochemistry on multiple specimens of the types shown in (A). Signal was quantitated in dopaminergic neurons of the PAL (protocerebral anterior lateral) cluster and plotted as mean signal intensity (±SD) for each brain (left-hand columns: elav-GAL4>landing vector controls, n = 4, elav-GAL4>COX7A KD, n = 8) or for each analyzed cell considered as a separate data point (right-hand columns: elav-GAL4>landing vector, n = 11, elav-GAL4>COX7A KD, n = 27). Note that all flies also carried *UAS-Dcr-2*. The PAL cluster was selected, being easily identified, close to the anterior surface of the brain, and comprising only a few cells.

(C) TH activity from extracts of female fly heads of the indicated genotypes: elav-GAL4>UAS-Dcr-2 only – *elav-GAL4^{C155}*, *UAS-Dcr2*, elav-GAL4>landing vector – *elav-GAL4^{C155}*, *UAS-Dcr-2*; *P{attP, y^{+}, w^{3}}* / + and elav-GAL4>COX7A KD – *elav-GAL4^{C155}*, *UAS-Dcr-2*; *UAS-RNAi^{COX7A}*/+.

Significant differences (Student's t test or, where more than two classes were compared, one-way ANOVA with Tukey *post hoc* HSD test) denoted as *, **, and ***, representing $p < 0.05$, 0.01, and 0.001, respectively. See also Figures S1–S5 for validation of knockdown and its effects and Figure S6 for validation of immunohistochemistry.

knockdown brains. TH activity, measured in protein extracts from isolated heads, showed a similar decrease (Figure 1C). Decreased TH activity in knockdown brains is consistent with a specific effect on DA neurons.

Locomotor Defect Is Caused by COX7A Knockdown in Specific Groups of Neurons

To test whether DA neurons are the functionally relevant target in generating locomotor defect by COX7A knockdown, we used the drivers *TH*-GAL4, which selectively targets DA neurons, *Ddc*-GAL4, which targets both serotonergic and DA neurons, and *TRH*-GAL4, specific for serotonergic neurons. To ensure effective knockdown, we included *UAS-Dcr-2* in all knockdown experiments. As negative controls we combined *UAS-Dcr-2* with each driver (except for *elav*-GAL4, which was included here as a positive control). Neither of the DA drivers (nor the one targeting only serotonergic neurons) gave a significant locomotor defect (Figure 2A). Using a wider selection of drivers (Figure 2B), we observed a significant locomotor defect when COX7A knockdown was driven by *Cha*-GAL4 (cholinergic neurons) or by OK371 (glutamatergic neurons) but not by *acj6*-GAL4 (Figures 2B and 3A), targeting a restricted group of cholinergic neurons (Lee and Salvaterra, 2002). Drivers targeting GABAergic or octopaminergic neurons or glia also had no effect on locomotor activity (Figure 2B).

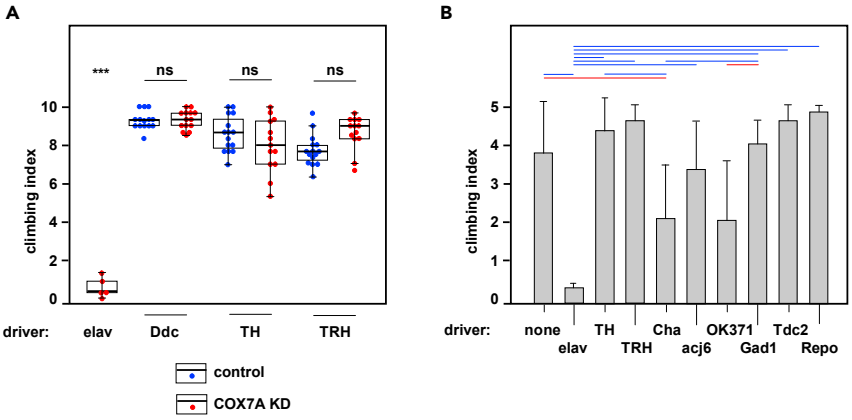

Figure 2. Locomotor Impairment Is due to COX7A Knockdown in Neurons of Specific Neurotransmitter Identities

Climbing index for COX7A-KD flies derived by crossing the indicated GAL4 driver or control males (homozygous or balanced, as indicated in Transparent Methods) to *UAS-RNAi*^{COX7A}; *UAS-Dcr-2* females or (A, controls) to *UAS-Dcr-2* females without the RNAi construct.

(A) Boxplots indicate medians (bold lines), 25th and 75th percentiles (box limits), and 1.5 times the interquartile range (Tukey-style whiskers, truncated where they would cross the zero or maximum lines) for batches of 10 virgin female flies. Colored dots represent individual data points for each batch (means of three tests) as indicated. Significant differences (one-way ANOVA with Tukey *post hoc* HSD test), indicated as ***, $p < 0.001$ for comparison with all other data classes, ns, $p > 0.05$ for the pairwise comparisons indicated. Other comparisons omitted for clarity. Note that the *elav*-GAL4 driver was included here as a positive control.

(B) Means $\pm$ SD ($n \geq 4$, except for *repo*-GAL4, $n = 3$) for batches of five virgin female flies. Statistical analysis (one-way ANOVA with Tukey *post hoc* HSD test; significant differences indicated by red and blue bars, denoting $p < 0.05$ and $p < 0.01$, respectively. For repeat experiments using *Cha*-GAL4 and OK371 drivers, alongside *UAS-Dcr-2* controls, see Figures 3B and 3C. Note that *TH*-GAL4 drives expression only poorly, if at all, in a small subset of DA neurons that are, conversely, targeted by *Ddc*-GAL4 (Riemensperger et al., 2013); both drivers are therefore needed to cover all DA neurons. Based on GFP controls, drivers were active in cells of the predicted identity (Figures S7–S9), although the *TRH*-GAL4 driver did drive expression in a small number of TH-positive (i.e., DA) neurons (Figure S9B). Effects in DA neurons were not simply delayed (see Figure S10).

Using GFP as a reporter we observed that the *Cha*-GAL4 driver is not fully specific for cholinergic neurons (see Figures S11–S13). We therefore proceeded to test additional drivers, incorporating only fragments of the *ChAT* gene, to identify more restricted subsets of cholinergic neurons responsible for the locomotor phenotype and confirm their neurotransmitter identities. Given the large number of neurons targeted by OK371 (Figure S14), we took a similar approach to narrow down the susceptible glutamatergic neurons, using drivers incorporating fragments from the *VGlut* gene. We identified strong candidates from both sets (Figure 3A) and confirmed them against *UAS-Dcr-2* controls (Figures 3B and 3C). In summary, the locomotor defect produced by neuronal knockdown of COX7A is dependent on restricted subsets of cholinergic and glutamatergic neurons, rather than on DA neurons as initially assumed.

Several Largely Non-overlapping Sets of Neurons Are Susceptible to COX7A Knockdown

For further study we selected the two cholinergic (R55A05 and R59E04) and the two glutamatergic drivers (R52A01 and R51C09) giving the strongest locomotor impairment. The expression patterns of these drivers are already known and were verified using fluorescent reporters before proceeding. Expression driven by the cholinergic driver R55A05 labeled a number of specific brain structures (Figures 4A and 4B), with widespread colocalization with ChAT, although in some brain regions the ChAT signal was very weak. There was no convincing colocalization with TH or other specific neural markers (see Figures S16 and S17). The second cholinergic driver (R59E04) exhibited an almost completely distinct expression pattern (Figures 4C and S18), with variable and incomplete colocalization with ChAT (Figures 4C and S19), and no overlap with TH (see Figure S20).

The two selected glutamatergic drivers showed limited expression in the brain (Figures 5 and 6), most prominently in the optic lobe (Figures 5A and 6A). Because motoneurons are glutamatergic in *Drosophila*, we investigated whether they were targets of either driver, by examining the subcuticular neurons of the larval PNS, where motoneurons are easily distinguished. R51C09 directed expression in a pair of prominent

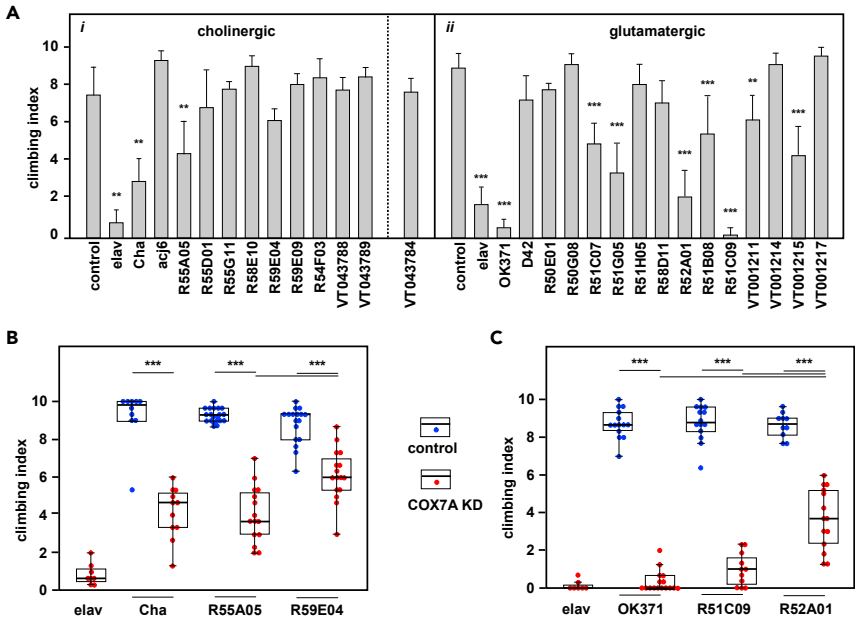

Figure 3. Locomotor Impairment due to COX7A Knockdown in Specific Sub-groups of Cholinergic and Glutamatergic Neurons

Climbing index for COX7A-KD flies derived by crossing the indicated GAL4 drivers, from the FlyLight (Jenett et al., 2012) and Vienna Tiles collections (Tirian and Dickson, 2017), or control males to *UAS-RNAi*^{COX7A}; *UAS-Dcr-2* females or (B, controls) to *UAS-Dcr-2* females without the RNAi construct.

(A) Means ± SD ($n \geq 4$) for batches of 10 virgin female flies. Significant differences (one-way ANOVA with Tukey *post hoc* HSD test) indicated as *, **, and ***, denoting $p < 0.05$, 0.01, and 0.001, respectively, in comparison with controls. Other comparisons omitted for clarity. (i) and (ii) represent separate series of experiments for cholinergic and glutamatergic drivers, as indicated. As denoted by the dotted line, for logistical reasons, experiments with the cholinergic VT043784 driver were performed and analyzed together with those using the glutamatergic drivers shown in (ii).

(B and C) Boxplots for selected (B) cholinergic and (C) glutamatergic drivers, using the same conventions and statistical analyses as in Figure 2A.

axons, repeating in each hemisegment of the trunk (Figure 5C). Their cell bodies were absent, consistent with their being motoneurons, since motoneuron cell bodies lie in the ventral nerve cord, which was removed in the dissection of the larvae. R52A01 also directed expression in prominent subcuticular neurons repeating in each hemisegment (Figure 6C). As the cell bodies of these neurons were present in the dissected larvae, they cannot be motoneurons and are almost certainly sensory neurons. Using a dual-reporter system we confirmed that there was very little overlap in the brain-expression patterns of the two selected cholinergic drivers or the two selected glutamatergic drivers (see Figures S23 and S24). We conclude that locomotor impairment can be brought about by mitochondrial dysfunction in any of several largely independent sets of neurons.

Only a Minor Fraction of COX7A Knockdown-Sensitive and DA Neurons Interact Directly

Based on the above findings, the neurons vulnerable to mitochondrial dysfunction are not dopaminergic, even though TH was depleted by pan-neuronal knockdown of COX7A. This raises the possibility that DA neurons and those sensitive to COX7A knockdown are part of the same neural circuits controlling locomotion. Consistent with this, dendritic projections from sensitive cholinergic neurons are found in the same areas of the brain as those from TH-positive neurons (Figures S25 and S26), although this does not demonstrate direct interaction. Moreover, using the *trans*-Tango reporter system (Talay et al., 2017), we found only a very low proportion of TH-positive neurons connected post-synaptically to those targeted by the R55A05 driver (Figure 7, Figures S27–S31, Video S1), and this did not include any of the prominent clusters of DA neurons where the loss of TH signal was quantified in earlier experiments. Any connections between the cholinergic neurons targeted by this driver and major groups of DA neurons involved in locomotor functions must therefore be indirect.

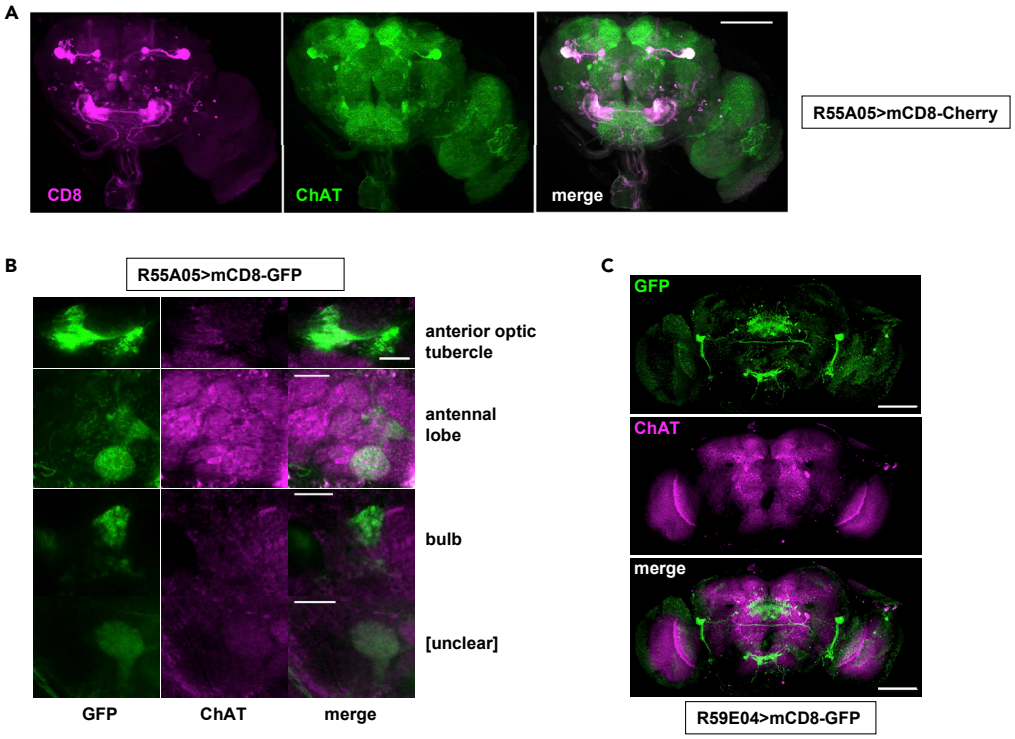

Figure 4. Neuronal Targets of GAL4 Drivers R55A05 and R59E04

Immunohistochemistry of brains from individual flies expressing mCD8 reporters under the control of the GAL4 drivers indicated.

(A) Single optical section co-stained for CD8 (rat anti-CD8, 1:200, followed by Alexa 568 goat anti-rat) and ChAT (mouse anti-ChAT, 1:100, followed by Alexa 488 goat anti-mouse). Scale bar, 100 μm. For equivalent maximum intensity projection of the whole brain stained for CD8, see Figure S15.

(B) Higher magnification of some specific brain regions co-stained for GFP (rabbit anti-GFP, 1:1,000, followed by Alexa 488 goat anti-rabbit) and ChAT (mouse anti-ChAT, 1:100, followed by Alexa 647 goat anti-mouse). Scale bar, 20 μm. These are maximum intensity projections compiled from a few adjacent optical sections, sufficient to reveal the shapes of the co-stained structures. The fourth structure (marked "[unclear]") shows a structure that we were unable to identify with confidence from Virtual Fly Brain (v2.virtualflybrain.org). Note that, because overlap appeared so extensive in the first experiment (Figure 4A), we here combined a green and a far-red fluor to minimize any possible bleeding between channels.

(C) Maximum intensity projection stained for GFP (rat anti-CD8, 1:200, followed by Alexa 647 goat anti-rat) and for ChAT (mouse anti-ChAT, 1:100, followed by Alexa 488 goat anti-mouse). Scale bar, 100 μm. See also Figures S16–S20: note that these two drivers targeted largely non-overlapping sets of cholinergic neurons, whereas neither was active in DA neurons.

Apoptosis of Neurons Sensitive to COX7A Knockdown Is Lethal

Although we found no evidence of widespread cell death in the brains of adult COX7A knockdown flies, this does not exclude death of vulnerable neurons during development. To test this, we set up crosses using males from each of the selected driver lines mated with balanced females expressing Hid, a potent inducer of apoptosis (Sandu et al., 2010), under GAL4 control (see Transparent Methods). In the case of all four selected drivers, all eclosing progeny carried the balancer markers. Therefore, the death of the targeted cells is developmentally lethal, excluding widespread neuronal death as the mechanism by which COX7A knockdown results in locomotor impairment.

TH Deficiency Does Not Correlate with Locomotor Defect in COX7A Knockdown Flies

Given that the connections between targeted and DA neurons appear to be mostly indirect, we tested whether the TH deficiency produced by pan-neuronal COX7A knockdown could be recapitulated by targeting COX7A knockdown to specific groups of neurons, using the selected drivers. The R55A05 GAL4 driver gave, at most, a modest, diminution of TH signal (Figure 8), whereas that produced by the R59E04 driver, with a weaker locomotor effect, was generally more pronounced (Figure 8). Similar findings were obtained using the glutamatergic drivers (Figure 9). These findings imply that TH deficiency and impaired

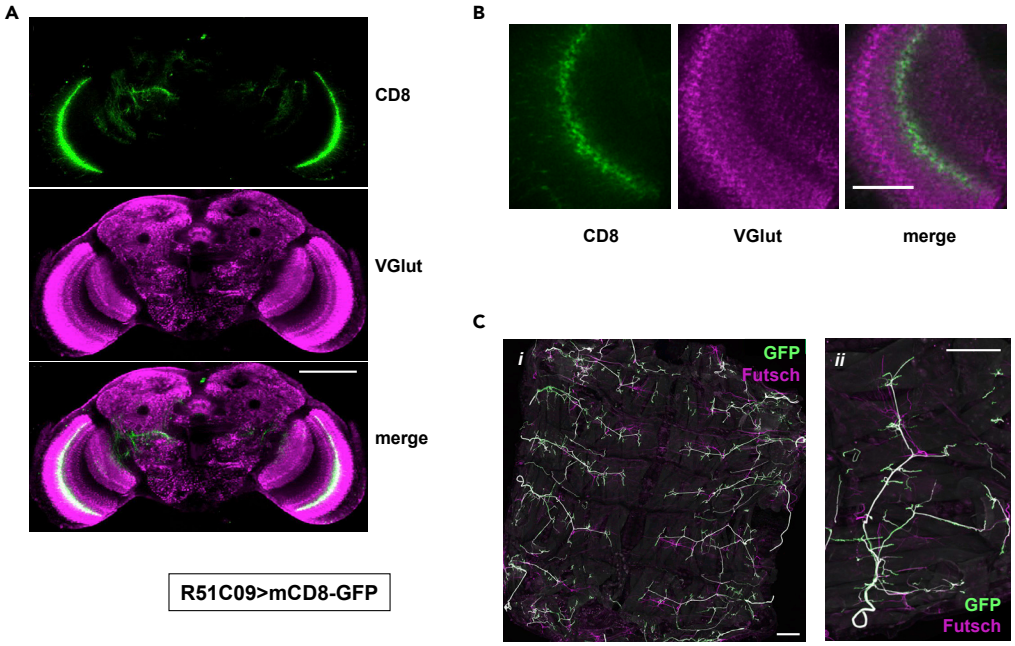

Figure 5. Neuronal Targets of GAL4 Driver R51C09

Immunohistochemistry of (A) whole brains and (B) portion of optic lobes from adult females, and (C) larval subcuticular neurons, from *Drosophila* expressing mCD8-GFP under the control of GAL4 driver R51C09.

(A and B) Single optical sections of samples co-stained for CD8 and VGlut. Scale bar, 100 μm in (A) and 20 μm in (B).

(C) Maximum intensity projections of samples co-stained for GFP and the microtubule-binding protein Futsch. (*i*) Low magnification, anterior to the top, dorsal midline in the middle. (*ii*) Higher magnification, dorsal side to the top, anterior to left. Scale bars, 200 μm. Note that there was no colocalization with GABA or TH (Figure S21).

locomotion are not strictly correlated and suggest that TH deficiency may not be systematically instrumental in the behavioral phenotype.

DISCUSSION

In this study we showed that several groups of susceptible cholinergic and glutamatergic neurons, but not dopaminergic (DA) neurons, underlie the locomotor impairment brought about by RNAi-mediated knockdown of a subunit of cytochrome *c* oxidase in the *Drosophila* nervous system. This challenges the widely held assumption that DA neurons are key targets of mitochondrial dysfunction, leading to impaired locomotor function, at least in the fly.

Mitochondrial Dysfunction in Specific Cholinergic and Glutamatergic Neurons Is Instrumental in Locomotor Impairment

Pan-cholinergic and pan-glutamatergic COX knockdown both produced a severe locomotor phenotype. We used drivers targeting much more restricted subsets of neurons to narrow down this vulnerability and exclude cells with other neurotransmitter identities. However, the two cholinergic drivers giving significant locomotor impairment had almost completely non-overlapping expression profiles, with the one showing the stronger effects (R55A05) expressed in numerous brain regions. Thus, it is not yet possible to say which such regions are the more critical. On the glutamatergic side, the two strongest drivers also showed only partially overlapping expression patterns in the brain (Figures 5 and 6), with prominent expression also in different cells of the larval peripheral nervous system (PNS), one in motoneurons (Figure 5C) and the other in a subclass of sensory neurons (Figure 6C). Note also that COX7A knockdown driven by D42, which targets at least some adult motoneurons (Yeh et al., 1995; Sanyal et al., 2003), gave no such phenotype (Figure 3A). Locomotor impairment may therefore be due to mitochondrial dysfunction in a variety of specific cells in the brain, PNS or both, in diverse combinations.

Our study illustrates the limitations of the widely used negative geotaxis assay, in that a similar locomotor impairment can be independently produced by a primary defect in any of a number of distinct subsets of

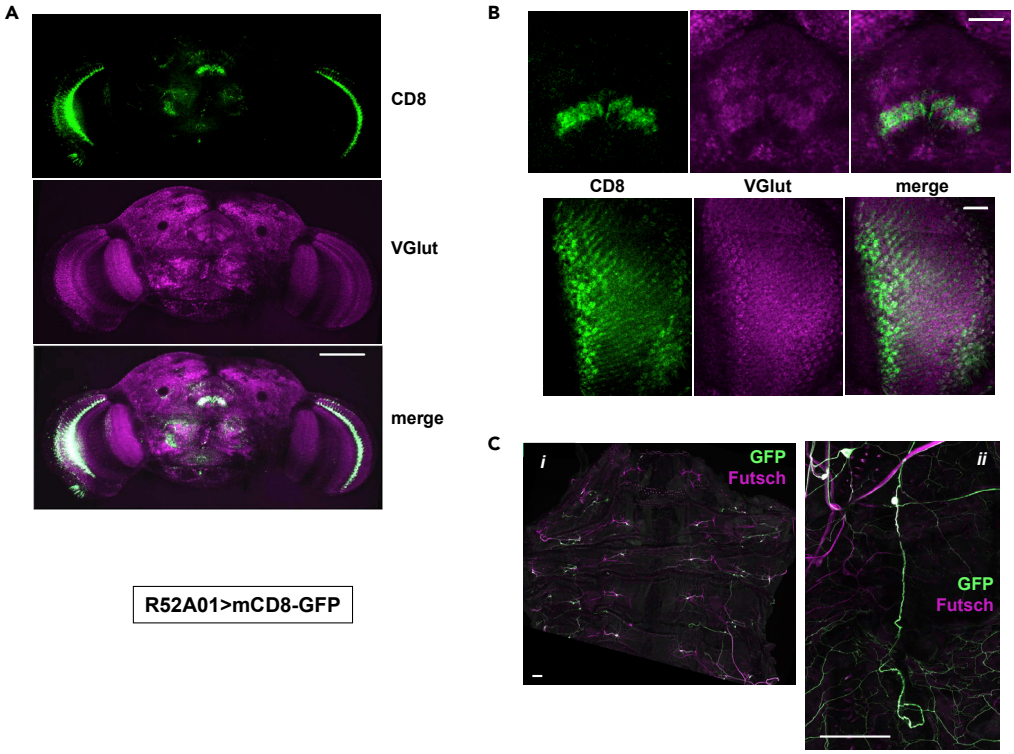

Figure 6. Neuronal Targets of GAL4 Driver R52A01

Immunohistochemistry of (A) whole brains and (B) selected brain areas from adult females, and (C) larval subcuticular neurons, from *Drosophila* expressing mCD8-GFP under the control of GAL4 driver R52A01.

(A and B) Single optical sections of samples co-stained for CD8 and VGlut. Scale bar, 100 μm in (A) and 20 μm in (B).

(C) Maximum intensity projections of samples co-stained for GFP and the microtubule-binding protein Futsch. (*i*) Low magnification, anterior to the top, dorsal midline in the middle. (*ii*) Higher magnification, dorsal side to the top, anterior to left. Scale bars, 100 μm. Note that there was no colocalization with GABA or TH (Figure S22).

neurons, with different functions and neurotransmitter identities, possibly not involving a uniform molecular mechanism. Experiments using the assay should therefore be interpreted with caution. The current study also prompts an analysis of a broader range of behavioral phenotypes in flies with neuronal COX deficiency.

Effects on DA Neurons

Ddc-GAL4 and *TH*-GAL4 most strongly target different subsets of DA neurons (Riemensperger et al., 2013), but neither was able to produce locomotor impairment when used to drive COX7A knockdown. This contrasts with the findings of Riemensperger et al. (2013), who found that the expression of the PD-associated human α-synuclein A30P variant produced a locomotor defect when expressed using the *Ddc*-GAL4 but not the *TH*-GAL4 (or *TRH*-GAL4) drivers. Although we cannot exclude that simultaneous COX deficiency in both groups of DA neurons is required to produce locomotor impairment, we did not detect TH-positive cells among those targeted by any of the four drivers that did produce the phenotype. Therefore, it is highly unlikely that COX deficiency in DA neurons contributes cell-autonomously to a locomotor phenotype, except perhaps in very aged flies.

Pan-neuronal COX7A knockdown did lead to a deficiency of TH, but its relationship to locomotor impairment is unclear. Although a non-cell-autonomous impairment of DA neuron function is a plausible explanation for our findings, TH deficiency might also be a secondary effect of dysfunction in relevant circuits that is not instrumental in the locomotor phenotype. Consistent with this, the individual drivers tested had varying and more subtle effects on TH levels (Figures 8 and 9). The two phenotypes (TH deficiency and impaired locomotion) are thus not tightly correlated.

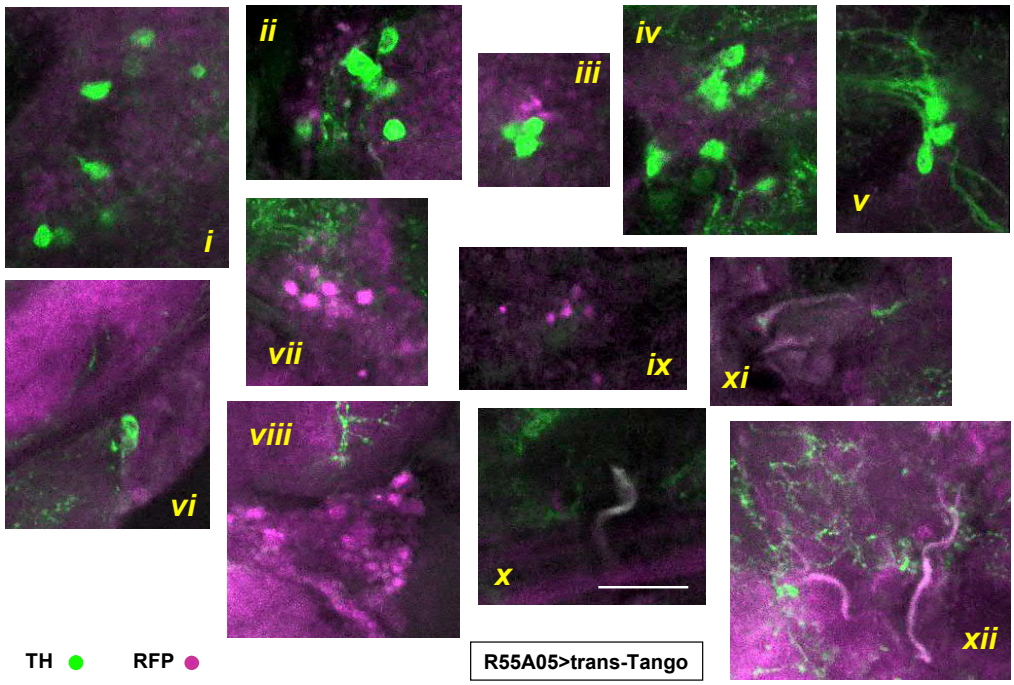

Figure 7. A Minor Fraction of R55A05 Post-synaptic Neurons Are Dopaminergic

Immunohistochemistry for TH (green, 1:500) and RFP (magenta) from brain of a female fly post-synaptically expressing RFP under the control of trans-Tango, driven by R55A05. Genotype: *UAS-myrGFP, QUAS-mtdTomato-3xHA* / +; *trans-Tango* / +; *R55A05-GAL4* / +. Zoomed images from individual optical sections; scale bar, 20 μm (all images to same scale). Images optimized for brightness and contrast but not manipulated in any other way. Overlap signals (white, pale magenta, and pale green, panels *viii*, *x–xii*) represent only a small minority of cells, not including (panels *i–vi*) the major clusters of DA neurons. Nevertheless, strong post-synaptic signals are seen both in TH-negative cell bodies (panels *ii*, *iii*, *viii*, *ix*) and in regions with abundant neurites (panels *vi–viii*, *xii*). For side-by-side comparisons of signals from the separate channels see Figures S27–S29. For the whole brain images from which these panels were derived, see Video S1 and Figures S30 and S31.

Locomotor Effects of Mitochondrial Dysfunction Are Not Mediated by DA Neuronal Death

We were unable to detect a prominent signature of cell death associated with pan-neuronal knockdown of COX7A. Moreover, there was no obvious difference in the number of PAL neurons, in contrast to the findings of Humphrey et al. (2012). Although we might have missed a very small decrease in the number of DA neurons, it is unlikely to account for the severe locomotor impairment produced. Although long-term loss of inputs to these neurons may result in their eventual loss, our data implicate COX deficiency in other group of neurons, not DA cell death, as the underlying cause of locomotor impairment.

Comparison with Previous Studies of Mitochondrial Dysfunction in DA Neurons

Our findings contrast with previous reports of progressive DA-cell loss and impaired locomotion, when a mitochondrial insult was targeted to DA neurons using the same *TH*-GAL4 driver as here (Humphrey et al., 2012), involving RNAi against the catalytic subunit of the mitochondrial DNA polymerase, Polγ (*tamas*). Conversely, applying *Cha*-GAL4 produced no such phenotype, whereas in the current report, RNAi against a subunit of cIV produced an opposite result. The discrepancy with our findings could have various explanations, which need to be explored in future studies.

First, the phenotype described by Humphrey et al. (2012) is a progressive one with late onset. *tamas* knockdown flies initially showed only a very mild degree of locomotor impairment, but that steadily worsened during adult life, whereas COX7A knockdown had dramatic (but stable) effects in young adult flies. The two phenotypes studied, i.e., age-related neurodegeneration and developmental locomotor impairment, are fundamentally different and may be produced by entirely different mechanisms. Note that most cases of heritable mitochondrial dysfunction affecting the CNS in humans manifest in infancy and are often fatal within the first weeks or months of life (Gorman et al., 2016).

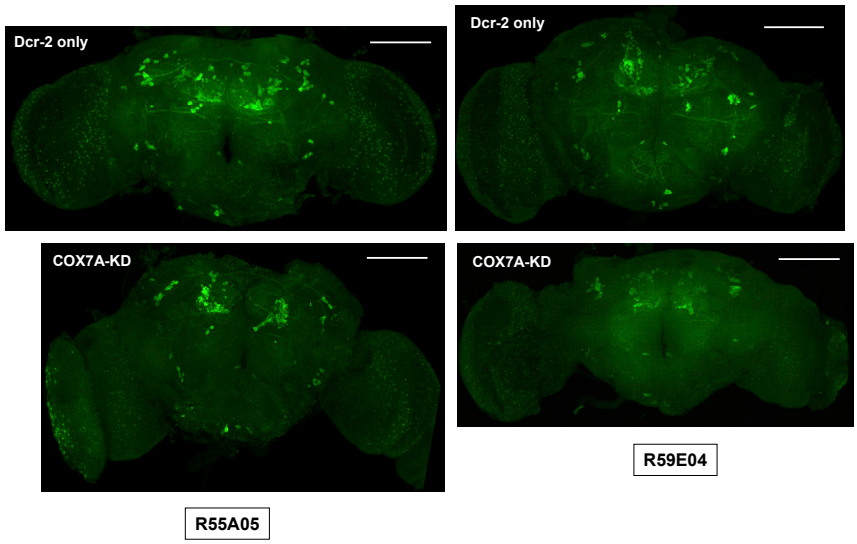

Figure 8. TH Deficiency Resulting from COX7A Knockdown in Subsets of Cholinergic Neurons

Immunohistochemistry for TH (1:500) in brains from flies with COX7A knockdown or controls with only Dcr-2 overexpression, as indicated, using the GAL4 drivers shown (maximum intensity projections). Genotypes – Dcr-2 only: +; *R55A05-GAL4* (or *R59E04-GAL4*)/*UAS-Dcr-2*, COX7A-KD: *UAS-RNAi*^{COX7A} / +; *R55A05-GAL4* (or *R59E04-GAL4*)/*UAS-Dcr-2*. Scale bars, 100 μm. Contrast and brightness have been similarly adjusted in each image, giving uniform background fluorescence. See Figures S32–S35 for these and images of other brains from flies of the same genotypes, alongside images showing counter-stain for Elav.

Second, *tamas* and COX7A knockdown should result in quite distinct metabolic effects. The latter results in a clear but isolated deficiency of cytochrome oxidase, whereas the former should produce mtDNA depletion, affecting all four enzymatic components of the oxidative phosphorylation (OXPHOS) system that are dependent on mtDNA-encoded gene products. Different classes of neuron may have quite distinct susceptibilities to these different metabolic stresses. AOX expression in the Polγ model (Humphrey et al., 2012) also had much less dramatic effects than in the COX7A model (Kemppainen et al., 2014; Andjelković et al., 2015).

Finally, in a different study (Bahhir et al., 2019), stress imposed upon mtDNA by the ubiquitous expression of a bacterial type I restriction endonuclease produced a range of metabolic abnormalities unrelated to OXPHOS, including decreased levels of dopamine, and accompanying behavioral changes, notably in feeding. Dietary supplementation with L-DOPA restored wild-type feeding behavior and delayed the onset of lethality in the model. Although the detailed mechanism of the effect remains to be elucidated, mitochondrial dysfunction and its effects on DA-producing cells clearly should not be considered as a single, "all or none" phenomenon.

Possible Relevance to Neurological Disease

Owing to the involvement of mitochondrial gene products and toxin targets in human neurological disease, combined with the evidence for DA neuron degeneration as a pathomechanism in progressive locomotor disorders, it is widely assumed that DA neurons are particularly vulnerable to mitochondrial dysfunction. Although our study may not be directly translatable to the human context, relates to only one component of the OXPHOS system (cIV), and concerns a developmental rather than a degenerative phenotype, neurological involvement is a common feature of early-onset mitochondrial disease (Gorman et al., 2016). Our findings indicate that the direct neuronal targets of mitochondrial dysfunction leading to locomotor impairment, at least in early-onset disease, may not be DA neurons, but some other class of neural cells, with any effects on DA neurons being secondary to the underlying defect. Mitochondrial dysfunction has also been widely proposed as an instrumental factor in a variety of neurodegenerative diseases (Smith et al., 2019; Lim et al., 2020). Neuronal classes other than DA neurons have recently been implicated in neurodegenerative disease in humans (Liu, 2020). Our findings provide a possible model whereby mitochondrial dysfunction in such cells might be an underlying factor in the pathology, operating long before overt neurodegeneration manifests.

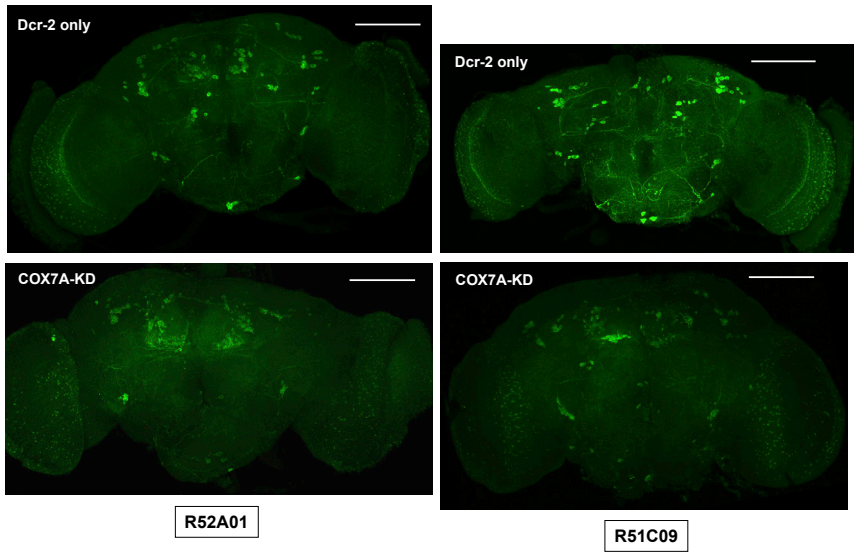

Figure 9. TH Deficiency Resulting from COX7A Knockdown in Subsets of Glutamatergic Neurons

Immunohistochemistry for TH (1:500) in brains from flies with COX7A knockdown or controls with only Dcr-2 overexpression, as indicated, using the GAL4 drivers shown (maximum intensity projections). Genotypes – Dcr-2 only: +; *R52A01-GAL4* (or *R51C09-GAL4*)/*UAS-Dcr-2*, COX7A-KD: *UAS-RNAi*^{COX7A} / +; *R52A01-GAL4* (or *R51C09-GAL4*)/*UAS-Dcr-2*. Scale bars, 100 μm. Contrast and brightness have been similarly adjusted in each image, giving uniform background fluorescence. See Figures S36–S39 for these and images of brains from flies of the same genotypes, alongside images showing counterstain for Elav.

Drosophila has proven to be a useful model for understanding fundamental biological processes in animals, such as the axial patterning of the nervous system (Estacio-Gómez and Díaz-Benjumea, 2014) or circadian behavior (Dubowy and Sehgal, 2017). In this light, and considering the conserved metabolism and function of DA neurons, it would be appropriate to re-examine this vulnerability to mitochondrial dysfunction of DA and other classes of neuron in other organisms, including mammals, and to test the effects of different types of mitochondrial insult, bearing in mind that the neuroanatomical differences (e.g., in size) between fly and mammalian brains may dictate a distinct outcome.

Limitations of the Study

As discussed above, the study was conducted on a single model organism (*Drosophila melanogaster*), using only one, albeit common, type of mitochondrial dysfunction, COX deficiency, here resulting from knockdown of a COX subunit. It focused on a single behavioral readout, locomotor impairment, and was concerned only with an intrinsic, developmentally determined, neural phenotype, rather than with age-related degeneration. Finally, although excluding a widely assumed mechanism whereby mitochondrial dysfunction results in locomotor impairment (i.e., a cell-autonomous effect in DA neurons), it leaves open the molecular mechanism(s) that do operate here.

Resource Availability

Lead Contact

Further information and requests for resources and reagents should be directed to and will be fulfilled by the Lead Contact, Howard T. Jacobs (howard.jacobs@tuni.fi).

Materials Availability

The study did not generate any new, unique reagents. All materials used in the work were sourced from public or commercial resources (*Drosophila* stock centers, antibody suppliers, manufacturers of standard laboratory equipment and reagents), as described under Transparent Methods (see Supplemental Information). If any such reagents or strains should become unavailable from these sources, the authors will be happy to assist in procuring them elsewhere, as far as they are able.

Data and Code Availability

This study did not generate or use any new datasets or machine code. All of the primary experimental data used in compiling this paper are included in the figures and Supplemental Information. For images presented here as maximum projections, the original image stacks are available upon request, although they do not provide any salient additional information relevant to the study.

METHODS

All methods can be found in the accompanying Transparent Methods supplemental file.

SUPPLEMENTAL INFORMATION

Supplemental Information can be found online at https://doi.org/10.1016/j.isci.2020.101362.

ACKNOWLEDGMENTS

We thank Serge Birman for the supply of the *TH*-GAL4 line; Hermann Aberle for providing the anti-VGlut antibody; Mikko Airavaara, Kira Holmström, Marten Szibor, Ying Liu, Tapio Heino, and Moussa Youdim for advice and fruitful discussions; Tea Tuomela, Eveliina Teeri, Anna Kuukasjärvi, and Lyon Bruinsma for technical assistance; Troy Faithfull for critical reading of the manuscript; and University of Helsinki LMU core facility for providing facilities for imaging. This work was supported by the Academy of Finland (Centre of Excellence grant 272376; Academy Professorship grant 283157 to H.T.J.; Centre of Excellence in Stem Cell Metabolism grant 312439 to V.H.); the French Muscular Dystrophy Association (AFM-Téléthon), grant no.19981 to C.Y.), the Finnish Cultural Foundation (grant 00181201 to C.Y. and 00160101 to A.A.), the Scientific Research Projects Coordination Unit of Pamukkale University (grant no. 2018TIPF034 to B.O.), Tampere University, and the Sigrid Jusélius Foundation. The work used the facilities of the Light Microscopy Unit (LMU, Institute of Biotechnology, University of Helsinki) and services for *Drosophila* maintenance and culture (Tampere Drosophila Facility and the Helsinki Drosophila core facility, Hi-Fly) all of which are supported by funding from Biocenter Finland.

AUTHOR CONTRIBUTIONS

Conceptualization, C.Y. and H.T.J.; Methodology, C.Y., E.D., and H.T.J.; Investigation, C.Y., B.R., A.A., M.N., B.O., and E.D.; Writing – Original Draft, H.T.J. and C.Y.; Writing – Review & Editing, all authors; Visualization, H.T.J. and C.Y.; Funding Acquisition, H.T.J. and V.H.; Supervision, H.T.J., C.Y., E.D., and V.H.

DECLARATION OF INTERESTS

The authors declare no competing interests.

Received: May 8, 2020
Revised: June 15, 2020
Accepted: July 8, 2020
Published: August 21, 2020

REFERENCES

Andjelković, A., Oliveira, M.T., Cannino, G., Yalgin, C., Dhandapani, P.K., Dufour, E., Rustin, P., Szibor, M., and Jacobs, H.T. (2015). Diiron centre mutations in *Ciona intestinalis* alternative oxidase abolish enzymatic activity and prevent rescue of cytochrome oxidase deficiency in flies. Sci. Rep. *5*, 18295.

Bahhir, D., Yalgin, C., Ots, L., Järvinen, S., George, J., Naudí, A., Krama, T., Krams, I., Tamm, M., Andjelković, A., et al. (2019). Manipulating mtDNA *in vivo* reprograms metabolism via novel response mechanisms. PLoS Genet. *15*, e1008410.

Bardet, P.-L., Kolahgar, G., Mynett, A., Miguel-Aliaga, I., Briscoe, J., Meier, P., and Vincent, J.-P. (2008). A fluorescent reporter of caspase activity for live imaging. Proc. Natl. Acad. Sci. U S A *105*, 13901–13905.

Bender, A., Krishnan, K.J., Morris, C.M., Taylor, G.A., Reeve, A.K., Perry, R.H., Jaros, E., Hersheson, J.S., Betts, J., Klopstock, T., et al. (2006). High levels of mitochondrial DNA deletions in *substantia nigra* neurons in aging and Parkinson disease. Nat. Genet. *38*, 515–517.

Bose, A., and Beal, M.F. (2016). Mitochondrial dysfunction in Parkinson's disease. J. Neurochem. *139* (*Suppl. 1*), 216–231.

Deng, H., Wang, P., and Jankovic, J. (2018). The genetics of Parkinson disease. Ageing Res. Rev. *42*, 72–85.

Dubowy, C., and Sehgal, A. (2017). Circadian Rhythms and sleep in *Drosophila melanogaster*. Genetics *205*, 1373–1397.

Estacio-Gómez, A., and Díaz-Benjumea, F.J. (2014). Roles of Hox genes in the patterning of the central nervous system of *Drosophila*. Fly *8*, 26–32.

Fernius, J., Starkenberg, A., and Thor, S. (2017). Bar-coding neurodegeneration: identifying subcellular effects of human neurodegenerative disease proteins using *Drosophila* leg neurons. Dis. Model. Mech. *10*, 1027–1038.

Frickenhaus, M., Wagner, M., Mallik, M., Catinozzi, M., and Storkebaum, E. (2015). Highly efficient cell-type-specific gene inactivation reveals a key function for the *Drosophila* FUS homolog cabeza in neurons. Sci. Rep. *5*, 9107.

Ge, P., Dawson, V.L., and Dawson, T.M. (2020). PINK1 and Parkin mitochondrial quality control: a

source of regional vulnerability in Parkinson's disease. Mol. Neurodegener. *15*, 20.

Gorman, G.S., Chinnery, P.F., DiMauro, S., Hirano, M., Koga, Y., McFarland, R., Suomalainen, A., Thorburn, D.R., Zeviani, M., and Turnbull, D.M. (2016). Mitochondrial diseases. Nat. Rev. Dis. Primers *2*, 16080.

Guo, M. (2012). *Drosophila* as a model to study mitochondrial dysfunction in Parkinson's disease. Cold Spring Harb. Perspect. Med. *2*, a009944.

Hartenstein, V., Cruz, L., Lovick, J.K., and Guo, M. (2017). Developmental analysis of the dopamine-containing neurons of the *Drosophila* brain. J. Comp. Neurol. *525*, 363–379.

Humphrey, D.M., Parsons, R.B., Ludlow, Z.N., Riemensperger, T., Esposito, G., Verstreken, P., Jacobs, H.T., Birman, S., and Hirth, F. (2012). Alternative oxidase rescues mitochondria-mediated dopaminergic cell loss in *Drosophila*. Hum. Mol. Genet. *21*, 2698–2712.

Ikeda, K., Shiba, S., Horie-Inoue, K., Shimokata, K., and Inoue, S. (2013). A stabilizing factor for mitochondrial respiratory supercomplex assembly regulates energy metabolism in muscle. Nat. Commun. *4*, 2147.

Jeibmann, A., and Paulus, W. (2009). *Drosophila melanogaster* as a model organism of brain diseases. Int. J. Mol. Sci. *10*, 407–440.

Jenett, A., Rubin, G.M., Ngo, T.T., Shepherd, D., Murphy, C., Dionne, H., Pfeiffer, B.D., Cavallaro, A., Hall, D., Jeter, J., et al. (2012). A GAL4-driver line resource for *Drosophila* neurobiology. Cell Rep. *2*, 991–1001.

Kemppainen, K.K., Rinne, J., Sriram, A., Lakanmaa, M., Zeb, A., Tuomela, T., Popplestone, A., Singh, S., Sanz, A., Rustin, P., and Jacobs, H.T. (2014). Expression of alternative oxidase in *Drosophila* ameliorates diverse phenotypes due to cytochrome oxidase deficiency. Hum. Mol. Genet. *23*, 2078–2093.

Kraytsberg, Y., Kudryavtseva, E., McKee, A.C., Geula, C., Kowall, N.W., and Khrapko, K. (2006). Mitochondrial DNA deletions are abundant and cause functional impairment in aged human substantia nigra neurons. Nat. Genet. *38*, 518–520.

Lapuente-Brun, E., Moreno-Loshuertos, R., Acin-Perez, R., Latorre-Pellicer, A., Colas, C., Balsa, E., Perales-Clemente, E., Quirós, P.M., Calvo, E., Rodríguez-Hernández, M.A., et al. (2013). Supercomplex assembly determines electron flux in the mitochondrial electron transport chain. Science *340*, 1567–1570.

Lee, M.-H., and Salvaterra, P.M. (2002). Abnormal chemosensory jump 6 is a positive transcriptional regulator of the cholinergic gene locus in Drosophila olfactory neurons. J. Neurosci. *22*, 5291–5299.

Lees, A.J., Hardy, J., and Revesz, T. (2009). Parkinson's disease. Lancet *373*, 2055–2066.

Lim, J.W., Lee, J., and Pae, A.N. (2020). Mitochondrial dysfunction and Alzheimer's disease: prospects for therapeutic intervention. BMB Rep. *53*, 47–55.

Liu, C. (2020). Targeting the cholinergic system in Parkinson's disease. Acta Pharmacol. Sin. *41*, 453–463.

Mansilla, N., Racca, S., Gras, D.E., Gonzalez, D.H., and Welchen, E. (2018). The complexity of mitochondrial complex IV: an update of cytochrome c oxidase biogenesis in plants. Int. J. Mol. Sci. *19*, 662.

Mao, Z., and Davis, R.L. (2009). Eight different types of dopaminergic neurons innervate the *Drosophila* mushroom body neuropil: anatomical and physiological heterogeneity. Front. Neural Circuits. *3*, 5.

Marcora, M.S., Fernández-Gamba, A.C., Avendaño, L.A., Rotondaro, C., Podhajcer, O.L., Vidal, R., Morelli, L., Ceriani, M.F., and Castaño, E.M. (2014). Amyloid peptides ABri and ADan show differential neurotoxicity in transgenic *Drosophila* models of familial British and Danish dementia. Mol. Neurodeg. *9*, 5.

McGurk, L., Berson, A., and Bonini, N.M. (2015). *Drosophila* as an *in vivo* model for human neurodegenerative disease. Genetics *201*, 377–402.

Riemensperger, T., Issa, A.R., Pech, U., Coulom, H., Nguyễn, M.V., Cassar, M., Jacquet, M., Fiala, A., and Birman, S. (2013). A single dopamine pathway underlies progressive locomotor deficits in a *Drosophila* model of Parkinson disease. Cell Rep. *5*, 952–960.

Sandu, C., Ryoo, H.D., and Steller, H. (2010). *Drosophila* IAP antagonists form multimeric complexes to promote cell death. J. Cell Biol. *190*, 1039–1052.

Sanyal, S., Narayanan, R., Consoulas, C., and Ramaswami, M. (2003). Evidence for cell autonomous AP1 function in regulation of *Drosophila* motor-neuron plasticity. BMC Neurosci. *4*, 20.

Smith, E.F., Shaw, P.J., and De Vos, K.J. (2019). The role of mitochondria in amyotrophic lateral sclerosis. Neurosci. Lett. *710*, 132933.

Talay, M., Richman, E.B., Snell, N.J., Hartmann, G.G., Fisher, J.D., Sorkaç, A., Santoyo, J.F., Chou-Freed, C., Nair, N., Johnson, M., et al. (2017). Transsynaptic mapping of second-order taste neurons in flies by trans-tango. Neuron *96*, 783–795.

Terron, A., Bal-Price, A., Paini, A., Monnet-Tschudi, F., Bennekou, S.H., EFSA WG EPI1 Members, Leist, M., and Schildknecht, S. (2018). An adverse outcome pathway for parkinsonian motor deficits associated with mitochondrial complex I inhibition. Arch. Toxicol. *92*, 41–82.

Tirian, L., and Dickson, B.J. (2017). The VT GAL4, LexA, and split-GAL4 driver line collections for targeted expression in the *Drosophila* nervous system. BioRxiv. https://doi.org/10.1101/198648.

White, K.E., Humphrey, D.M., and Hirth, F. (2010). The dopaminergic system in the aging brain of *Drosophila*. Front. Neurosci. *4*, 205.

Yeh, E., Gustafson, K., and Boulianne, G.L. (1995). Green fluorescent protein as a vital marker and reporter of gene expression in *Drosophila*. Proc. Natl. Acad. Sci. U S A *92*, 7036–7040.

iScience, Volume *23*

Supplemental Information

Effects on Dopaminergic Neurons Are Secondary in COX-Deficient Locomotor Dysfunction in *Drosophila*

Cagri Yalgin, Bohdana Rovenko, Ana Andjelković, Margot Neefjes, Burak Oymak, Eric Dufour, Ville Hietakangas, and Howard T. Jacobs

SUPPLEMENTAL INFORMATION

Contents

Within this file:

In separate files

TRANSPARENT METHODS

Drosophila strains and culture

Drosophila strains used in the study, and their sources, are summarized in Table S1. Flies were maintained in standard high-sugar medium (Kemppainen et al., 2016) on a 12 h light/dark cycle at 25 °C. Crosses were generally implemented in triplicate, with flies tipped to new vials on three successive days after mating.

Repetitive iterative negative geotaxis (RING) assay

Eggs from parents crossed two days earlier were collected over three consecutive days, and cultured at 25 °C until eclosion. Virgin female progeny were then kept in food vials at 25 °C until day 3, when they were sorted into batches of 10 flies and maintained at 25 °C for a further 2 days. On day 5, flies were tipped from vials to 50 ml Falcon tubes without the use of CO_2 (Bartholomew et al., 2015). Up to six Falcon tubes were placed in rows as described (Nichols et al., 2012). After a 10 min waiting period, flies were tipped down and their subsequent behavior recorded using a DFK 21AF04 camera (The Imaging Source, Bremen, Germany) and Media Recorder 2 software (Noldus, Wageningen, Netherlands). The climbing index (Kemppainen et al., 2014) for each vial was manually calculated from recordings as the mean number of flies which climbed 6 cm in 10 s in three trials. Climbing indices from different genotypes were compared by one-way ANOVA with Tukey *post hoc* HSD test. Box plots were drawn with BoxPlotR (boxplot.tyerslab.com), with Tukey-style whiskers (Krzywinski and Altman, 2014).

Evaluation of apoptotic phenotypes

To determine the phenotype produced by inducing cell-death during development in a specific set of cells defined by a given driver, crosses were set up using males from the driver in question

(either homozygous or combined with a genetically marked balancer chromosome) with balanced females of genotype *UAS-Stinger, UAS-hid* / *CyO*. Hid being a potent inducer of the intrinsic pathway of apoptosis (Sandu et al., 2010), this approach allowed the extent of apoptosis to be profiled in surviving non-balancer progeny by the absence of GFP expression in the target cells, and this correlated with any observed phenotype(s).

Lifespan measurements

Flies were mated for 2 days at room temperature. Eggs were collected into fresh vials and cultured to eclosion at 25 °C. Eclosed females were transferred to fresh vials (5 vials per group, 20 flies per vial) and tipped to new vials every 2-3 days until no live flies remained. At each transfer, the number of dead flies was recorded, from which a median lifespan for each vial was calculated.

Western blotting

Flies were anaesthetized and decapitated on ice and heads were snap-frozen for storage at -80 °C. Protein extracts were prepared from batches of 30 fly heads essentially as described by Fernandez-Ayala et al. (2009), by homogenization using a disposable plastic pestle, in PBS containing 1.5% (w/v) Triton X-100 plus, per 25 ml, one cOmplete™ EDTA-free Protease Inhibitor Cocktail tablet (Roche). After incubation at room temperature for 5 min, samples were centrifuged at 15,000 g_{max} for 10 min at room temperature, and supernatants transferred to fresh tubes on ice. Protein concentrations were determined using the Bradford assay. After the addition of an equal volume of SDS sample buffer (Laemmli 2× concentrate, Sigma-Aldrich), samples were heated for 5 min at 100 °C, briefly centrifuged to remove particulates, and 20 μg of each extract was loaded onto 18-well precast Any kD™ Criterion™ TGX Stain-Free™ Protein Gels (Bio-Rad), which were run and blotted as described (Andjelković et al., 2015). For detection of

ATP5A, α-actinin or GAPDH, blots were blocked in PBS-0.1% Tween (PBS-T) containing 5% nonfat milk for 2 h then reacted overnight in the same buffer at 4 °C with primary antibody (ATP5A: Abcam mouse monoclonal ab14748, 1:100,000; α-actinin: rabbit polyclonal C-20 sc-7454-R, Santa Cruz Biotechnology, 1:7,000); GAPDH: goat anti-GAPDH (C Terminus), EB06377, Everest Biotech, 1:5,000) in PBS-T containing 5% nonfat milk at 4 °C, and washed five times for 7 min in PBS-T. After incubation with secondary antibody (respectively, peroxidase-labeled horse anti-mouse IgG (H+L), Vector Laboratories PI-2000, 1:10,000; rabbit anti-goat IgG (H+L) HRP, Invitrogen, ThermoFisher Scientific 31402, 1:5,000 and peroxidase-labeled goat anti-rabbit IgG (H+L), Vector Laboratories PI-1000, 1:10,000) for 1 h at room temperature with further washes, blot signals were visualized by chemiluminescence (Immun Star® Luminol enhancer and substrate, Bio-Rad) and documented both by X-ray film as well as using a Bio-Rad ChemiDoc imager. For detection of Cox4 a similar procedure was used, except that the blocking agent was 5% BSA instead of nonfat milk, primary antibody was Abcam COXIV rabbit polyclonal, ab16056 (1:500) and secondary antibody was peroxidase-labeled goat anti-rabbit IgG (1:10,000; PI-1000; Vector Laboratories).

Tyrosine hydroxylase (TH) assay

The activity of tyrosine hydroxylase was measured spectrophotometrically by the formation of dopachrome, essentially as described earlier (Vermeer et al., 2013; Figueira et al., 2017). On the day of eclosion, flies were snap-frozen in liquid nitrogen, vortexed for 20 s at 4 °C to separate fly heads from bodies, then passed through a household sieve to collect the heads, which were stored at -80 °C unless processed immediately. Heads were homogenized (1 mg per 10 µl, using a plastic micropestle in a 1.5 ml Eppendorf tube) in ice-cold 50 mM Tris/HCl (pH 7.4) containing 0.1 mM phenylmethylsulfonyl fluoride (PMSF) and 0.1 mM dithiothreitol (DTT). TH activity was assayed in a reaction mixture containing 100 mM HEPES/KOH (pH 7.0), 0.25 mM

tetrahydrobiopterin, 500 μM ferrous sulphate, 200 μM tyrosine, 100 μM sodium periodate, and 20-40 μg of supernatant protein, with a blank without protein extract used for background subtraction. The reaction was monitored on a 2200 EnSpire plate reader (Perkin Elmer, US) at 475 nm for 30 min at 21 °C. Production of L-DOPA (L-3,4-dihydroxyphenylalanine) was determined using a molar extinction coefficient for dopachrome of $\varepsilon = 3700\ M^{-1}\ cm^{-1}$. One unit of tyrosine hydroxylase was defined as the amount of enzyme generating 1 μmol of L-DOPA per min. In figures TH activity is expressed in international milliunits (mU) per milligram of soluble protein (mU/mg protein). Protein content was measured by the Bradford (1976) method, with bovine serum albumin (1-8 μg) used as a standard.

Respirometry

Respirometry was conducted essentially as previously (Andjelković et al., 2015), except using batches of 50 freshly isolated heads from adult males instead of whole flies as source material, and employing the O2K oxygraph instrument (Oroboros).

TUNEL assay

Cell death was profiled essentially as described by Ghosh et al. (2011) and Trunova and Giniger (2012). Brains were dissected out in HL3.1 buffer (70 mM NaCl, 5 mM KCl, 20 mM $MgCl_2$, 10 mM $NaHCO_3$, 5 mM HEPES/NaOH, 115 mM sucrose, 5 mM trehalose, pH 7.2) and immediately fixed in freshly made (Yalgin et al., 2011) ice-cold 4% paraformaldehyde in 0.1% PBS (pH 7.2) for 20 min. After 3 washes for 20 min in 0.1% Triton X-100 in PBS (PBS-Tx), brains were permeabilized in 100 mM citrate in PBS-Tx at 65 °C for 30 min, then subjected to TUNEL reaction (In Situ Cell Death Detection Kit, fluorescein, Roche, Cat. No. 11684795910) for 3 h at 37 °C in the dark, followed by three washes for 20 min in PBS-Tx in the dark at room temperature. Brains were then immunostained for fluorescein according to the protocol below

(see also Table S2). Positive control brains were made by subjecting fixed wild-type brains to DNase I according to manufacturer's instructions (ThermoFisher Scientific, Cat. no. #EN0521) after the permeabilization step.

Immunohistochemistry

Brains were dissected out and fixed as for the TUNEL assay and blocked in freshly prepared 5% bovine serum albumin (BSA; Sigma #A7906) for 20 min at room temperature. They were then incubated in primary antibody solution (see Table S2), diluted in 5% BSA in PBS-Tx for ~36 hours at 4 °C, washed 3 times for 20 min in PBS-Tx, and incubated in secondary antibody solution, diluted in 5% BSA in PBS-Tx for 2 nights at 4 °C (Wu and Luo, 2006). After 3 final washes for 20 min in PBS-Tx, brains were mounted in 80% glycerol with coverslips raised by double-sided tape. Dissection of larvae for immunohistochemistry was as previously reported (Yalgin et al., 2011).

Image acquisition and analyses

Images from whole-mount brains were acquired confocally with a Zeiss LSM 700, and examined manually using Fiji ImageJ software (RRID: SCR_003070). Quantitation of TH signal in immunostained brains used images acquired with a Zeiss LSM 700 using a 10x objective. Brains with the same genotype were imaged under the same coverslip. Up to four brains were scanned at one time and then separated into separate TIFF files using ImageJ. Brightness was adjusted using the same settings for all samples in a given experiment. To assess signals quantitatively, the mean signal intensity of each cell body was measured from the image stack using the 'measure' function of ImageJ. The background signal intensity was separately measured, then subtracted from each ROI measurement. Measurements were statistically compared using

Microsoft Excel. Samples that had been mounted with the posterior surface facing the coverslip were not used in the analyses.

SUPPLEMENTAL REFERENCES

[In addition to references already cited in the main paper]

Bartholomew, N.R., Burdett, J.M., VandenBrooks, J.M., Quinlan, M.C., and Call, G.B. (2015). Impaired climbing and flight behaviour in *Drosophila melanogaster* following carbon dioxide anaesthesia. Sci. Rep. *5*, 15298.

Chou, Y., Spletter, M., Yaksi, E., Leong, J.C., Wilson, R.I., and Luo, L. (2010). Diversity and wiring variability of olfactory local interneurons in the *Drosophila* antennal lobe. Nat. Neurosci. *13*, 439–449.

Dietzl, G., Chen, D., Schnorrer, F., Su, K.C., Barinova, Y., Fellner, M., Gasser, B., Kinsey, K., Oppel. S., Scheiblauer, S., et al. (2007). A genome-wide transgenic RNAi library for conditional gene inactivation in *Drosophila*. Nature *448*, 151–156.

Fernandez-Ayala, D.J.M., Sanz, A., Vartiainen, S., Kemppainen, K., Babusiak, M., Mustalahti, E., Costa, R., Tuomela, T., Zeviani, M., Chung, J., et al. (2009). Expression of the *Ciona intestinalis* alternative oxidase (AOX) in *Drosophila* complements defects in mitochondrial oxidative phosphorylation. Cell Metab. *9*, 449–460.

Figueira, F.H., de Quadros Oliveira, N., de Aguiar, L.M., Escarrone, A.L., Primel, E.G., Barros, D.M., and da Rosa, C.E. (2017). Exposure to atrazine alters behaviour and disrupts the dopaminergic system in *Drosophila melanogaster*. Comp. Biochem. Physiol. C Toxicol. Pharmacol. *202*, 94–102.

Friggi-Grelin, F., Coulom, H., Meller, M., Gomez, D., Hirsh, J., and Birman, S. (2003). Targeted gene expression in *Drosophila* dopaminergic cells using regulatory sequences from tyrosine hydroxylase. J. Neurobiol. *54*, 618–627.

Ghosh, A., Manrique-Hoyos, N., Voigt, A., Schulz, J. B., Kreutzfeldt, M., Merkler, D., and Simons, M. (2011). Targeted ablation of oligodendrocytes triggers axonal damage. PloS One *6*, e22735.

Hummel, T., Krukkert, K., Roos, J., Davis, G., and Klämbt, C. (2000). Drosophila Futsch/22C10 is a MAP1B-like protein required for dendritic and axonal development. Neuron *26*, 357–370.

Kemppainen, E., George, J., Garipler. G., Tuomela, T., Kiviranta, E., Soga, T., Dunn, C.D., and Jacobs, H.T. (2016). Mitochondrial dysfunction plus high-sugar diet provokes a metabolic crisis that inhibits growth. PLoS One *11*, e0145836

Krzywinski, M., and Altman, N. (2014). Visualizing samples with box plots. Nat. Methods *11*, 119–120.

Kvon, E.Z., Kazmar, T., Stampfel, G., Yáñez-Cuna. J.O., Pagani, M,, Schernhuber, K., Dickson, B.J., Stark, A. (2014). Genome-scale functional characterization of *Drosophila* developmental enhancers in *vivo*. Nature *512*, 91–95.

Li, H., Chaney, S., Roberts, I.J., Forte, M., and Hirsh, J. (2000). Ectopic G-protein expression in dopamine and serotonin neurons blocks cocaine sensitization in *Drosophila melanogaster*. Curr. Biol. *10*, 211–214.

Mahr, A., and Aberle, H. (2006). The expression pattern of the *Drosophila* vesicular glutamate transporter: a marker protein for motoneurons and glutamatergic centers in the brain. 6, 299–309.

Nichols, C.D., Becnel, J., and Pandey, U.B. (2012). Methods to assay *Drosophila* behavior. J. Vis. Exp. (*61*), 3795.

Pfeiffer, B.D., Ngo, T.-T.B., Hibbard, K.L., Murphy, C., Jenett, A., Truman, J.W., and Rubin; G.M. (2010). Refinement of tools for targeted gene expression in *Drosophila*. Genetics *186*, 735–755.

Trunova, S., and Giniger, E. (2012). Absence of the Cdk5 activator p35 causes adult-onset neurodegeneration in the central brain of *Drosophila*. Dis. Model Mech. *5*, 210–219.

Vermeer, L.M., Higgins, C.A., Roman, D.L., Doorn, J.A. (2013). Real-time monitoring of tyrosine hydroxylase activity using a plate reader assay. Anal. Biochem. 432,11–15.

Wu, J. S., and Luo, L. (2006). A protocol for dissecting *Drosophila melanogaster* brains for live imaging or immunostaining. Nat. Protoc. *1*, 2110–2115.

Yalgin, C., Karim, M.R., Moore, A.W. (2011). Immunohistological labeling of microtubules in sensory neuron dendrites, tracheae, and muscles in the *Drosophila* larva body wall. J. Vis. Exp. (*57*), 3662.

SUPPLEMENTAL TABLES

Table S2. Antibodies used in immunohistochemistry, Related to Figures 1 and 4-9

Antibody	**Supplier**	**Dilution**	**RRID, Reference or Comment**
Rat anti-Elav, clone 7E8A10	Developmental Studies Hybridoma Bank	1:200	RRID:AB_528218
Mouse anti-Repo clone 8D12	Developmental Studies Hybridoma Bank	1:200	RRID:AB_528448
Rabbit anti-TH	Merck Millipore #AB152	1:200 or 500 (see figure legends)	RRID:AB_390204
Rabbit anti-GABA	Sigma #A2052	1:200 (1:500 in some experiments)	RRID:AB_477652
Mouse anti-ChAT, clone ChAT4B1	Developmental Studies Hybridoma Bank	1:100	RRID:AB_528122, Chou et al., 2010
Rabbit anti-fluorescein	Molecular Probes A-889	1:500	RRID:AB_221561
Rabbit anti-GFP	Abcam #ab6556	1:1000	RRID:AB_305564
Mouse anti-GFP, clone 1G9	Developmental Studies Hybridoma Bank	1:1000 (differs in some experiments: see figure legends)	RRID:AB_2617420
Rat anti-RFP, clone 5F8	Chromotek #5F8-100	1:200	RRID:AB_2336064
Mouse anti-actin, JLA-20-S	Developmental Studies Hybridoma Bank	1:200	RRID:AB_528068, for Westerns
Rat anti-CD8, clone 5H10	ThermoFisher Scientific MCD0800	1:200	RRID:AB_10392843

Rabbit anti-VGlut, affinity purified	kind gift of Dr H. Aberle	1:500	RRID:AB_2315544, Mahr and Aberle, 2006
Mouse anti-Futsch, clone 22C10	Developmental Studies Hybridoma Bank	1:1000	RRID:AB_528403, Hummel et al., 2000
Alexa 647 goat anti-rabbit	ThermoFisher Scientific A21245	1:500	RRID:AB_2535813
Alexa 488 goat anti-rabbit	ThermoFisher Scientific A11008	1:500	RRID:AB_143165
Alexa 647 goat anti-mouse	ThermoFisher Scientific A21240	1:500	RRID:AB_2535809
Alexa 488 goat anti-mouse	ThermoFisher Scientific A11001	1:500	RRID:AB_2534069
Alexa 594 goat anti-rabbit	ThermoFisher Scientific A11012	1:500	RRID:AB_2534079
Alexa 594 goat anti-mouse	ThermoFisher Scientific A11005	1:500	RRID:AB_2534073
Alexa 647 goat anti-rat	ThermoFisher Scientific A21247	1:500	RRID:AB_141778
Alexa 568 goat anti-rat	ThermoFisher Scientific A11077	1:500	RRID:AB_2534121
Alexa 568 goat ant-mouse	ThermoFisher Scientific A11004	1:500	RRID:AB_2534072
Alexa 568 goat anti-rabbit	ThermoFisher Scientific A11011	1:500	RRID:AB_143157
Alexa 488 goat anti-rat	ThermoFisher Scientific A11006	1:500	RRID:AB_2534074

LEGENDS TO SUPPLEMENTAL FIGURES

Figure S1. Supplemental data on effects of pan-neuronal COX7A knockdown (COX assembly, respirometry and apoptosis), Related to Figure 1

(A) Western blots of protein extracts (amounts loaded in the various gel tracks, as indicated, in μg) from pooled heads of 30 male flies of each genotype shown: con (control) – *elav-GAL4*^{C155}, *UAS-Dcr-2* / Y *; P{attP, y*$^{+}$*, w*^{3}*}* / +, and KD (COX7A knockdown) – *elav-GAL4*^{C155}, *UAS-Dcr-2* / Y *; UAS-RNAi*^{COX7A} / +. Horizontally separated tracks are from different gels, probed with antibodies as indicated in Transparent Methods; molecular weights (in kDa) of closest markers run on same gels, following Ponceau S staining of the membranes, as shown. The samples in (i) and (ii) represent two biological replicates. The extent of COX4 depletion was quantitated by densitometry and normalized against α-actinin as a loading reference, giving a residual signal of 34% of the control value for experiment (i) and 48% for experiment (ii). The latter value may be more reliable due to low signal intensities in (i). (B) Respirometry on extracts from pooled heads of 50 male flies of each genotype shown: con (control) and *elav*-GAL4>COX7A KD as above, normalized for protein content, using cI-, cIII- and cIV-linked substrate mixes. No error bars are shown since this was a single large-scale experiment using fresh material. Replicate experiments gave similar data. (C) TUNEL-staining of brain from *elav*-GAL4>COX7A KD male, prepared on the day of eclosion, alongside a *w*^{1118} positive control brain (DNase I-treated). TUNEL stain was amplified by immunohistochemistry (rabbit anti-fluorescein, followed by Alexa 488 goat anti-rabbit, see Table S2). Scale bar 50 μm.

Figure S2. Supplemental data on effects of pan-neuronal COX7A knockdown (apoptotic cells), Related to Figure 1

(A) Number of TUNEL-positive cells per brain (n = 10 for each class, as indicated). Boxplot

shows interquartile range (box), median (bold line), Tukey-style whiskers (Krzywinski and Altman, 2014) and outliers (open circles). *** denotes significant difference (Student's *t* test, $p < 0.001$). Note that this experiment was performed on 21-day old flies not carrying *UAS-Dcr-2*, i.e. the same control and knockdown genotypes as originally studied by Kemppainen et al. (2014) and by Andjelković et al. (2015), showing a milder knockdown phenotype than when *UAS-Dcr-2* is also present. (B) Immunocytochemistry for fluorescein (TUNEL) and nuclear markers for (i) glia (Repo) and (ii) neurons (Elav) in single optical sections from two elav-GAL4>COX7A KD knockdown brains (including *UAS-Dcr-2*). Scale bars 20 μm. Note that both classes of neural cells were affected, even though the driver itself is active only in neurons.

Figures S3 and S4. Supplemental data on effects of pan-neuronal COX7A knockdown (Apoliner), Related to Figure 1

Images of brains of elav-GAL4>COX7A KD males also expressing Apoliner (derived from the cross *UAS-RNAi*^{COX7A} / + ; *UAS-Apoliner* / *TM3, Sb* males to *elav-GAL4*^{C155} ; *UAS-Dcr-2* virgin females), prepared on the day of eclosion. Genotypes were verified by PCR on residual carcasses. GFP was detected by mouse anti-GFP primary antibody (1:2,000) and Alexa 488 goat anti-mouse secondary antibody (1:500), and Elav by rat anti-Elav (1:200) and Alexa 647 goat anti-rat secondary antibody (1:500). For full details of antibodies see Table S2. Images show single optical sections at 2 μm resolution. Fig. S3A (high) and Fig. S4 (low) magnification images, scale bars 20 μm and 100 μm, respectively. At highest magnification in Fig. S3B, one cell in the population appears to show clear co-localization of GFP with the Elav neuronal nuclear marker, although this may be an artifact due to low vertical resolution and high intensity of the cytoplasmic signal. Scale bar 5 μm.

Figure S5. Supplemental data on effects of pan-neuronal COX7A knockdown (ROS), Related to Figure 1

DHE staining of control and elav-GAL4>COX7A KD brains. Signal intensity on an arbitrary scale is as indicated. Scale bars 100 μm.

Figure S6. Counterstaining for Elav validates immunohistochemistry for TH, Related to Figure 1

To check that the depletion of TH observed in COX7A KD brains was not due to differential antibody penetration in different samples, brains of controls (genotype – *elav-GAL4*^{C155} / Y ; *UAS-Dcr-2* / *P{attP,y*$^{+}$*,w*$^{3´}$*}*) and elav-Gal4>COX7A KD flies (genotype – *elav-Gal4*^{C155} / Y; *UAS-Dcr-2* / *UAS-RNAi*^{COX7A}) were counterstained for Elav, a pan-neuronal nuclear marker, as well as TH (1:1,000), as indicated. Zoomed images (scale bars 20 μm; optimized for overall contrast and brightness but otherwise using same settings for controls and knockdown brains) show variable relative signal within a class, but generally lower TH signals in knockdown brains, as quantified in Fig. 1.

Figures S7, S8 and S9. Expression patterns produced by various neuronal GAL4 drivers (*TH*-, *Ddc*-, *TRH*-GAL4), Related to Figure 2

Immunohistochemistry for GFP and the indicated markers (TH – 1:200, Elav, Chat, GABA), of brains of flies expressing nuclear GFP (nGFP, 'Stinger') under the control of the indicated drivers, at different magnifications, as indicated by the scale bars. Fig. S7 – maximum intensity projection of (i, ii) brains of two flies expressing nGFP under the control of *TH*-GALl4. Scale bars 100 μm. Fig. S8 – maximum intensity projection of (i, ii) brains of two flies expressing nGFP under the control of *Ddc*-GAL4. Scale bars 100 μm. Fig. S9A – single optical section from such a specimen, at higher magnification. Scale bar 10 μm. Fig. S9B – maximum intensity

projection of brain of a fly expressing nGFP under the control of *TRH*-GAL4. Scale bar 100 μm.

Figure S10. Phenotypes produced by various neuronal GAL4 drivers, Related to Figure 2

(A) Locomotor impairment produced by COX7A knockdown using various drivers, as indicated, measured 7 or 10 days after eclosion (two separate experiments separated by dashed line). Box-plot nomenclature: boxes denote interquartile range (IQR), bold lines the median, with standard, Tukey-style whiskers (Krzywinski and Altman, 2014). (B) Median lifespan (mean $\pm$ SD, n = 5 except for controls, n = 4) of female flies in which COX7A was knocked down using the indicated drivers. Horizontal lines indicate significant differences (one-way ANOVA with Tukey *post hoc* HSD test, blue lines: $p < 0.01$, red lines: $p < 0.05$). Note that, based on these data, effects of COX7A knockdown in DA neurons were not simply delayed, compared with other neuronal classes. By 10 days of age (A), no effects on locomotor performance were seen and (B) lifespan was only slightly affected, using either of the dopaminergic or the serotonergic drivers.

Figures S11, S12 and S13. Expression pattern produced by the *Cha*-GAL4 driver, Related to Figure 2

Fig. S11A – low magnification images of a series of confocal planes, showing extensive overlap between expressed nGFP, driven by *Cha*-GAL4, and Elav, a pan-neuronal marker. Scale bar 100 μm. Fig. S11B – high magnification image (single optical section) showing the wide quantitative variation in GFP signal between neuronal nuclei, indicative of varying expression using the *Cha*-GAL4 driver. Intensity of staining arbitrarily indicated numerically as 1-5, in increasing intensity. Scale bar 5 μm. Fig. S11C – high magnification image (single optical section) showing that most nGFP-positive cells using the *Cha*-GAL4 driver are also positive for ChAT (choline acteyltransferase), but in many cases at very low levels. Scale bar 5 μm. Fig. S12 – maximum intensity projection of whole brain of a fly expressing nGFP under the control of *Cha*-Gal4.

Scale bar 100 μm. Fig. S13A – high magnification image (single optical section) confirming that some nGFP-positive cells using the *Cha*-GAL4 driver are also positive for TH. Scale bar 10 μm. Fig. S13B – high magnification image (single optical section) showing that some GFP-positive cells are also positive for GABA. Note that, in many cell bodies, the GABA antibody stains mainly the nucleus. Scale bar 20 μm. Thus, in line with Lucin et al. (2019), the *Cha*-GAL4 driver is not 100% specific for cholinergic neurons.

Figure S14. Expression patterns produced by the OK371 driver, Related to Figure 2

Maximum intensity projection of the brain from a fly expressing nGFP under the control of OK371, immunostained for GFP and Elav, as shown. Scale bar 100 μm.

Figures S15, S16 and S17. Expression driven by R55A05 is confined to cholinergic neurons, Related to Figures 3 and 4

Immunohistochemistry of brains from 5-day old male flies expressing various reporters under the control of the R55A05 GAL4 driver. Fig. S15 – maximum intensity projection of the whole brain stained for CD8 (genotype: *R55A05-GAL4* / *UAS-mCD8::GFP*). For a single optical section of an equivalent brain co-stained for CD8 and ChAT, see Fig. 3A. Scale bar 50 μm. Fig. S16A, S16B, S17A and S17B – maximum intensity projections of whole brains stained for (nuclear) GFP and the neural markers indicated: Fig. S16 – GABA, as a marker for GABAergic neurons, Fig. S17A – TH (1:200), as a marker for DA neurons, and Fig. S17B – Repo, as a marker for glial cells. Genotype: *UAS-Stinger* / + ; *R55A05-GAL4* / +. Scale bars: 100 μm, except Fig. S17B – 50 μm.

Figures S18, S19 and S20. R59E04 drives expression in a subset of cholinergic, but not DA neurons, Related to Figures 3 and 4

Fig. S18 – reference images showing expression patterns using R55A05 and R54E09 GAL4 drivers (Jenett et al., 2012), in the brain and ventral nerve cord as indicated – publicly available images generated by the Janelia FlyLight Project Team and the laboratories of Gerald M. Rubin, James W. Truman, Richard S. Mann, and Christopher Q. Doe, reproduced under Creative Commons Licence (CC BY 4.0). See also https://www.janelia.org/open-science/janelia-flylight-expression-patterns-gal4-and-lexa-driver-lines. Scale bars 100 μm, GFP and Bruchpilot (background control) signals as indicated. Fig. S19 – zoomed immunohistochemistry images from bottom panel of Fig. 4C: maximum projection image of three brain regions (i-iii) from a fly expressing (membrane-bound) mCD8-GFP under the control of the R59E04 GAL4 driver, co-stained for GFP and ChAT. Scale bars 20 μm. Fig. S20 – immunohistochemistry of brain from a 5-day old male fly expressing nuclear GFP under the control of the R59E04 GAL4 driver (genotype: *UAS-Stinger* / + ; *R59E04-GAL4* / +). Maximum intensity projection co-stained for GFP and for TH (1:200). Scale bar100 μm. Note that the discontinuity in the image in Fig. S20 is due to separate acquisition of the z-stacks using a relatively aged microscope that does not digitally smooth out such boundaries when stacks are combined.

Figure S21. R51C09 does not drive expression in GABAergic or DA neurons, Related to Figure 5

Immunohistochemistry of brains from 5-day old male flies expressing nuclear GFP under the control of the R51C09 GAL4 driver (genotype: *UAS-Stinger* / + ; *R51C09-GAL4* / +). Maximum intensity projection of the whole brain stained for GFP and for (A) GABA and (B) TH (1:500). Scale bars 100 μm. Note that the reporter used here (Stinger, nuclear GFP) enables colocalization to be visualized more reliably (green nuclei surrounded by magenta cytoplasm, rather than white

areas which could arise from signals in different cells not resolved by the optics). The GFP reporter used in Fig. 5 is the membrane bound (mCD8) version, which prominently labels projections in the optic lobe, whereas the nuclear GFP does not.

Figure S22. R52A01 does not drive expression in GABAergic or DA neurons, Related to Figure 6

Immunohistochemistry of brains from 5-day old male flies expressing nuclear GFP under the control of the R52A01 GAL4 driver (genotype: *UAS-Stinger* / + ; *R52A01-GAL4* / +). Maximum intensity projection of the whole brain stained for GFP and for (A) GABA and (B) TH (1:500). Scale bars 100 μm. Note that the reporter used here (Stinger, nuclear GFP) enables colocalization to be visualized more reliably (green nuclei surrounded by magenta cytoplasm, rather than white areas which could arise from signals in different cells not resolved by the optics). The GFP reporter used in Fig. 6 is the membrane bound (mCD8) version, which prominently labels projections in the optic lobe, whereas the nuclear GFP does not.

Figure S23. Minimal overlap of expression directed by cholinergic drivers R55A05 and R59E04, Related to Figures 4-6

(A) Maximum intensity projection, (B) zoomed substack from (A) and (C, D) single optical sections from brain from a female fly co-expressing GFP (green) under the control of driver R59E04 and RFP (magenta) under the control of R55A05, using the LexA and GAL4 expression systems, respectively. Genotype was *10XUAS-IVS-mCD8::RFP, 13XLexAop2-mCD8::GFP* / + ; *R59E04-lexA* / + ; *R55A05-GAL4* /+. Scale bars (A) 100 μm, (B, C, D) 20 μm. Note the almost total lack of overlap, even for brain regions where neurites targeted by each driver intermingle, as in (B). In a small number of specific brain regions, e.g., in (C), there is overlap of the signals, whereas in most of the brain, e.g., in (D), they are completely separate.

Figure S24. Minimal overlap of expression directed by glutamatergic drivers R52A01 and R51C09, Related to Figures 4-6

(A) Maximum intensity projection, (B) single optical section and (C) zoomed area from (B) of brain from a female fly co-expressing GFP (green) under the control of driver R52A01 and RFP (magenta) under the control of R51C09, using the LexA and GAL4 expression systems, respectively. Genotype was *10XUAS-IVS-mCD8::RFP*, *13XLexAop2-mCD8::GFP* / + ; *R52A01-lexA* / + ; *R51C09-GAL4* /+. Scale bars (A, B) 100 μm, (C) 20 μm. Note specific brain structures in (C), where both reporters are expressed, indicating a small degree of overlap between the drivers. See also images from the FlyLight collection at: http://flweb.janelia.org/cgi-bin/view_flew_imagery.cgi?line=R51C09 and http://flweb.janelia.org/cgi-bin/view_flew_imagery.cgi?line=R52A01.

Figures S25 through S31. Brain regions where DA neurons and R55A05 (or R59E04) neurons project show a small degree of overlap, Related to Figure 7

Fig. S25 and S26 – immunohistochemistry for TH (1:200, green) and CD8 (magenta) of brains from male fly expressing mCD8-Cherry under the control of Fig. S25 – R55A05 and Fig. S26 – R59E04. Genotypes – *R55A05-GAL4* (or *R59E04-GAL4*) / *UAS-mCD8::Cherry*. Maximum projection images of the whole brain (scale bar 100 μm), with zoomed areas as indicated. Fig. S27, S28 and S29 – individual TH and RFP signals from optical sections of the brain analyzed in Fig. 7, showing minimal overlap between (TH-positive) DA neurons and neurons post-synaptically expressing RFP under the control of trans-Tango, driven by R55A05. Scale bars 10 μm. Panel numbers correspond with those of Fig. 7. The clusters of neurons intensely stained for TH (panels *ii*, *iii*, and *v*) are negative for RFP, whilst the cell-bodies of a few neurons staining intensely for RFP are essentially negative for TH (panel *vii*). A few neurites are stained for both

markers, as shown by the small minority of signals that overlap (panels *x* and *xii*). Fig. S30 and S31 – optical sections of the brain analyzed in Fig. 7, showing the location of the DA neuron clusters visualized in panels *i-v* thereof. Scale bars in zoomed images 10 μm.

Figures S32 through S39. TH deficiency in subsets of neurons with COX7A knockdown, Related to Figures 8 and 9

Immunohistochemistry for TH (1:1,000) and Elav in brains from flies with COX7A knockdown or controls with only Dcr-2 overexpression, as indicated, using the GAL4 drivers shown (maximum intensity projections). Individual specimens also shown in Fig. 8 or 9 (TH only) indicated by *. Genotypes – Dcr-2 only: + ; *R55A05-GAL4* (or *R59E04-GAL4*, or *R52A01-GAL4* or *R51C09-GAL4*) / *UAS-Dcr-2*, COX7A-KD: *UAS-RNAi*^{COX7A} / + ; *R55A05-GAL4* (or *R59E04-GAL4*, or *R52A01-GAL4* or *R51C09-GAL4*) / *UAS-Dcr-2*. Scale bars 100 μm. Contrast and brightness have been similarly adjusted in each image, giving uniform background fluorescence. Sample variation and the subtle nature of the observed differences preclude reliable quantitation.

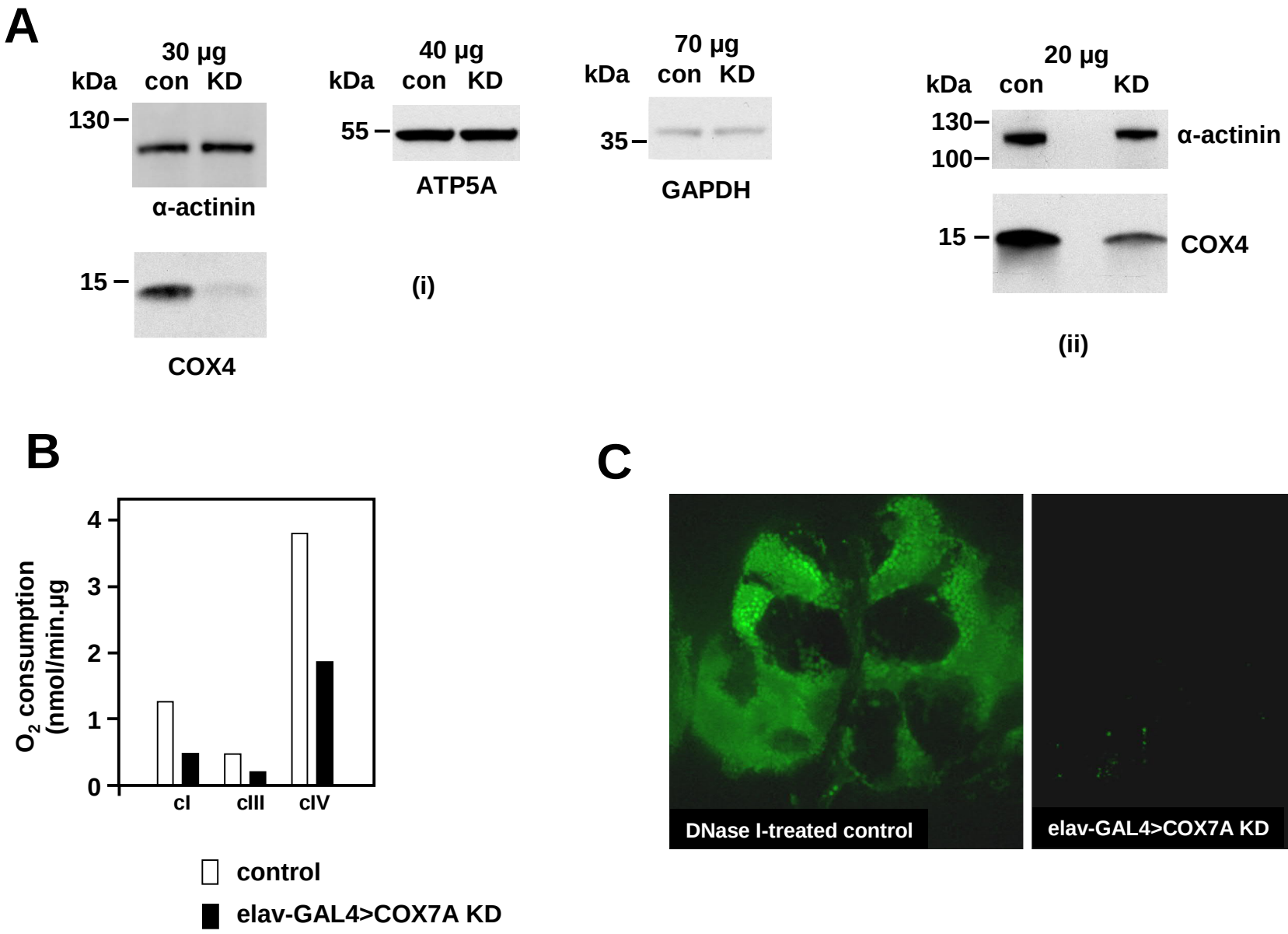

Yalgin et al, Figure S1

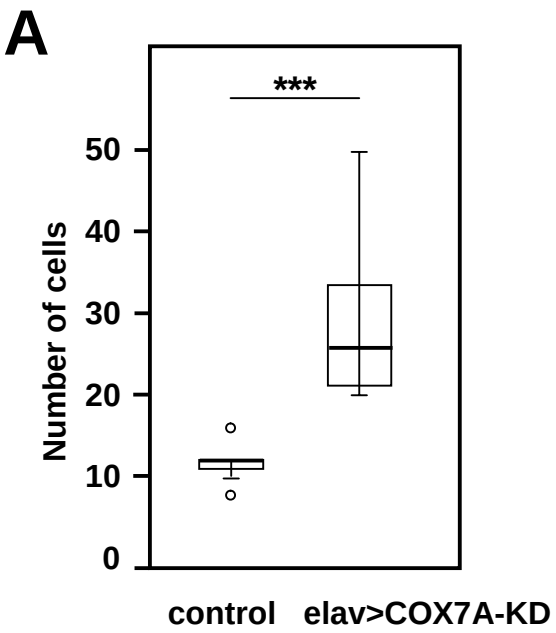

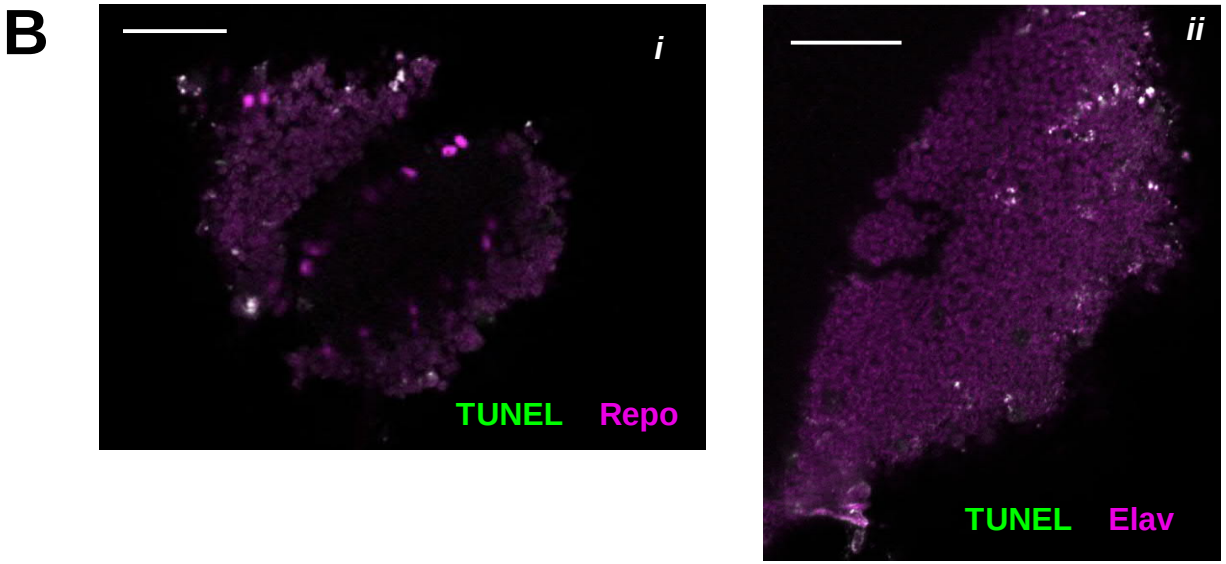

Yalgin et al, Figure S2

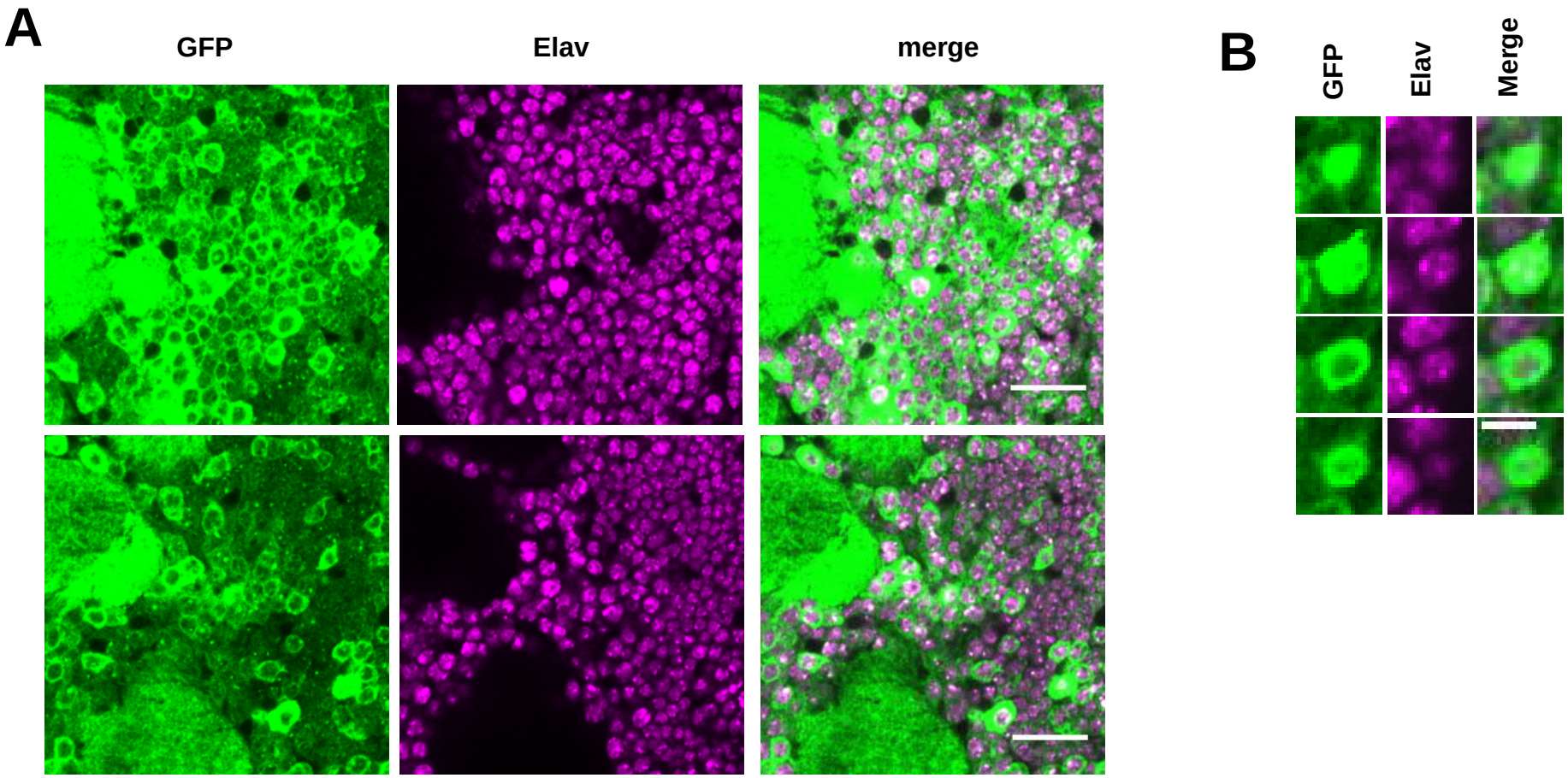

Yalgin et al, Figure S3

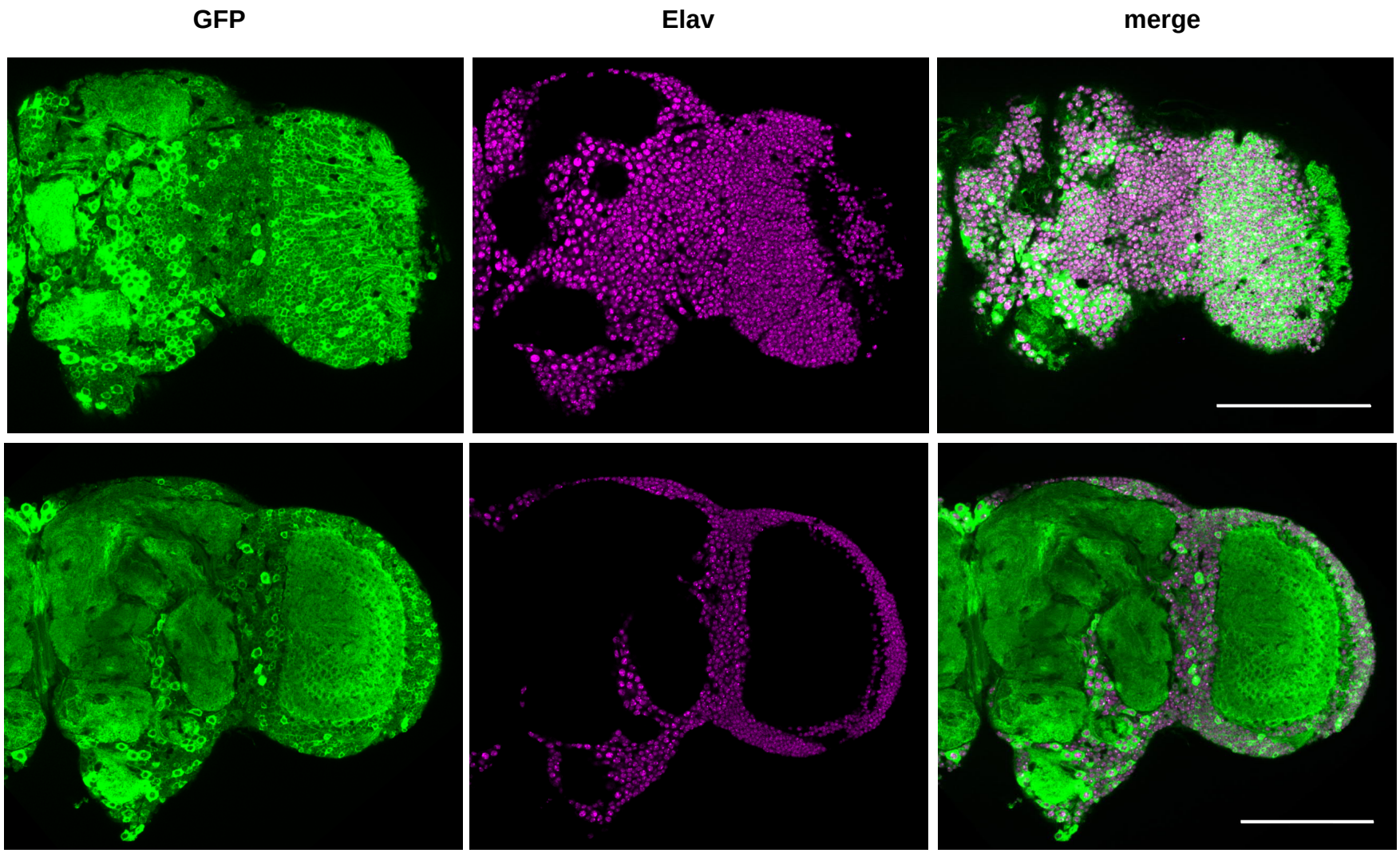

Yalgin et al, Figure S4

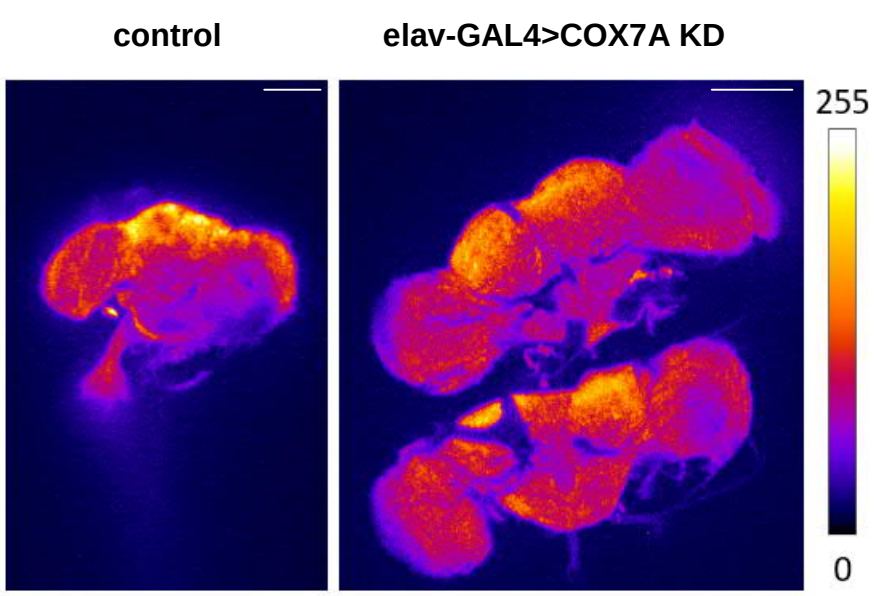

Yalgin et al, Figure S5

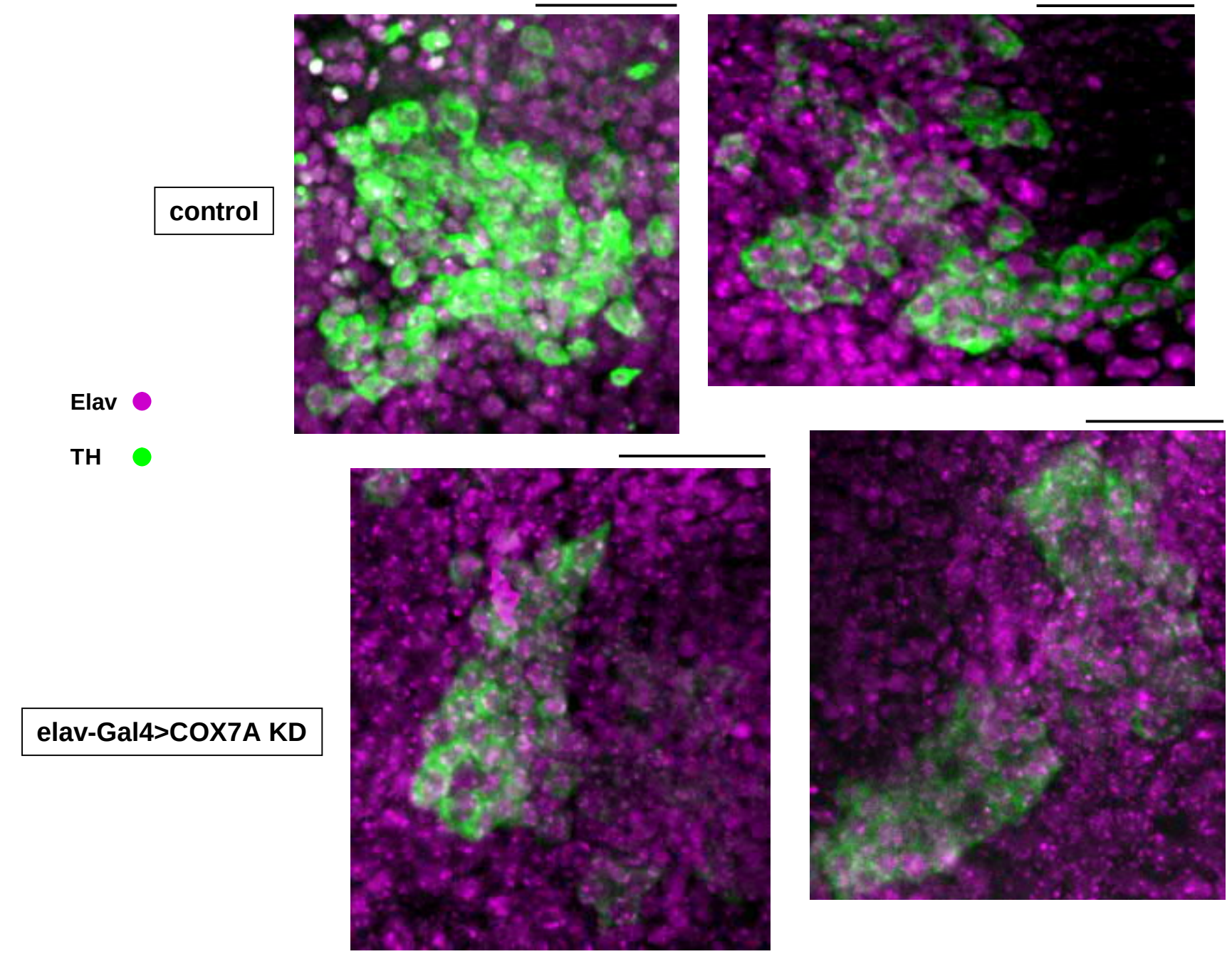

Yalgin et al, Figure S6

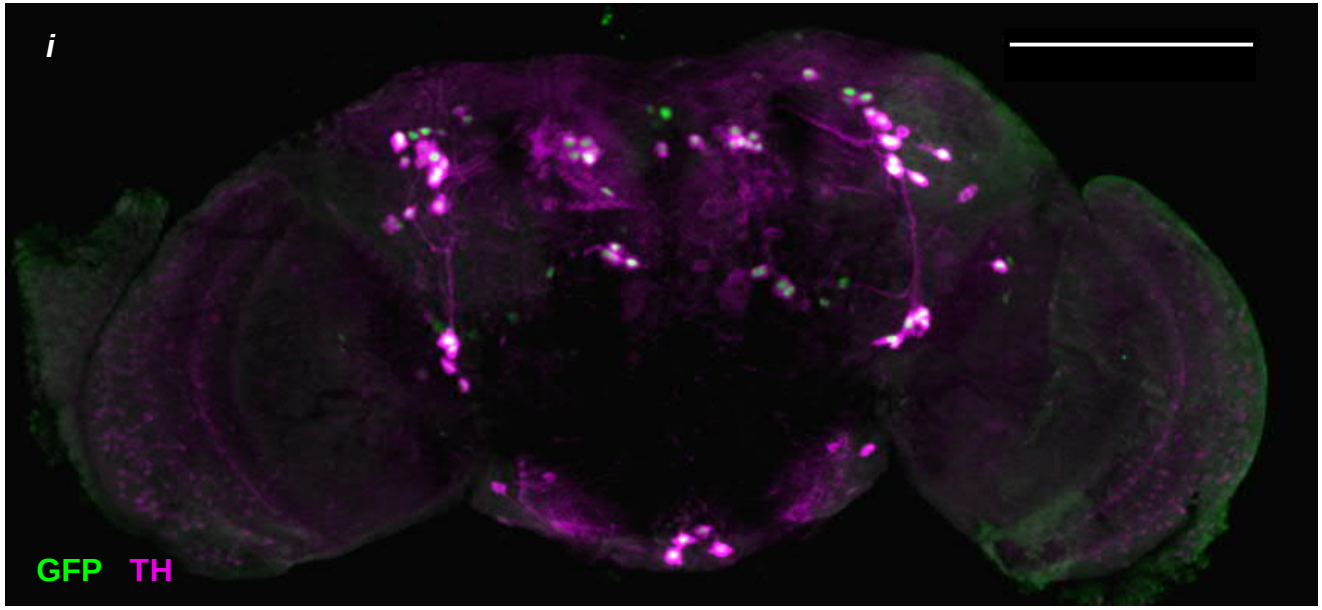

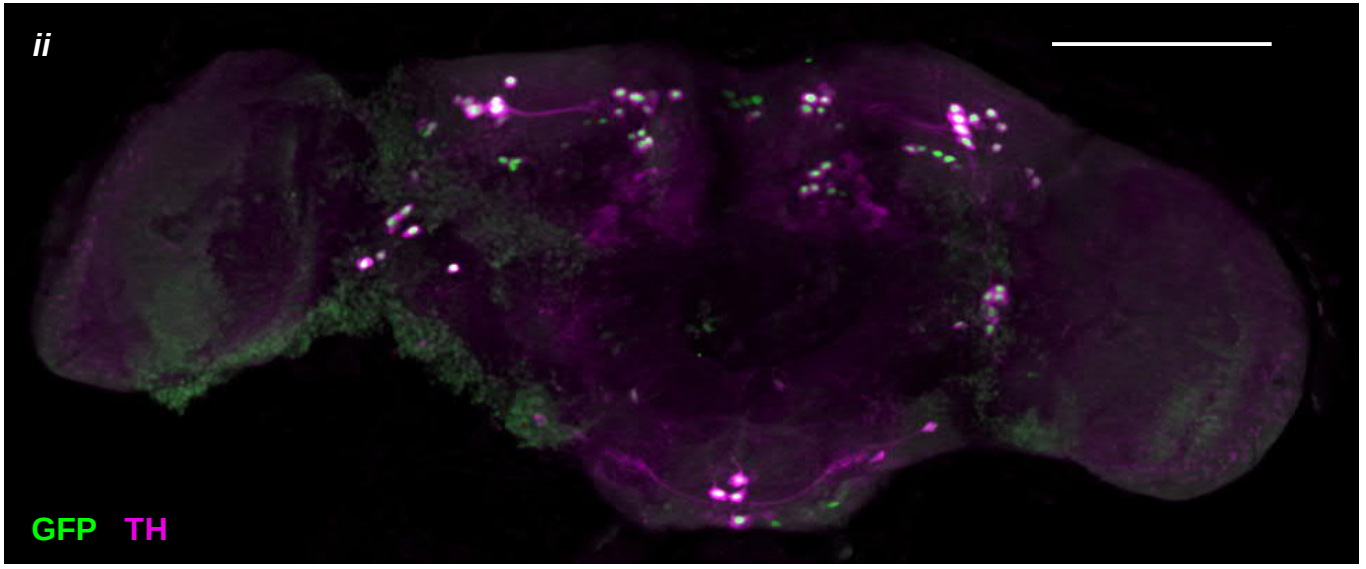

TH-GAL4>nGFP

Yalgin et al, Figure S7

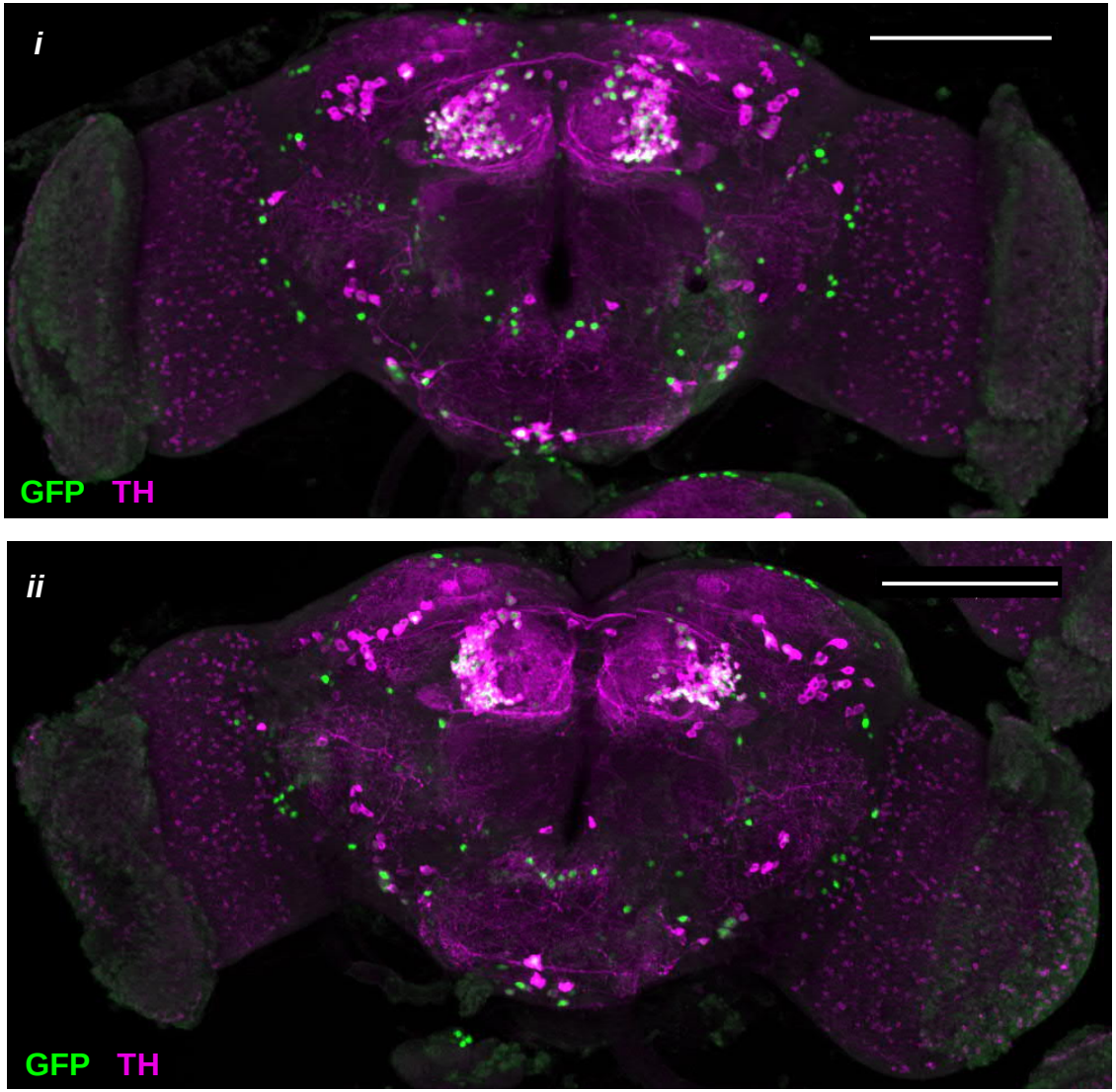

Ddc-GAL4>nGFP

Yalgin et al, Figure S8

A

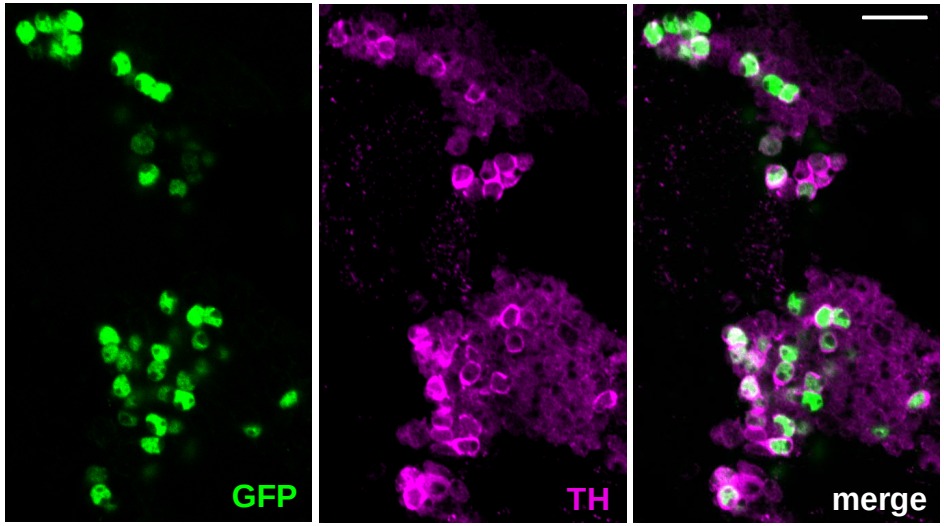

Ddc-GAL4>nGFP

B

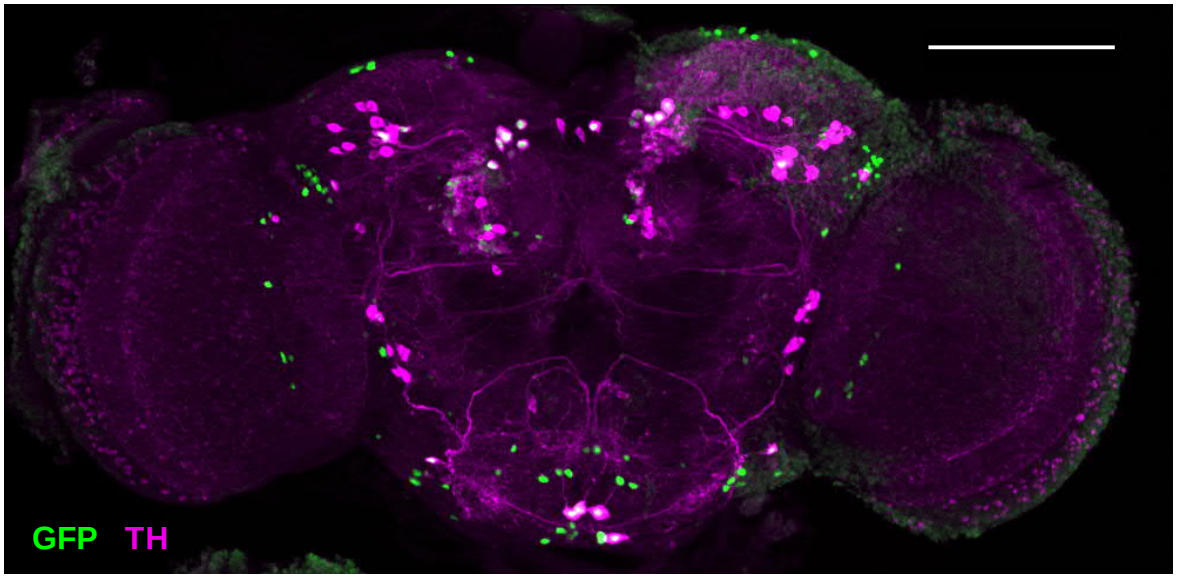

TRH-GAL4>nGFP

Yalgin et al, Figure S9

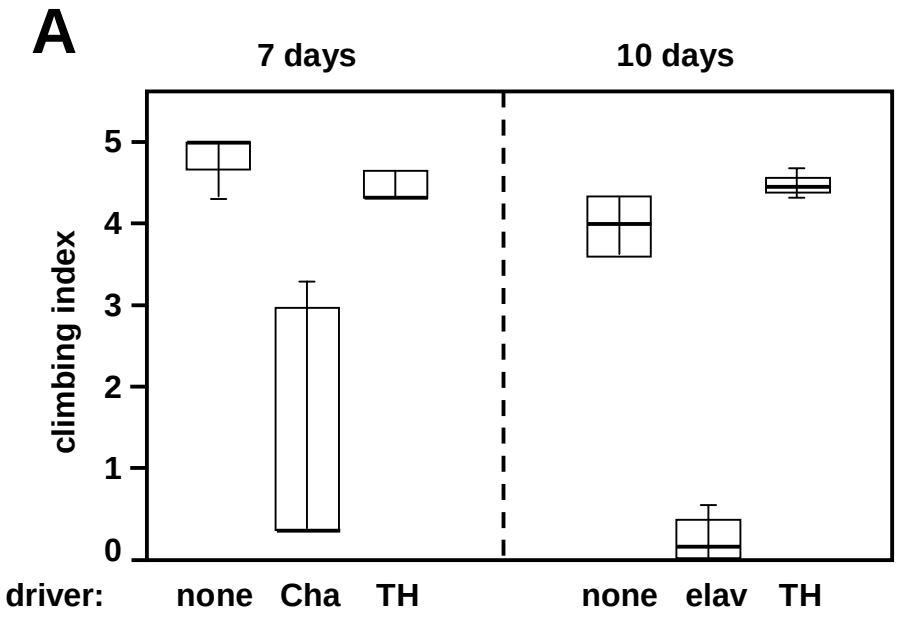

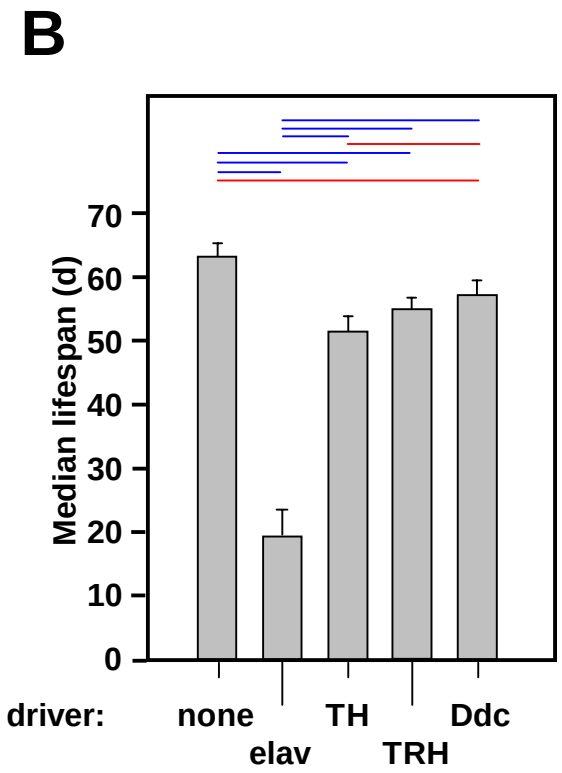

Yalgin et al, Figure S10

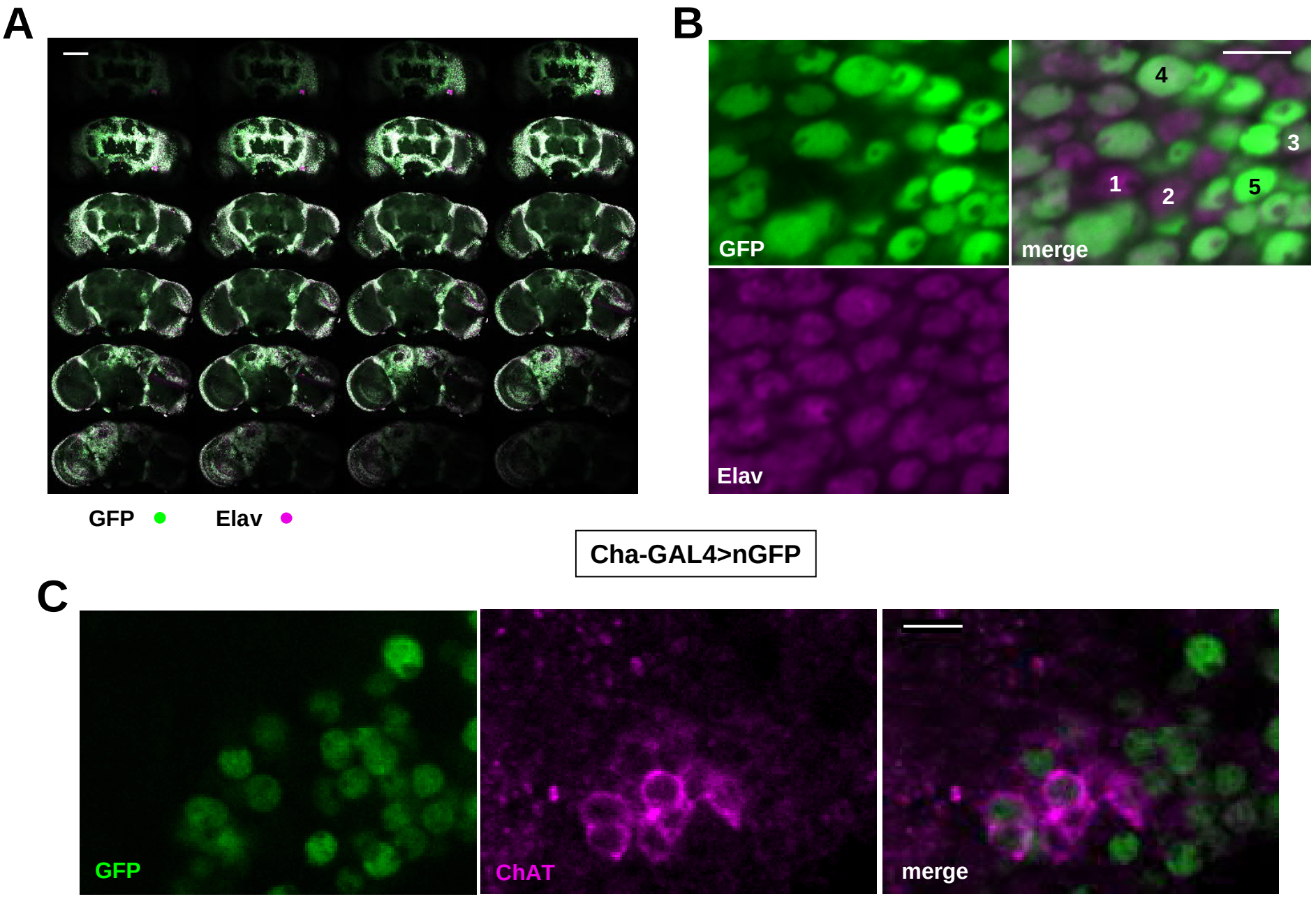

Yalgin et al, Figure S11

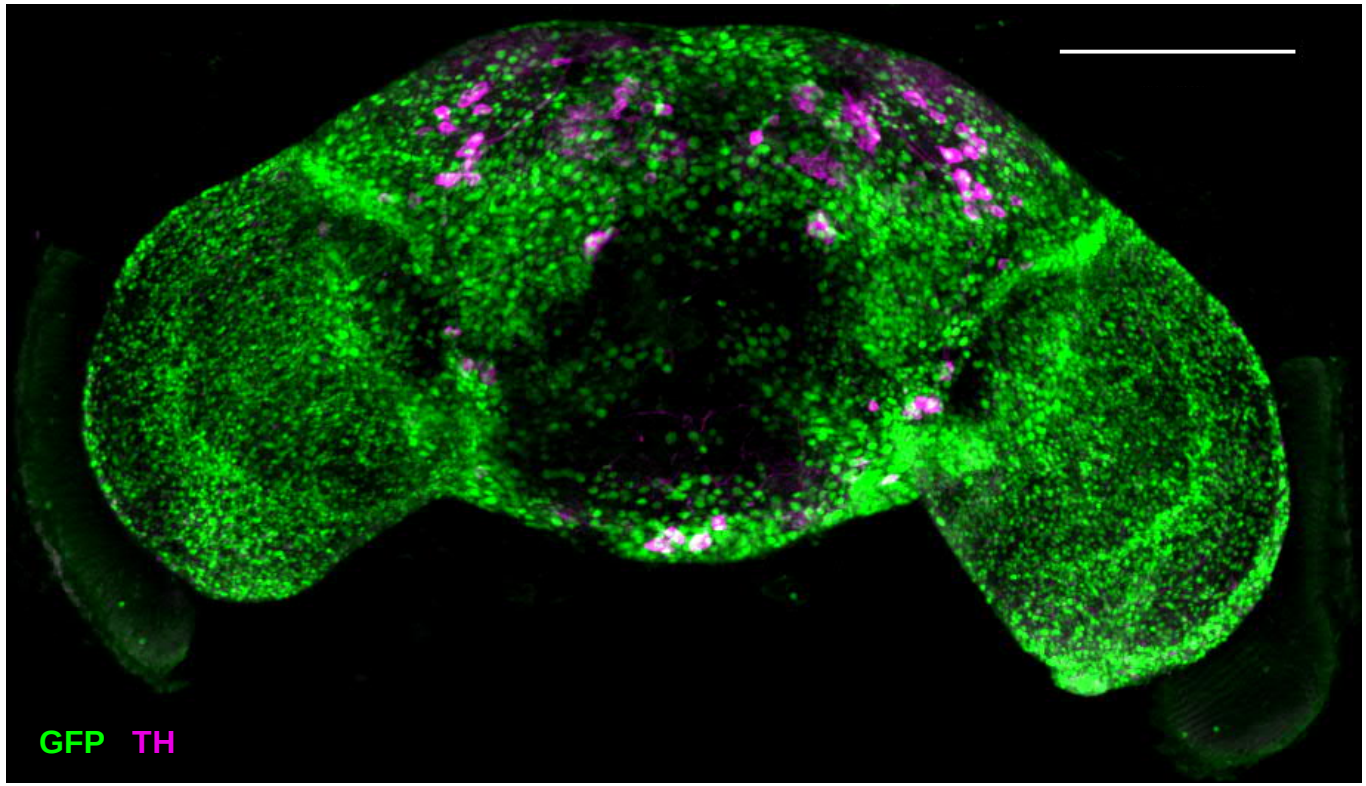

Cha-GAL4>nGFP

Yalgin et al, Figure S12

A

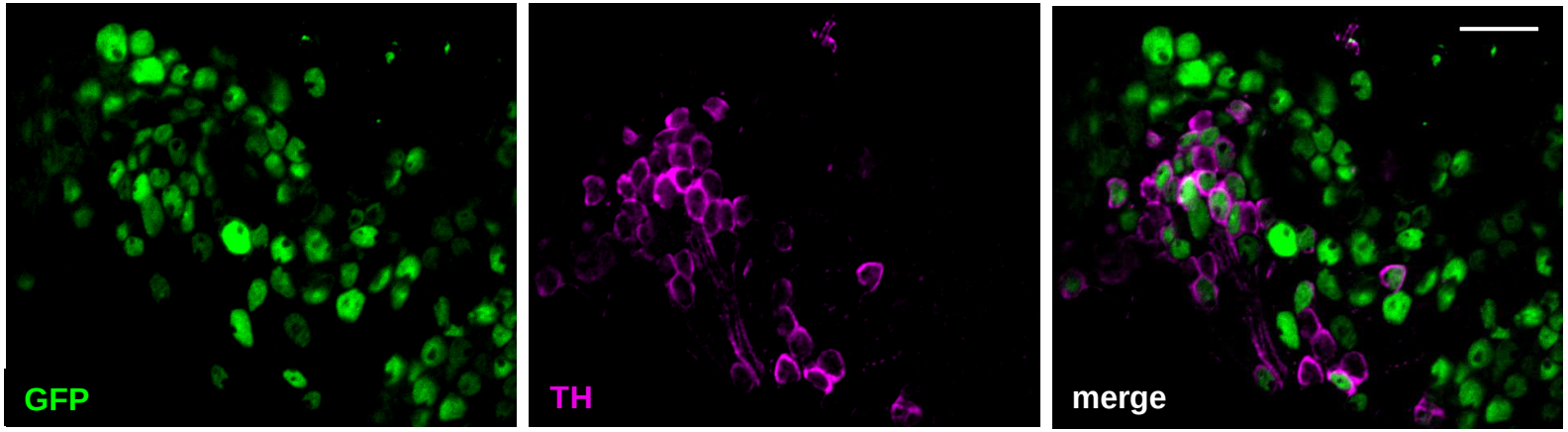

Cha-GAL4>nGFP

B

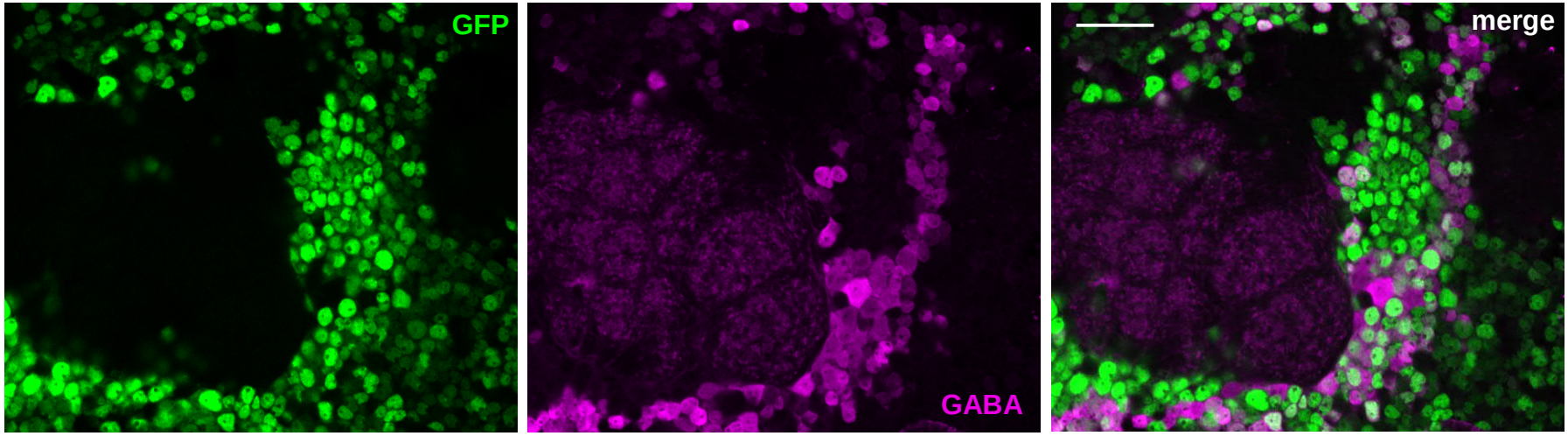

Yalgin et al, Figure S13

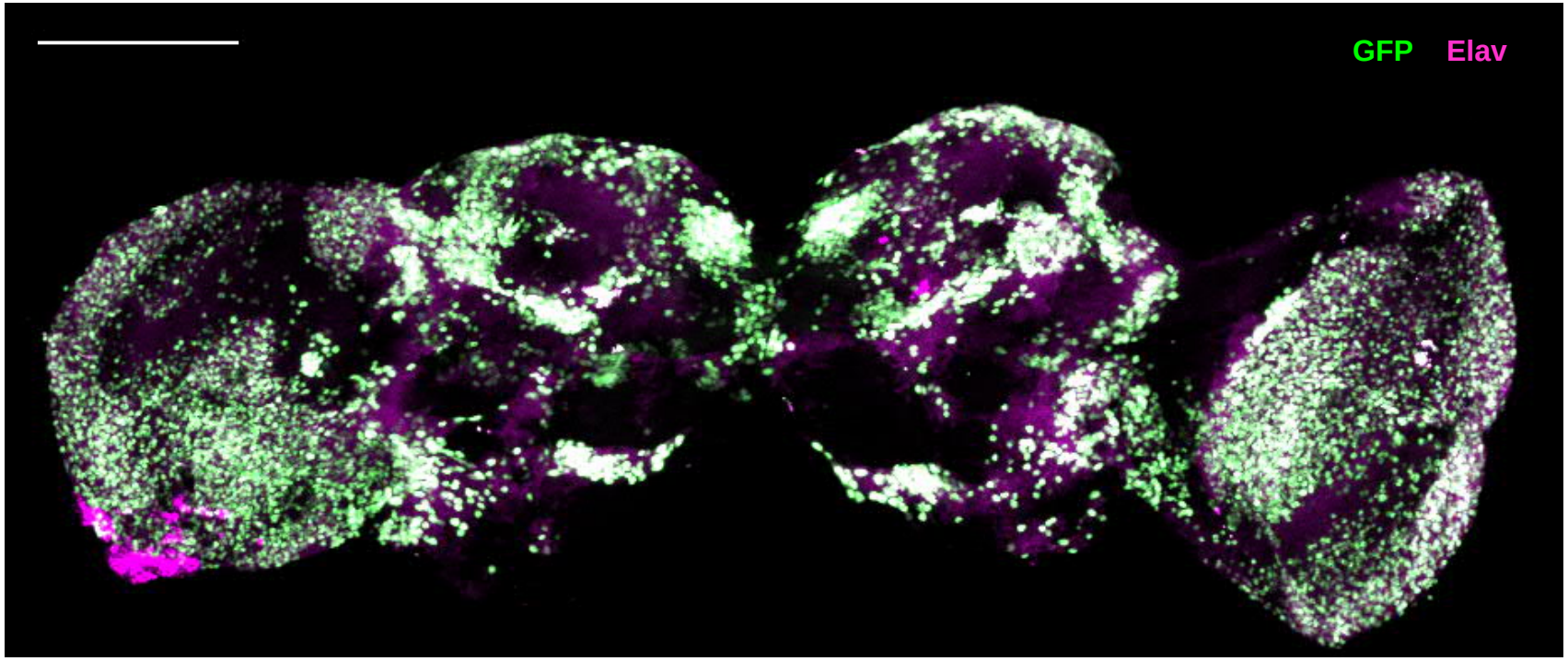

OK371>nGFP

Yalgin et al, Figure S14

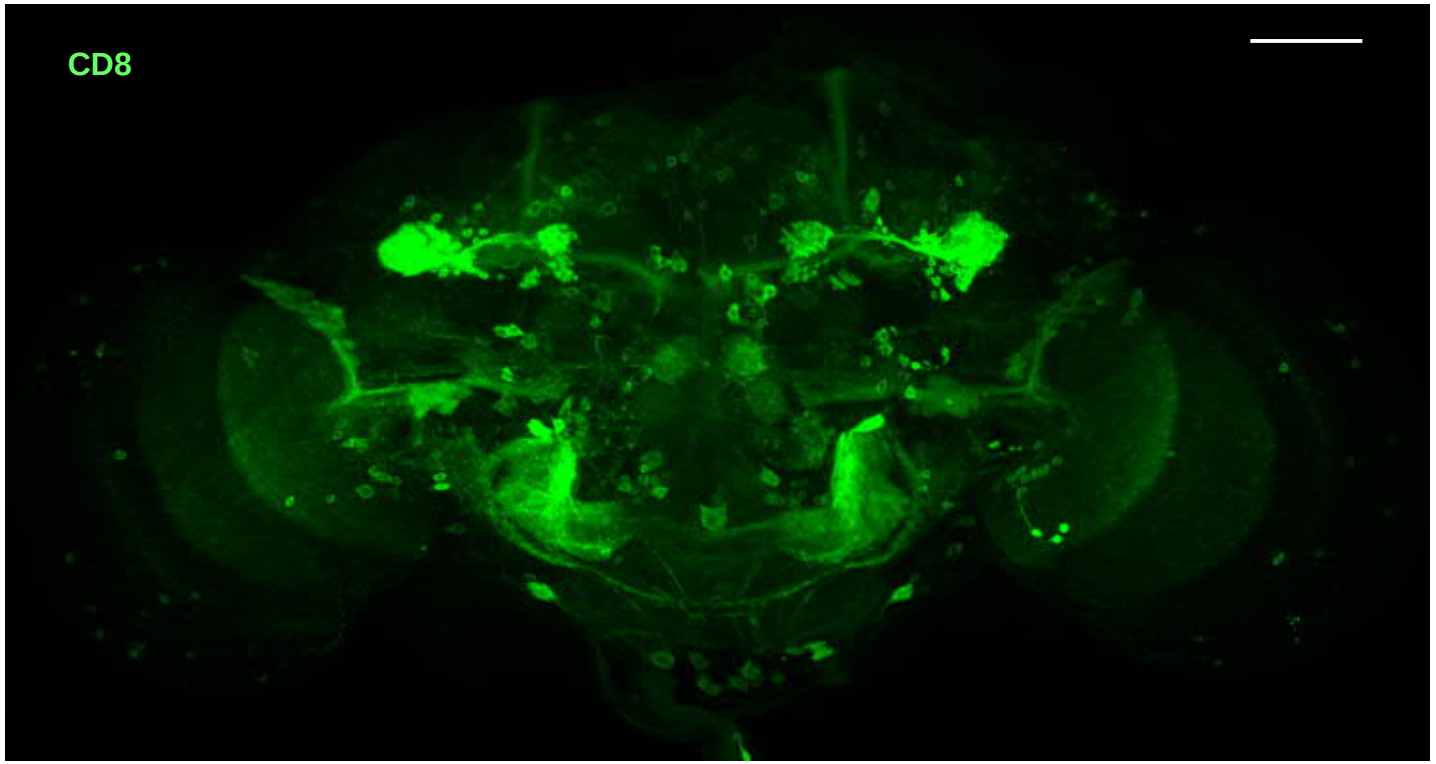

R55A05>mCD8-Cherry

Yalgin et al, Figure S15

A

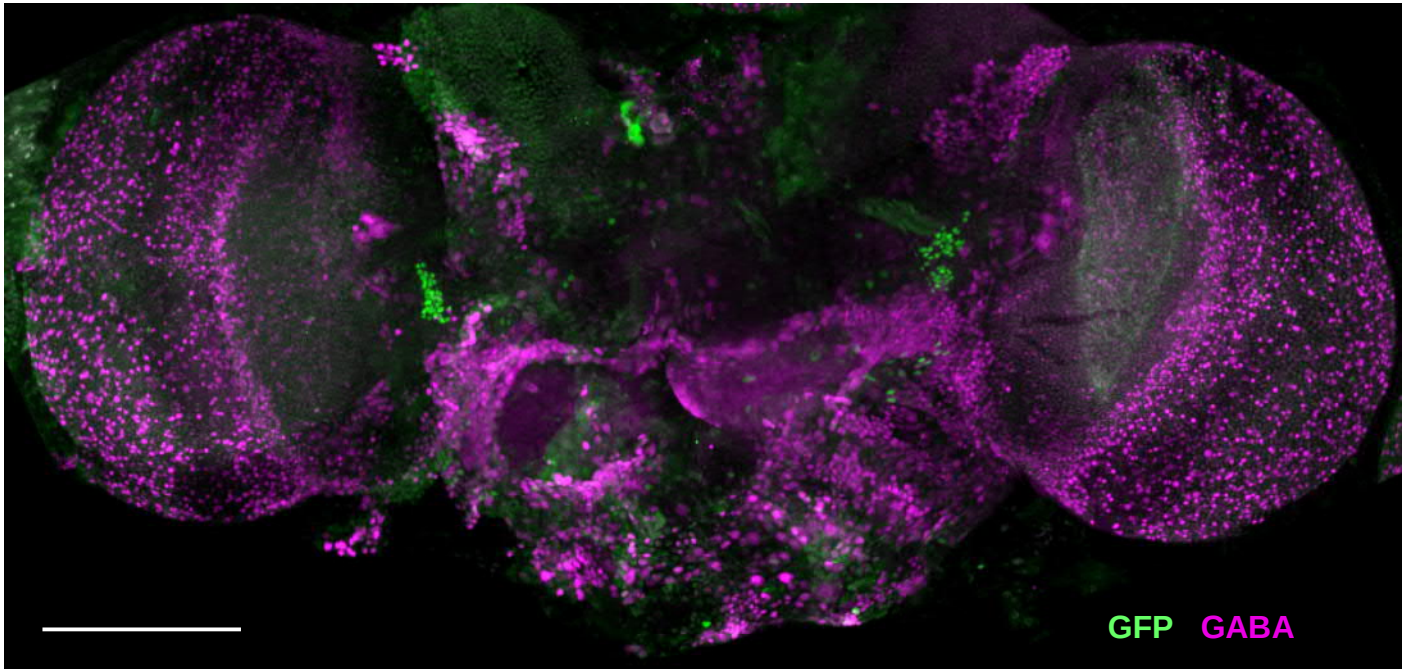

B

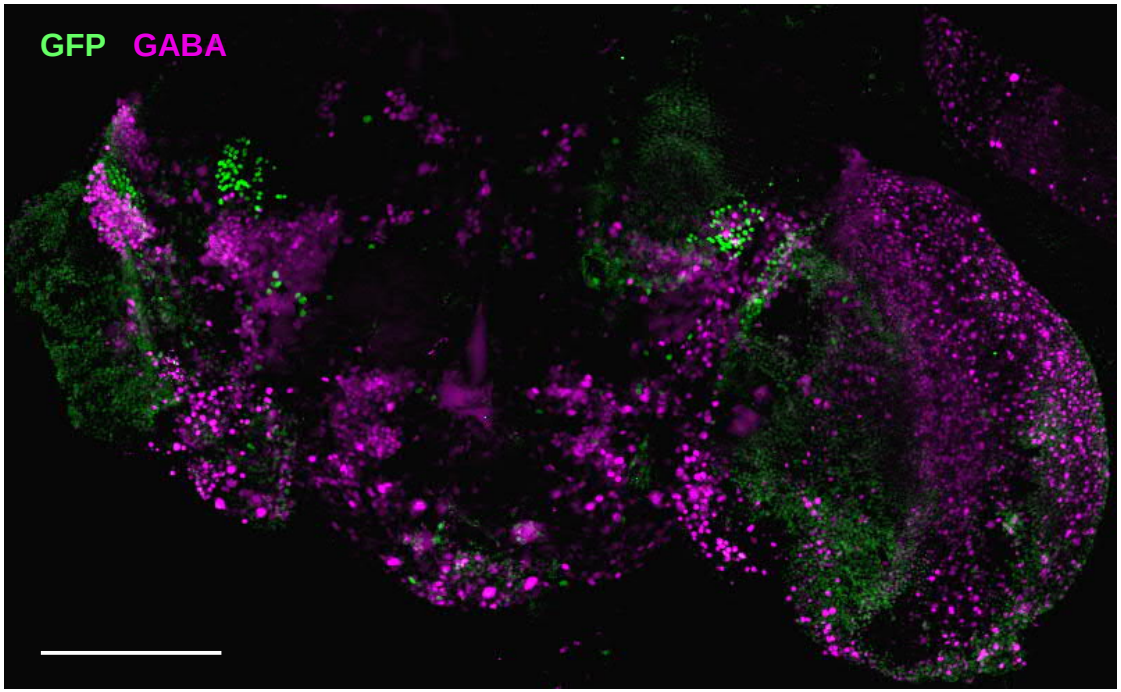

R55A05>nGFP

Yalgin et al, Figure S16

A

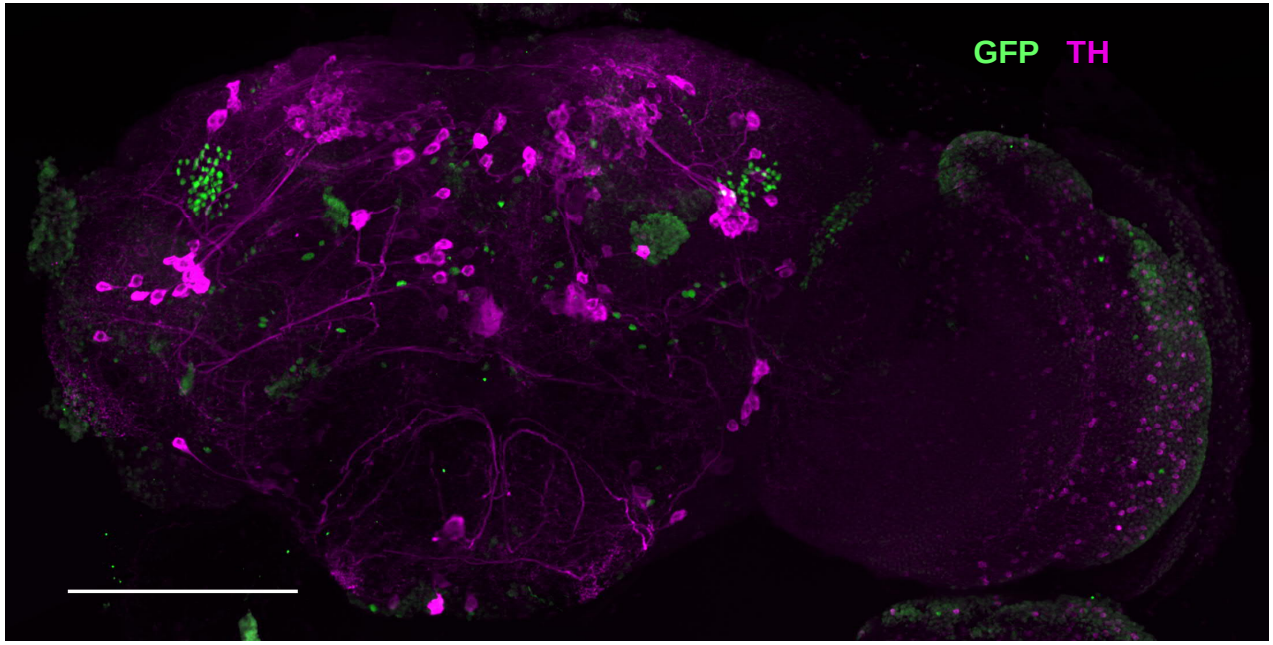

R55A05>nGFP

B

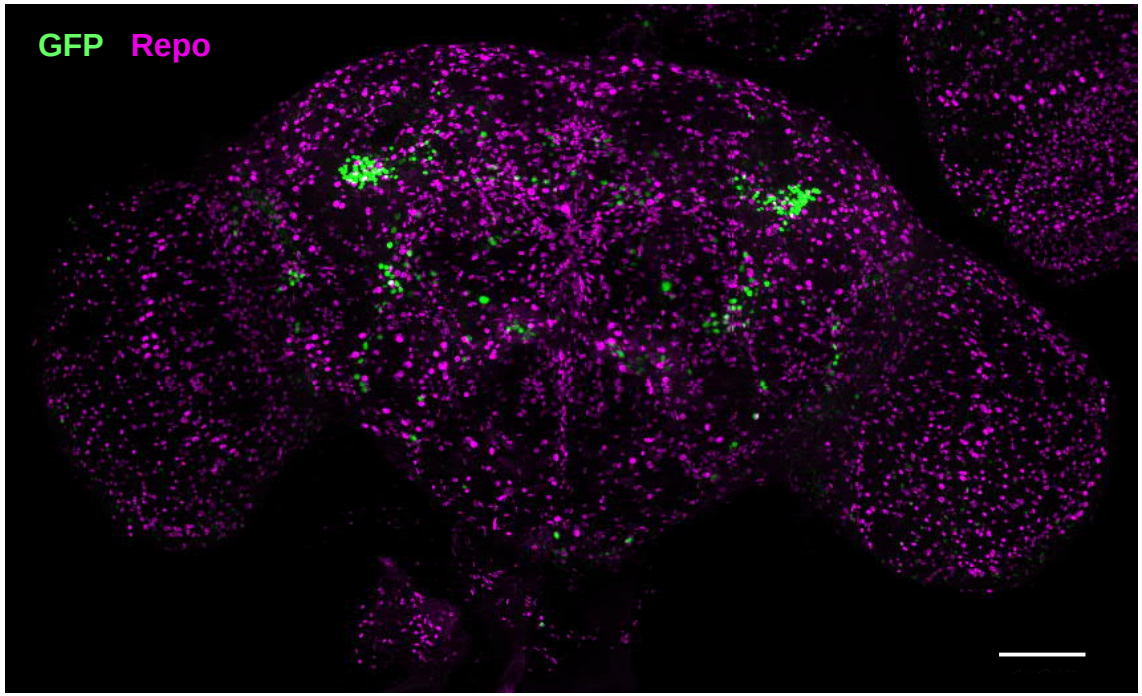

Yalgin et al, Figure S17

R55A05>mCD8-GFP

R59E04>mCD8-GFP

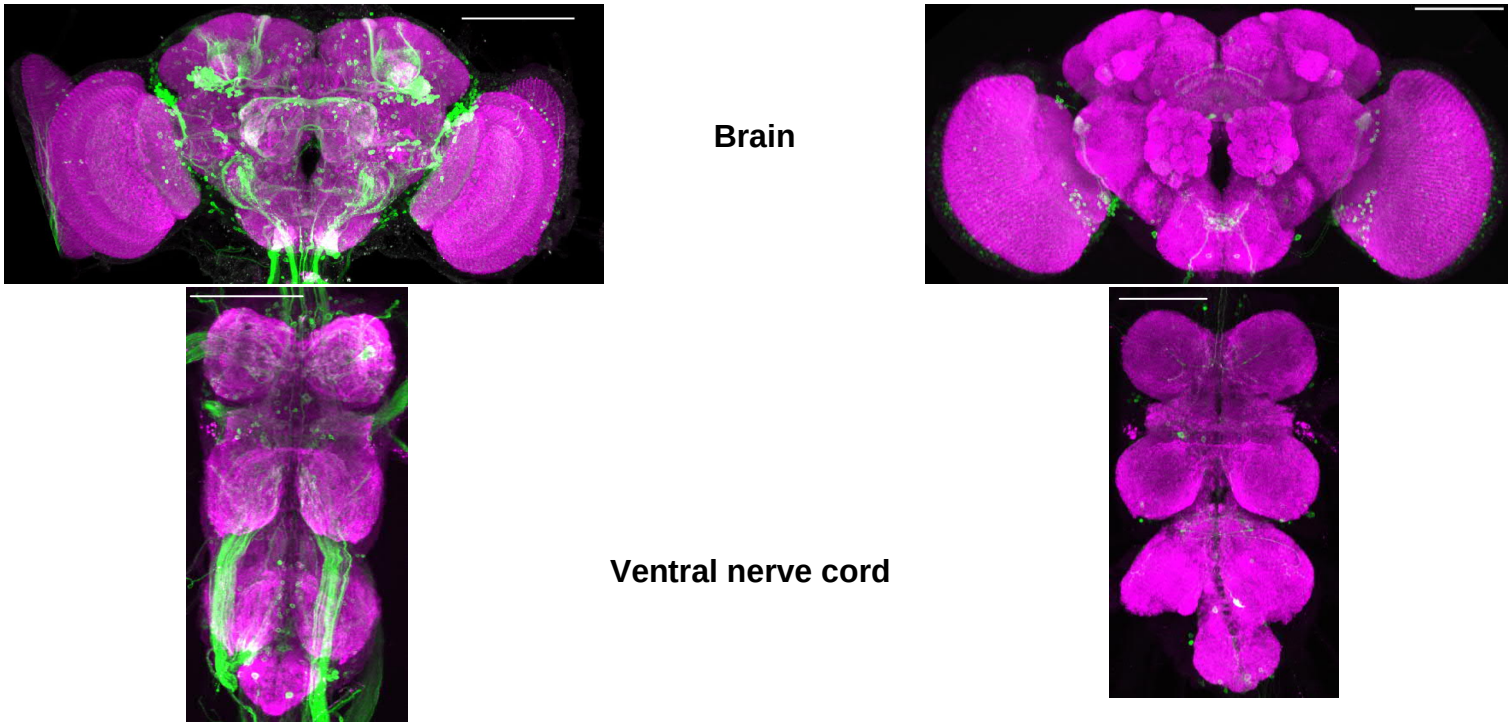

GFP **Bruchpilot**

Images reproduced from publicly available Janelia Flylight website: see legend

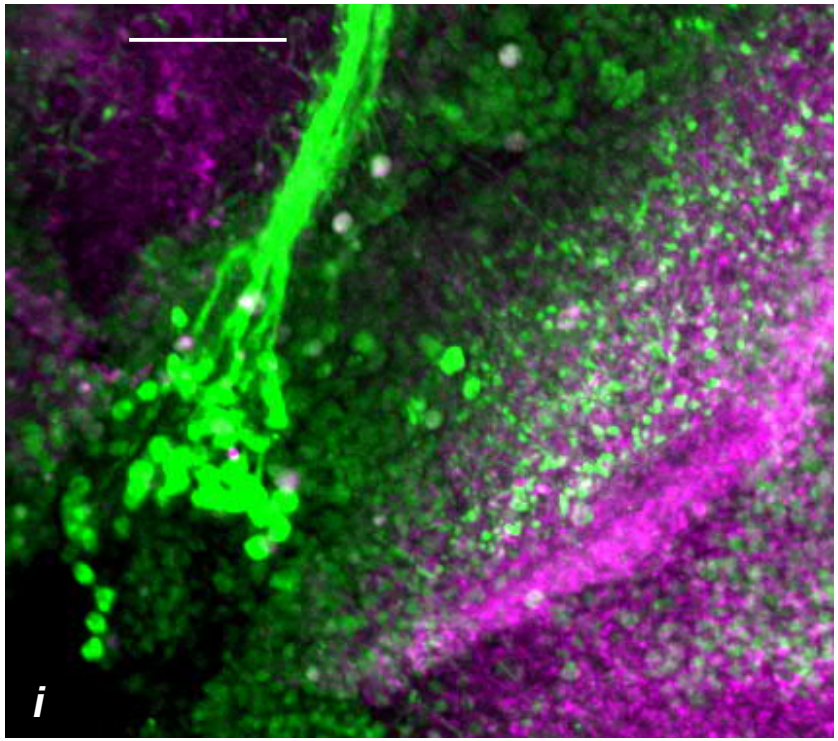

R59E04>mCD8-GFP

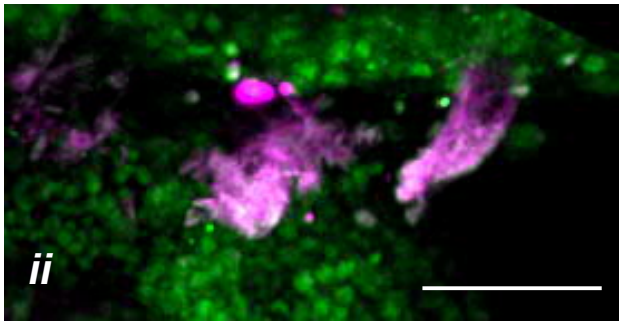

GFP

ChAT

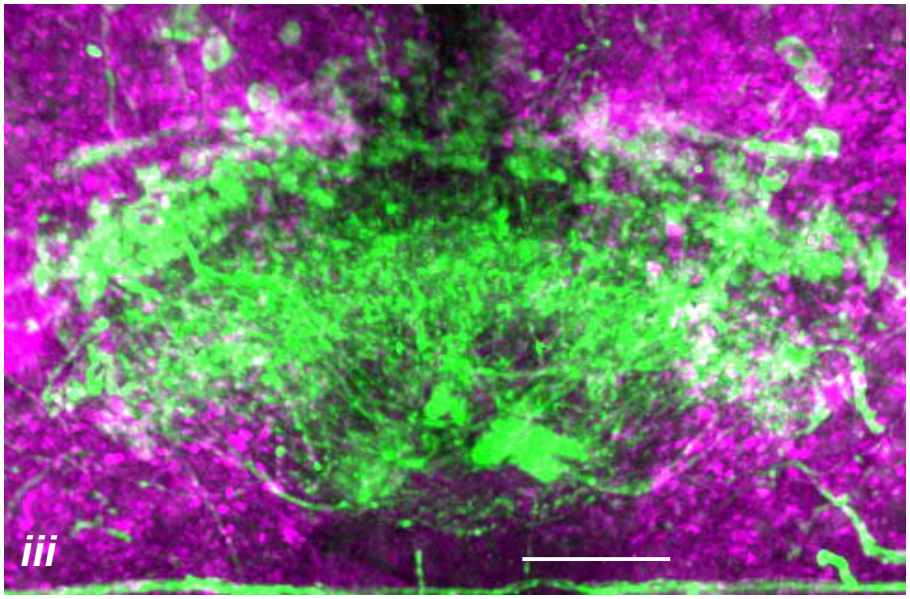

Yalgin et al, Figure S19

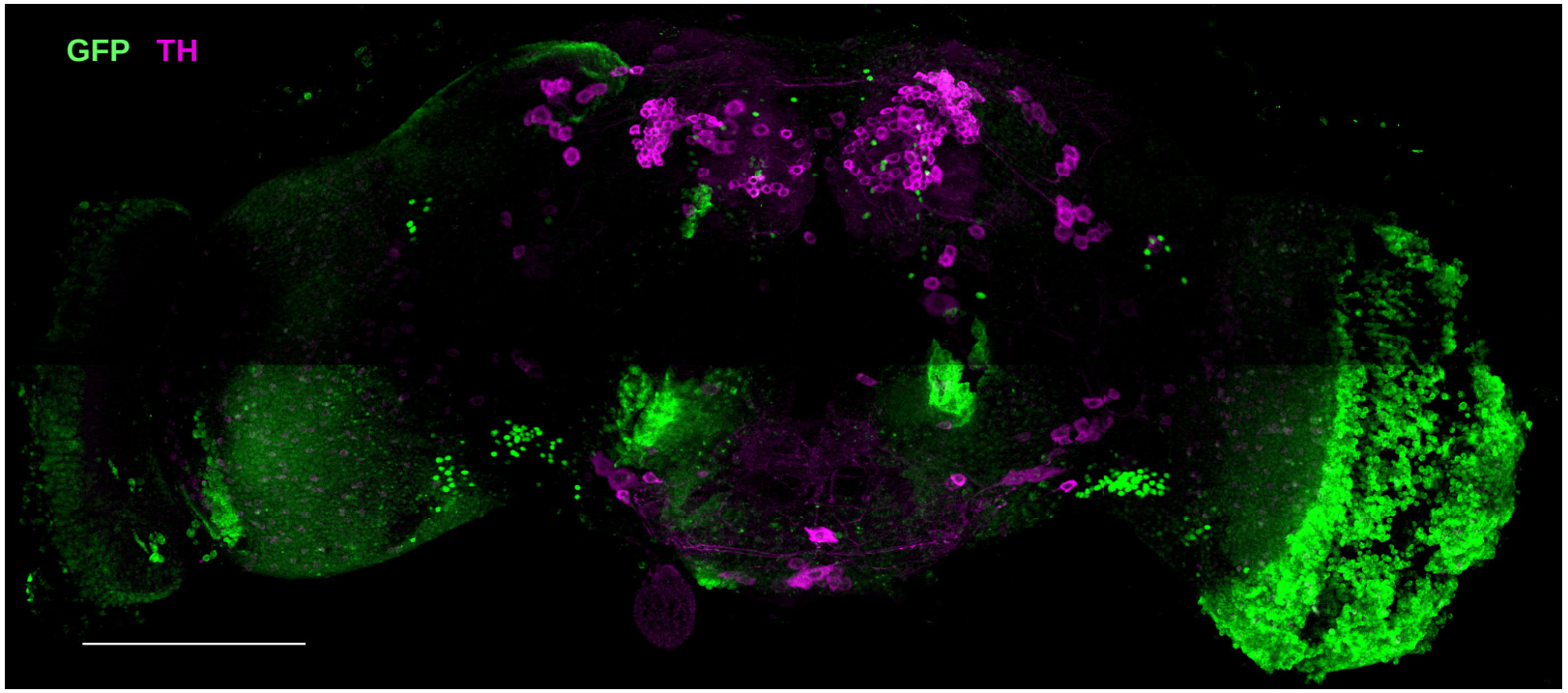

R59E04>nGFP

Yalgin et al, Figure S20

A

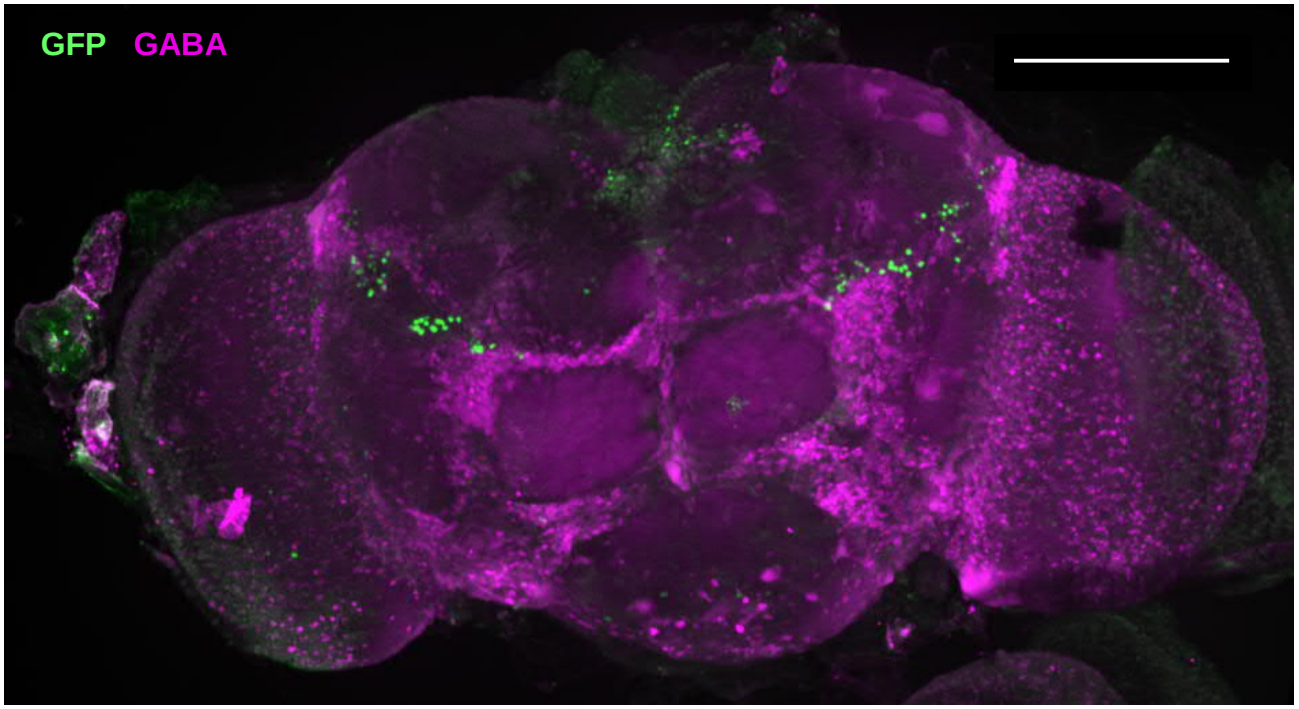

R51C09>nGFP

B

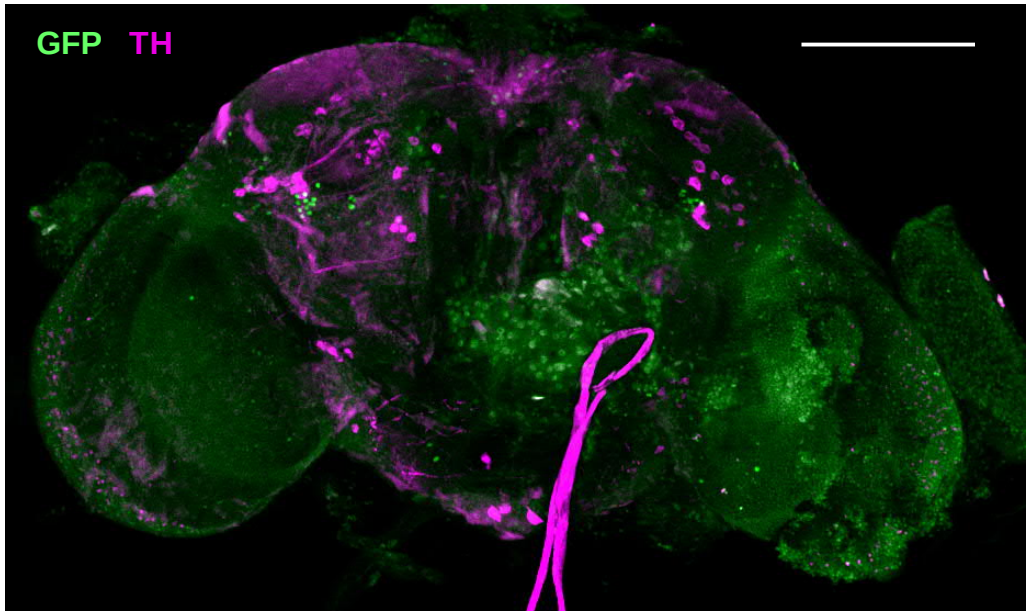

Yalgin et al, Figure S21

A

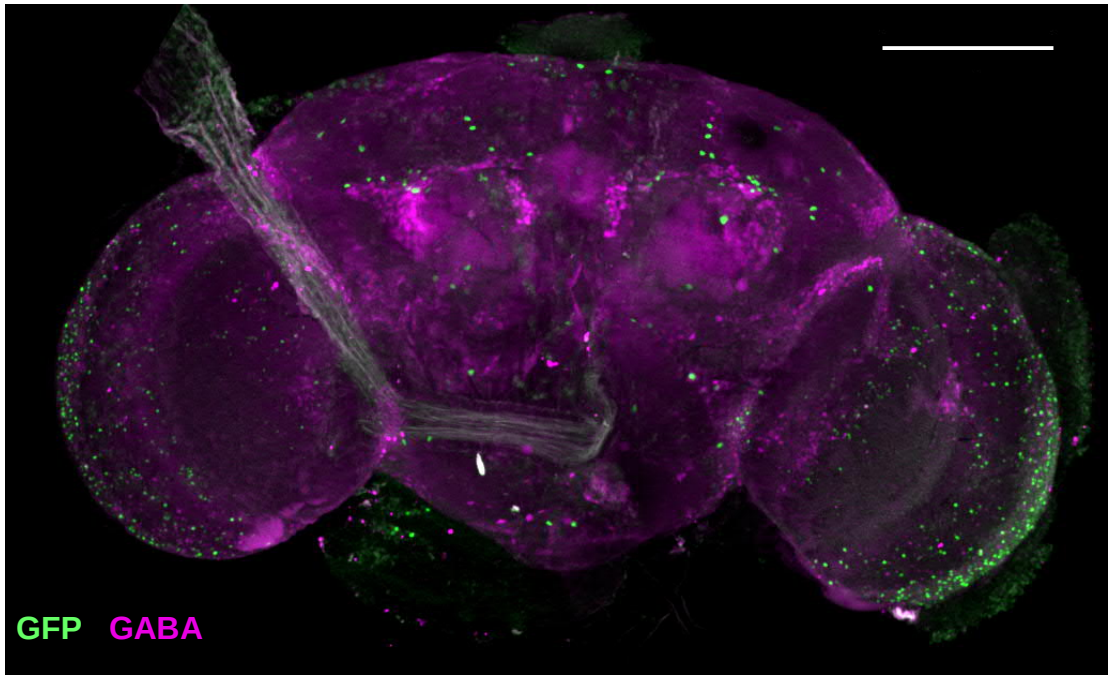

B

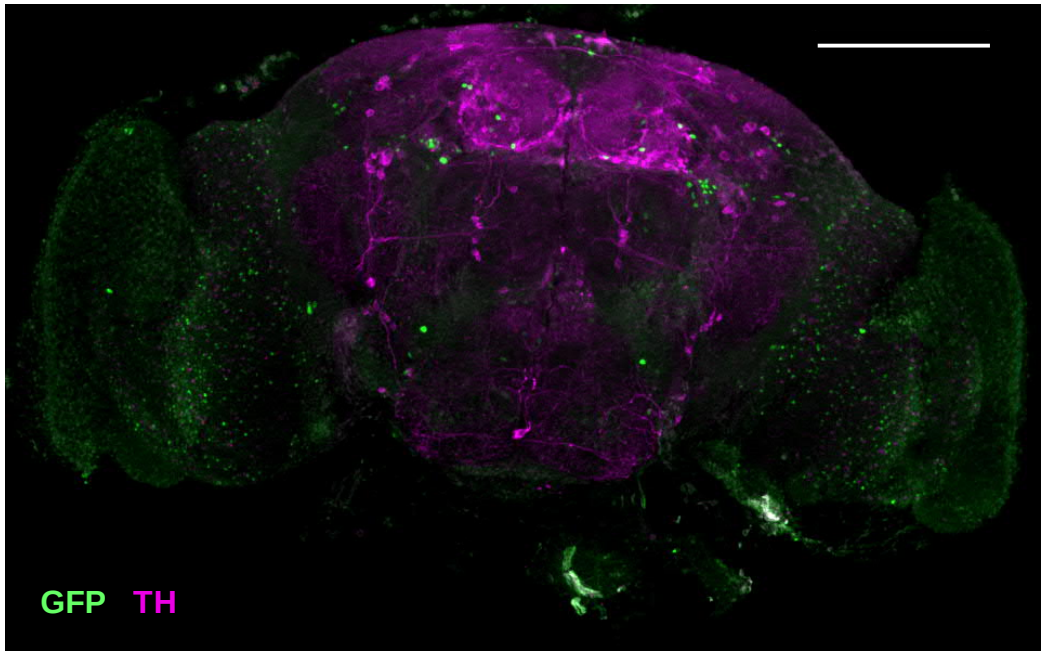

R52A01>nGFP

Yalgin et al, Figure S22

A

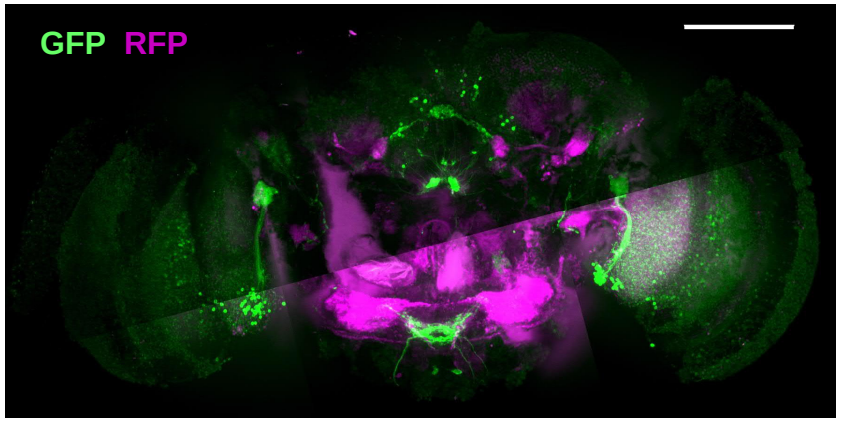

B

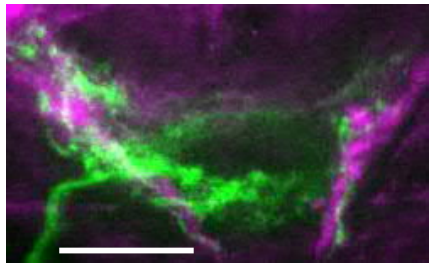

R59E04-LexA>mCD8-GFP
R55A05-GAL4>mCD8-RFP

D

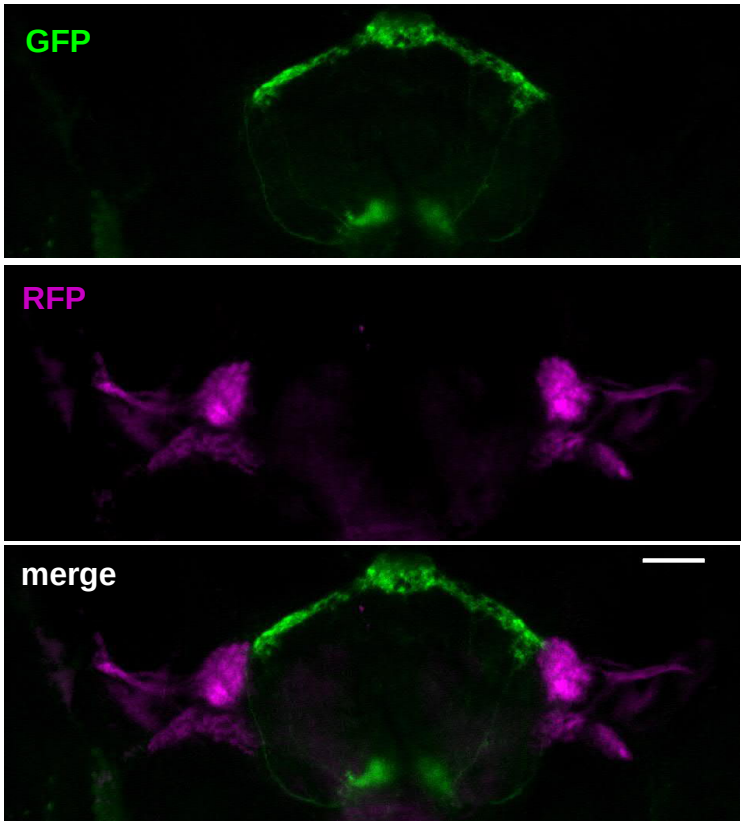

C

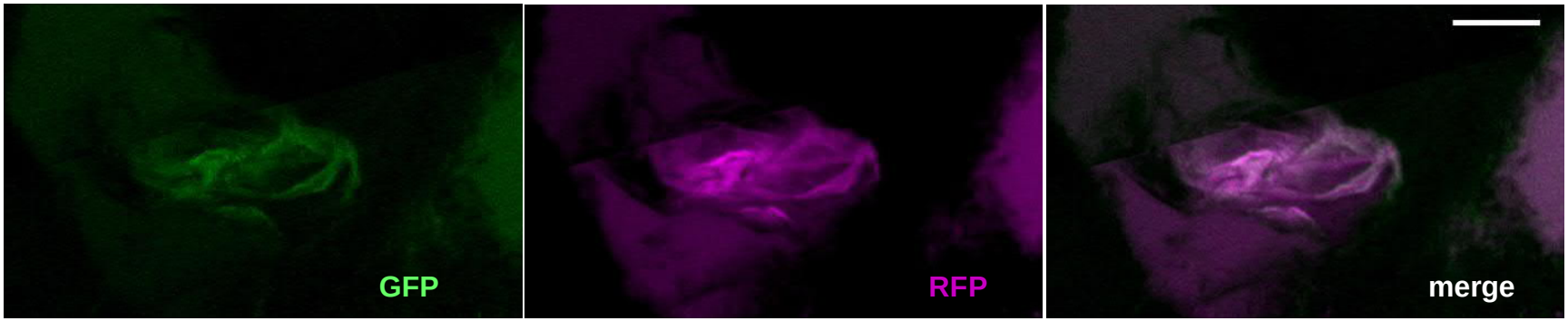

Yalgin et al, Figure S23

A

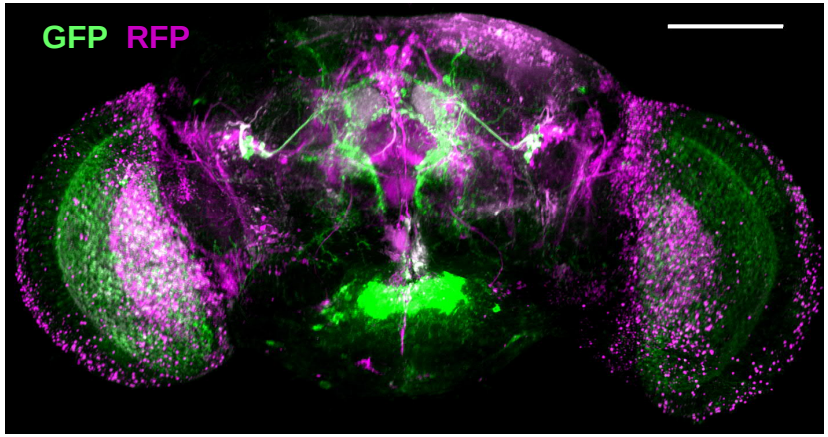

B

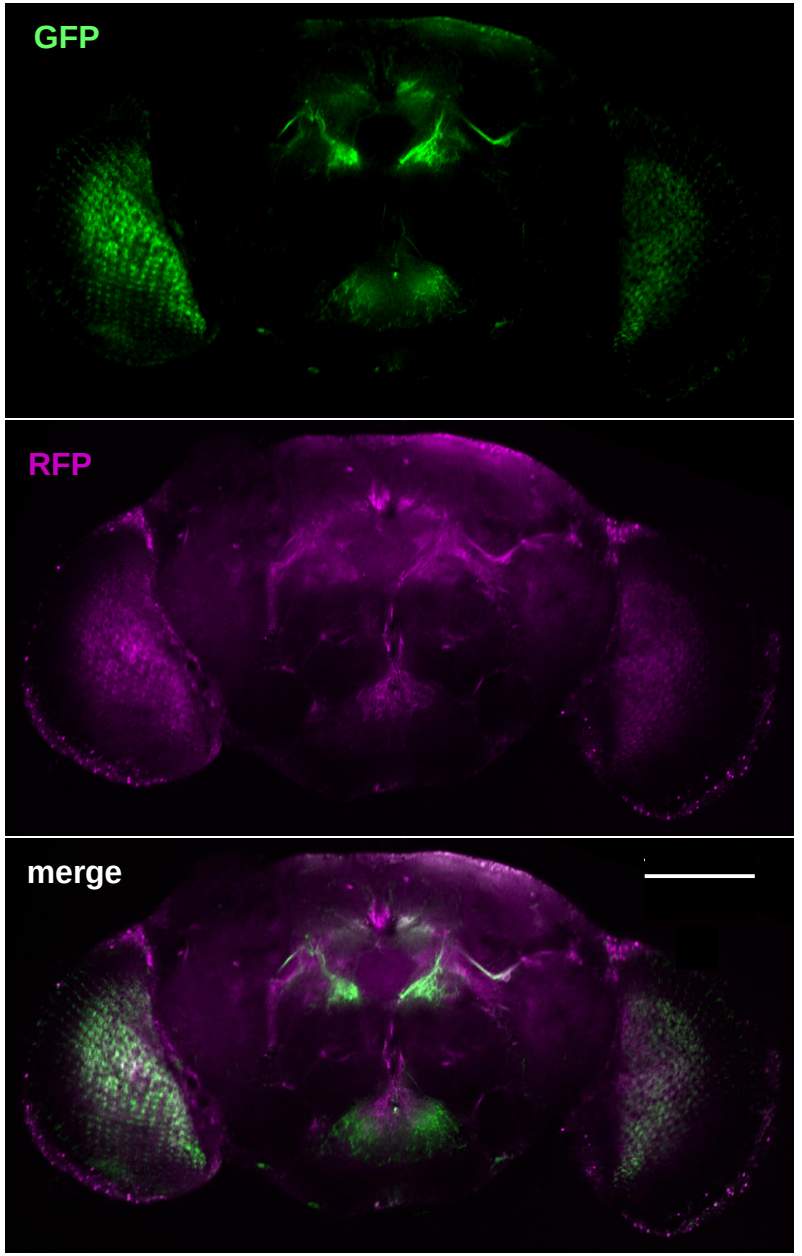

R52A01-LexA>mCD8-GFP
R51C09-GAL4>mCD8-RFP

C

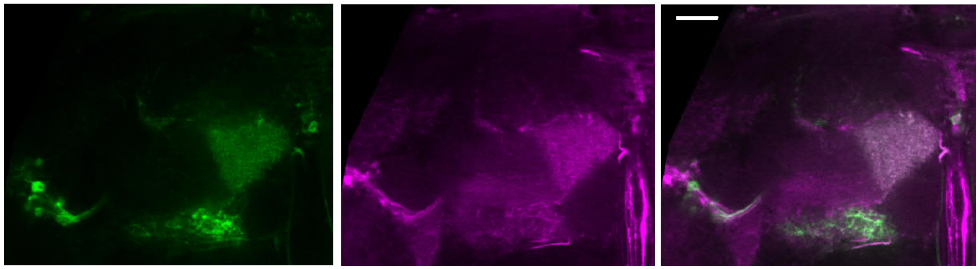

GFP RFP merge

Yalgin et al, Figure S24

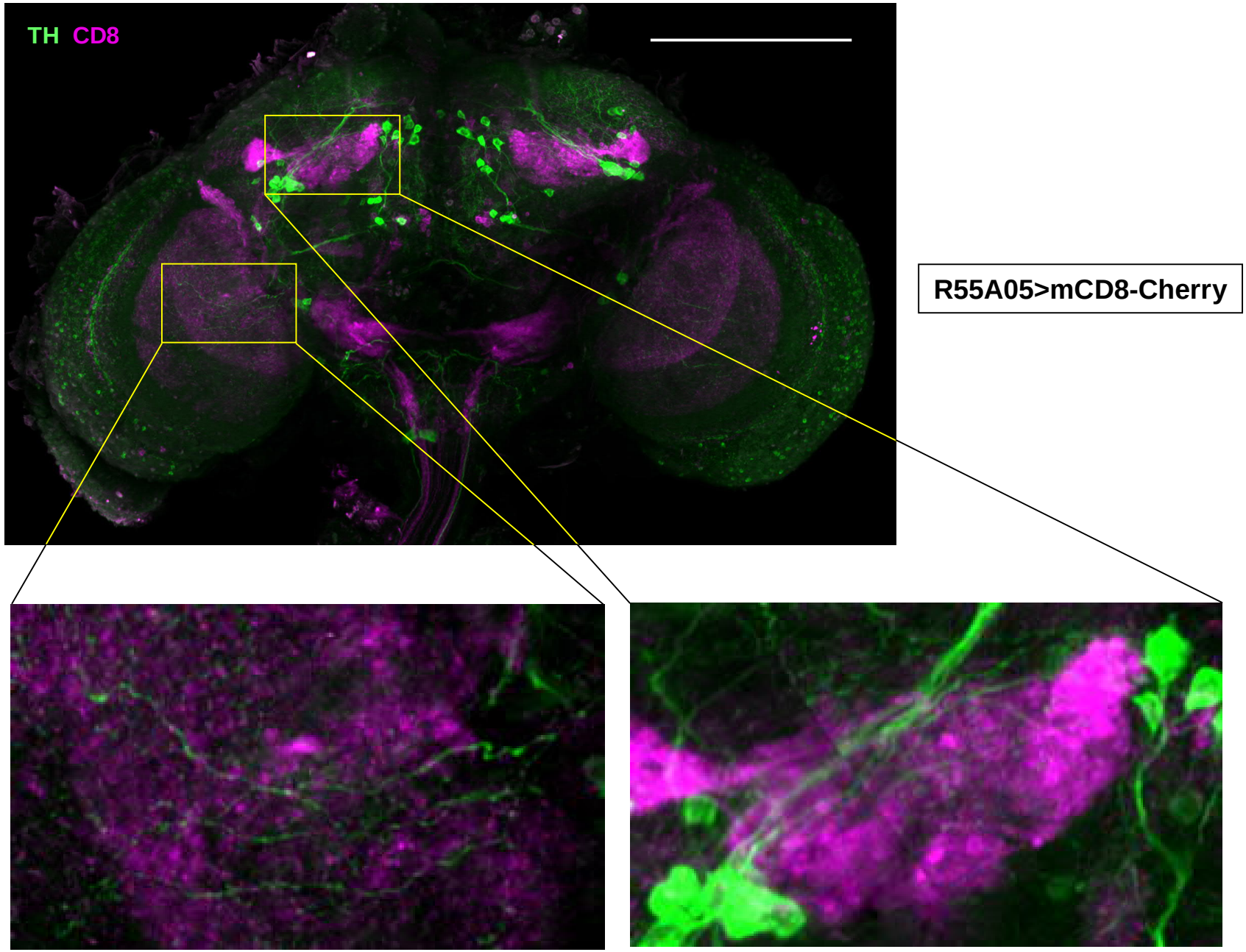

Yalgin et al, Figure S25

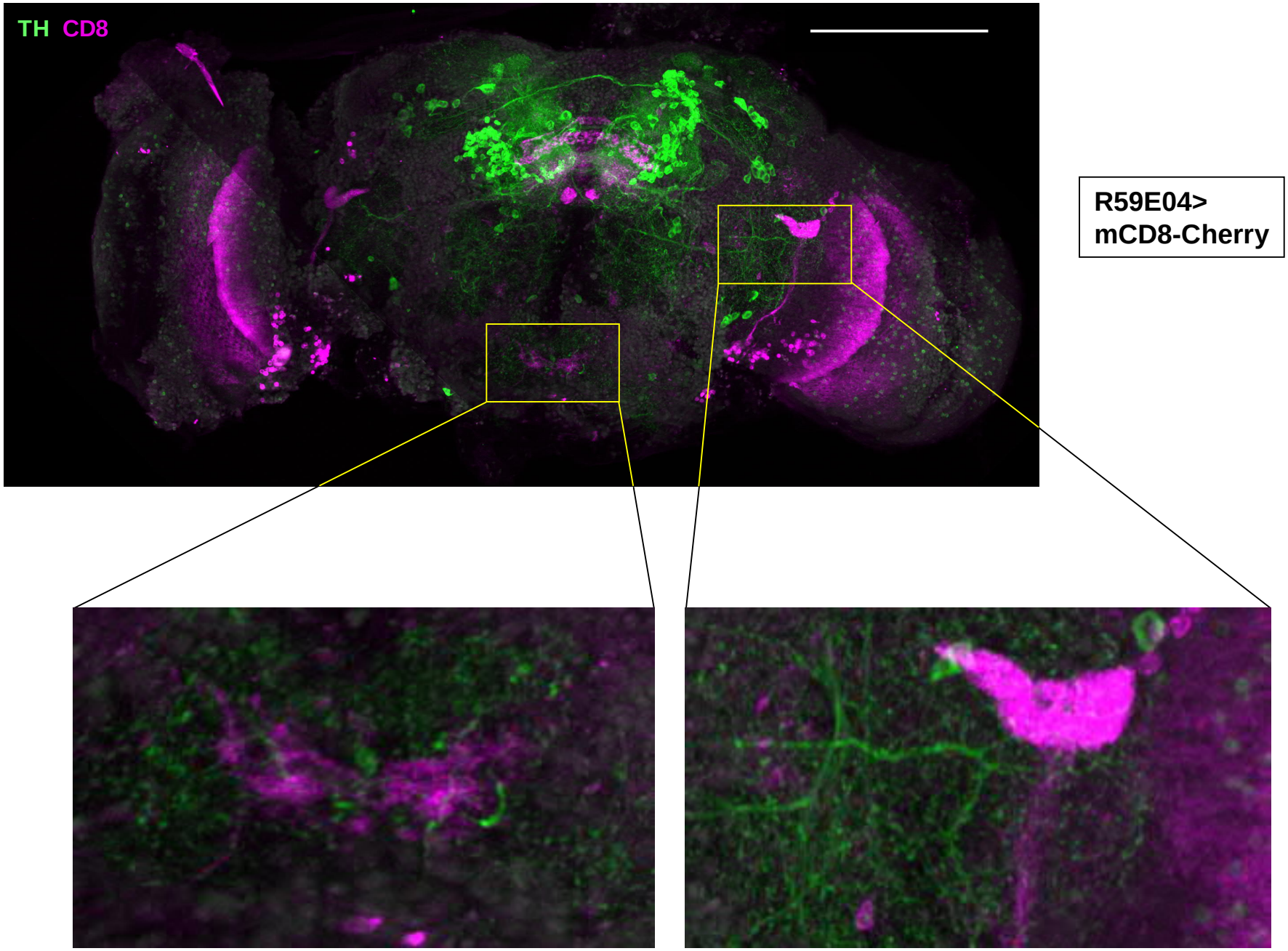

Yalgin et al, Figure S26

panels *v* and *iii* of Figure 7

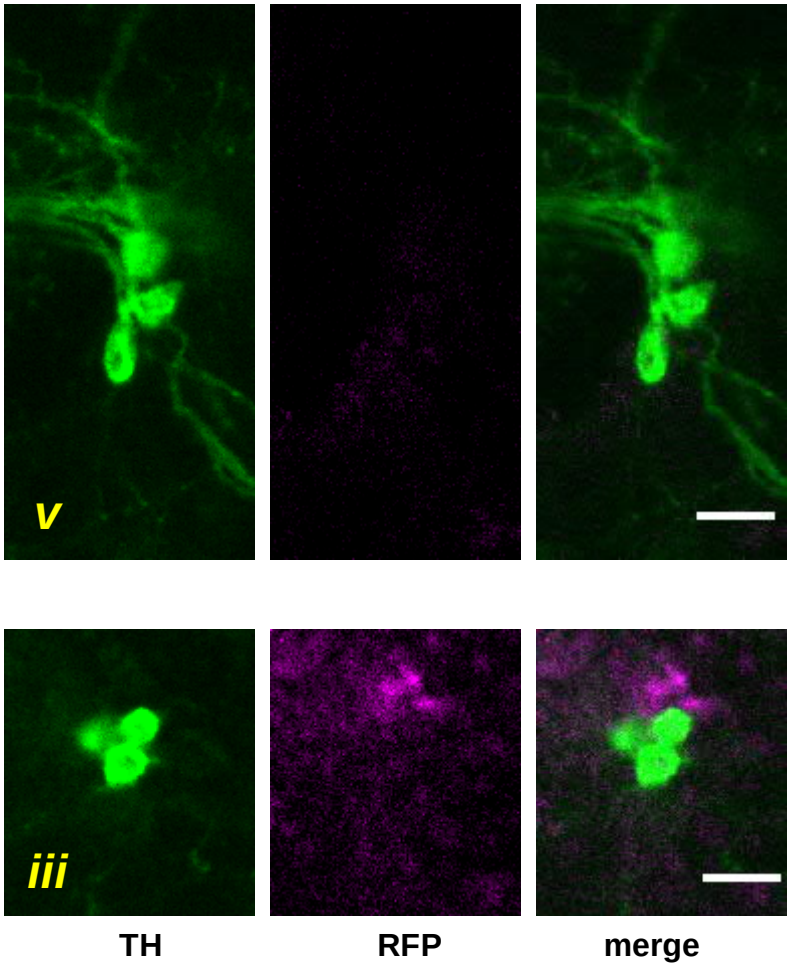

R55A05>trans-Tango

Yalgin et al, Figure S27

panels *ii*, *x* and *vii* of Figure 7

R55A05>trans-Tango

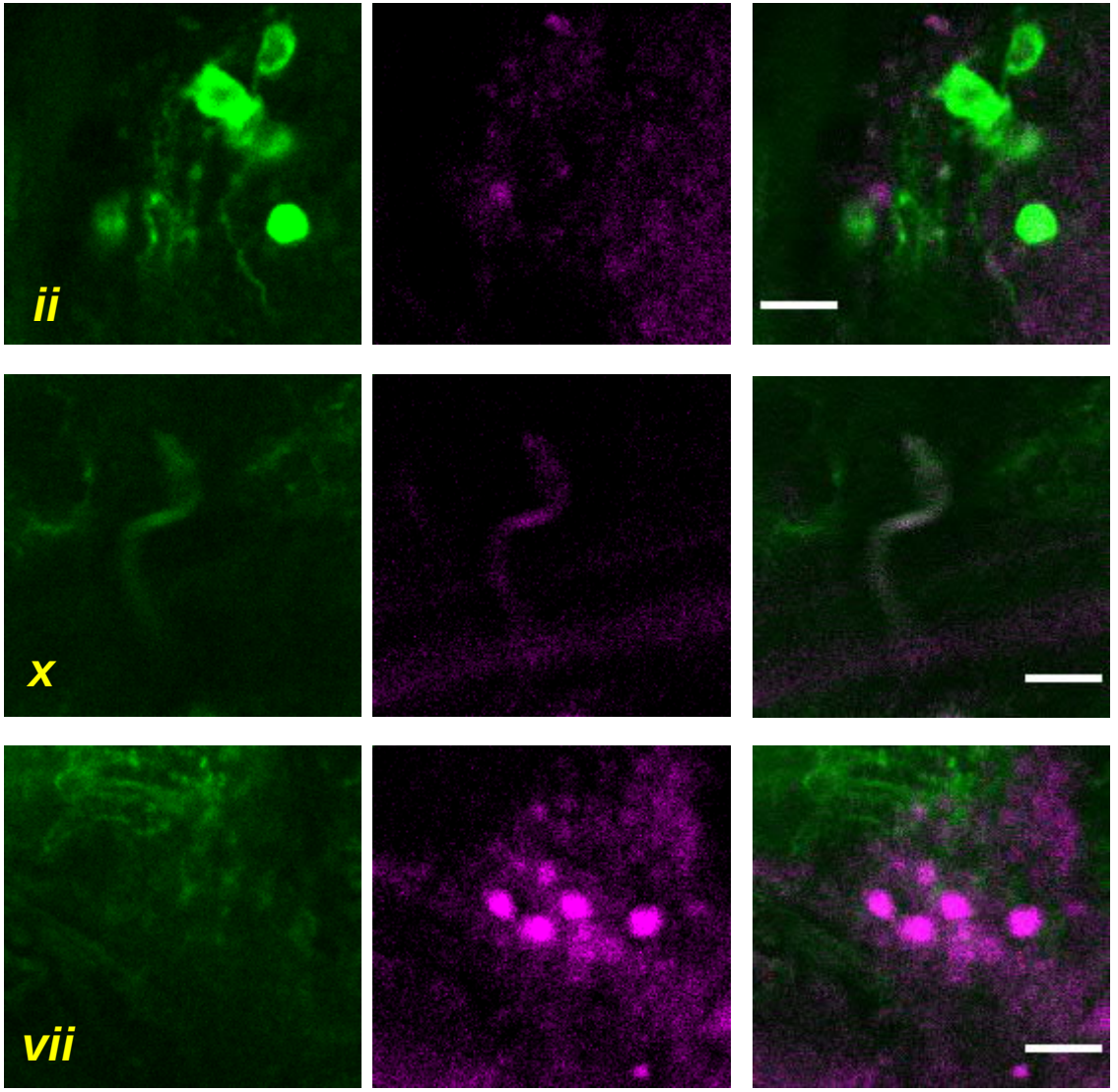

Yalgin et al, Figure S28

panel *xii* of Figure 7

R55A05>trans-Tango

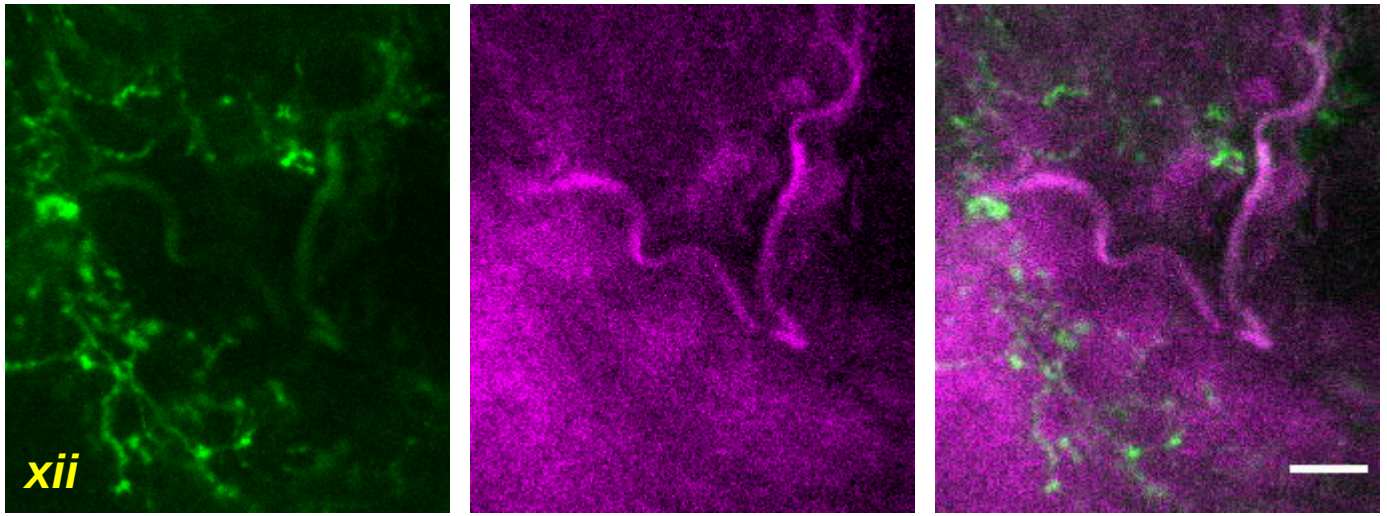

TH **RFP** **merge**

panels *v* and *iii* of Figure 7

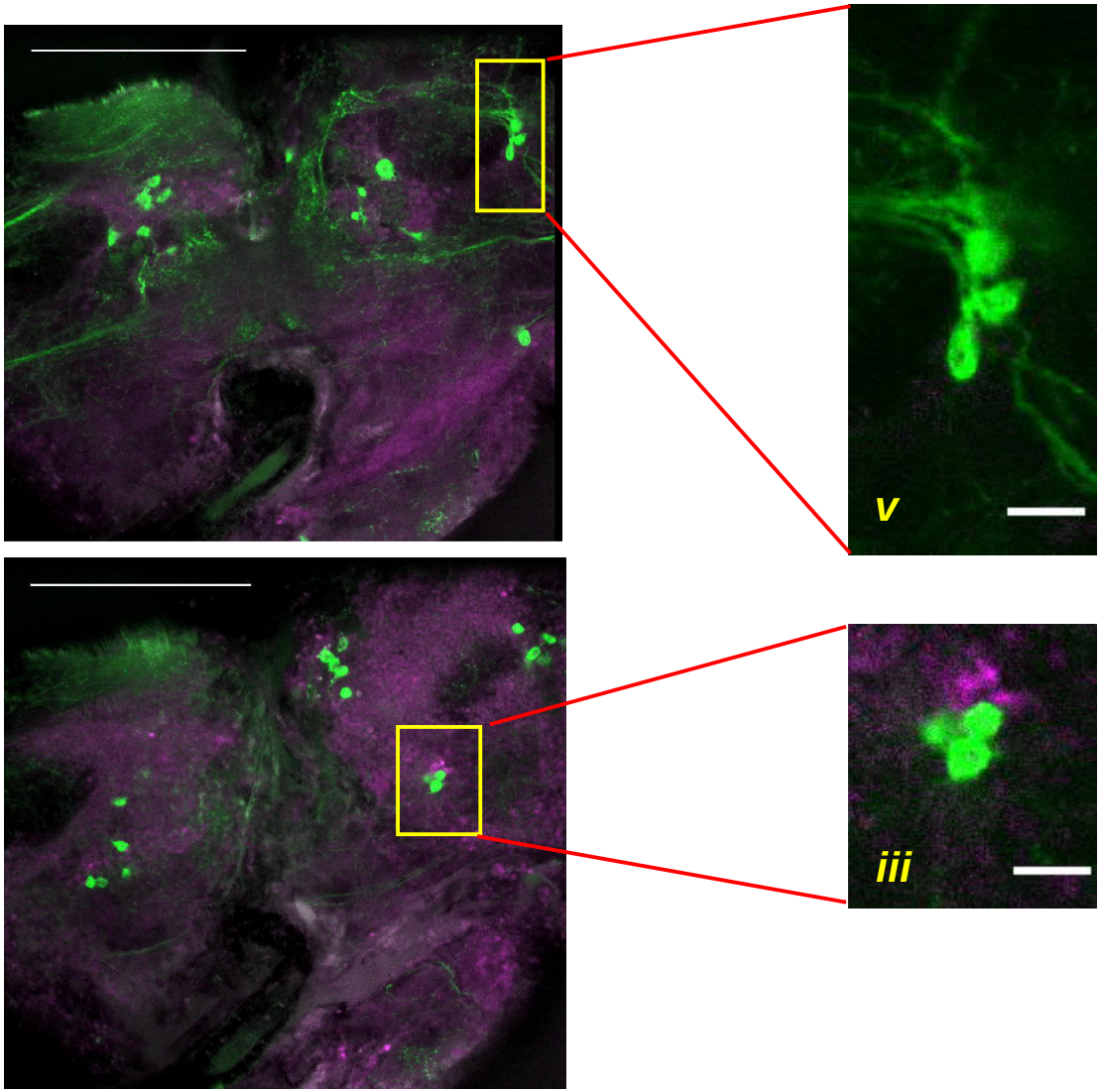

R55A05>trans-Tango

Yalgin et al, Figure S30

panels *i*, *ii* and *iv* of Figure 7

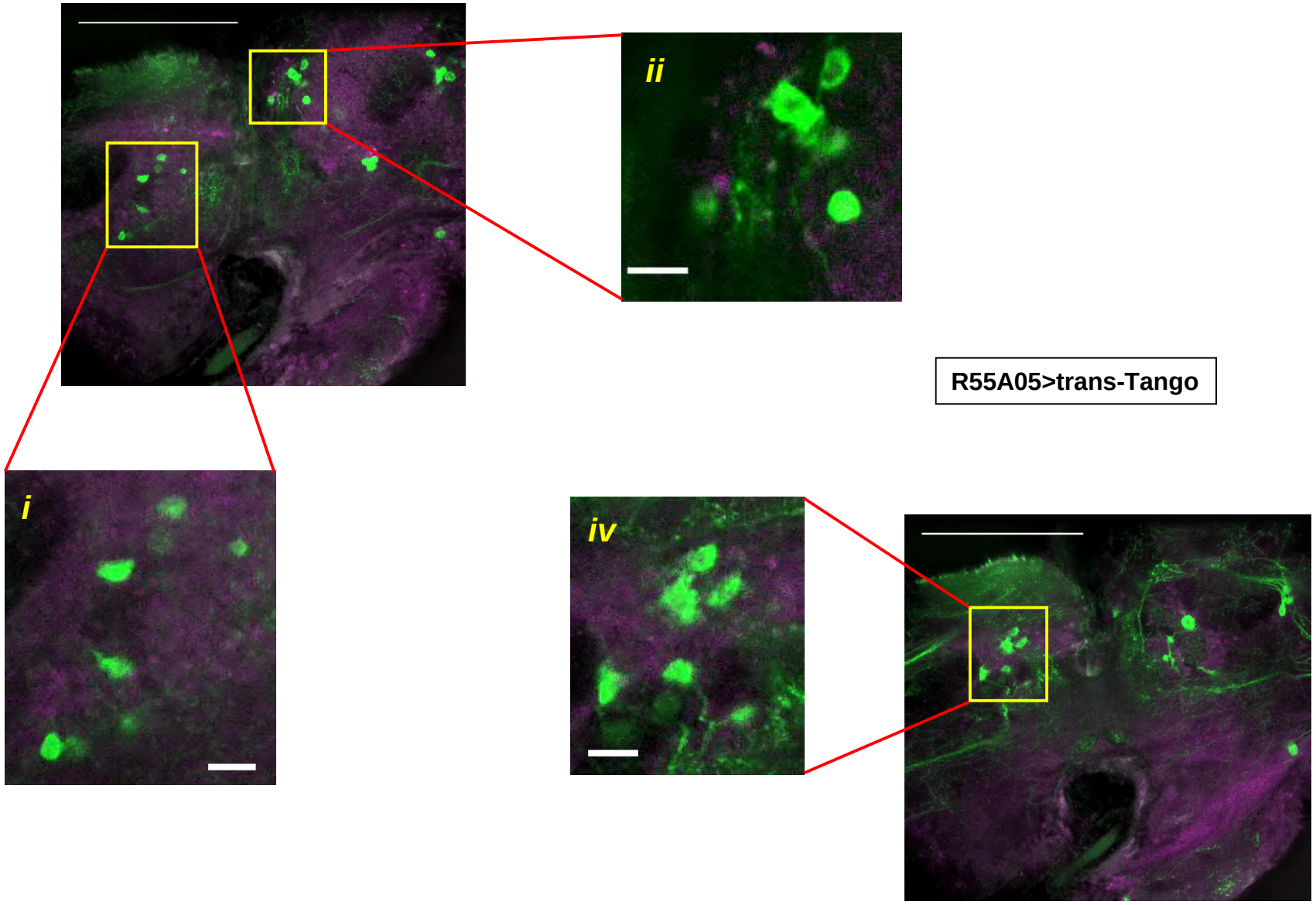

Yalgin et al, Figure S31

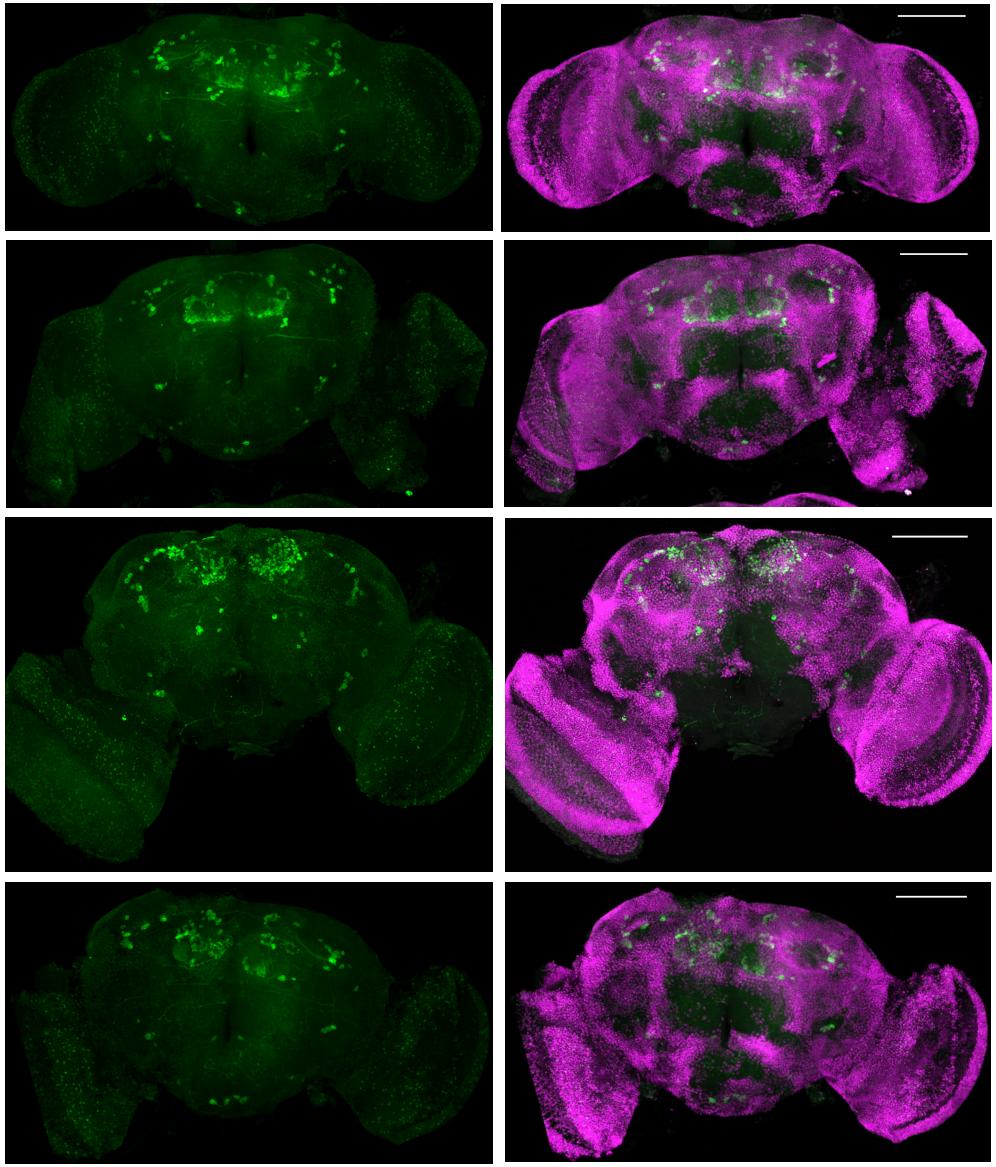

R55A05>Dcr2 only

TH

Elav

Yalgin et al, Figure S32

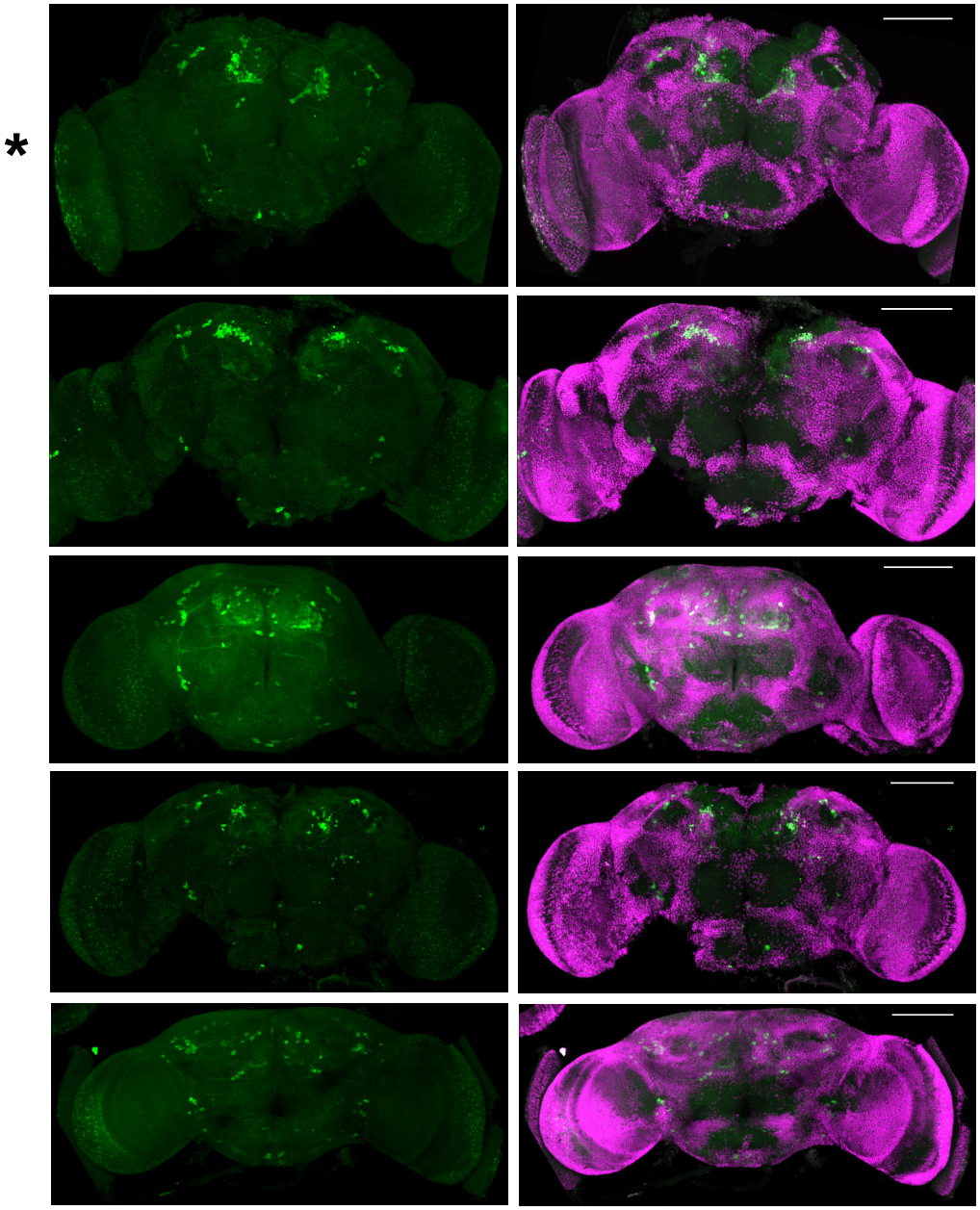

Yalgin et al, Figure S33

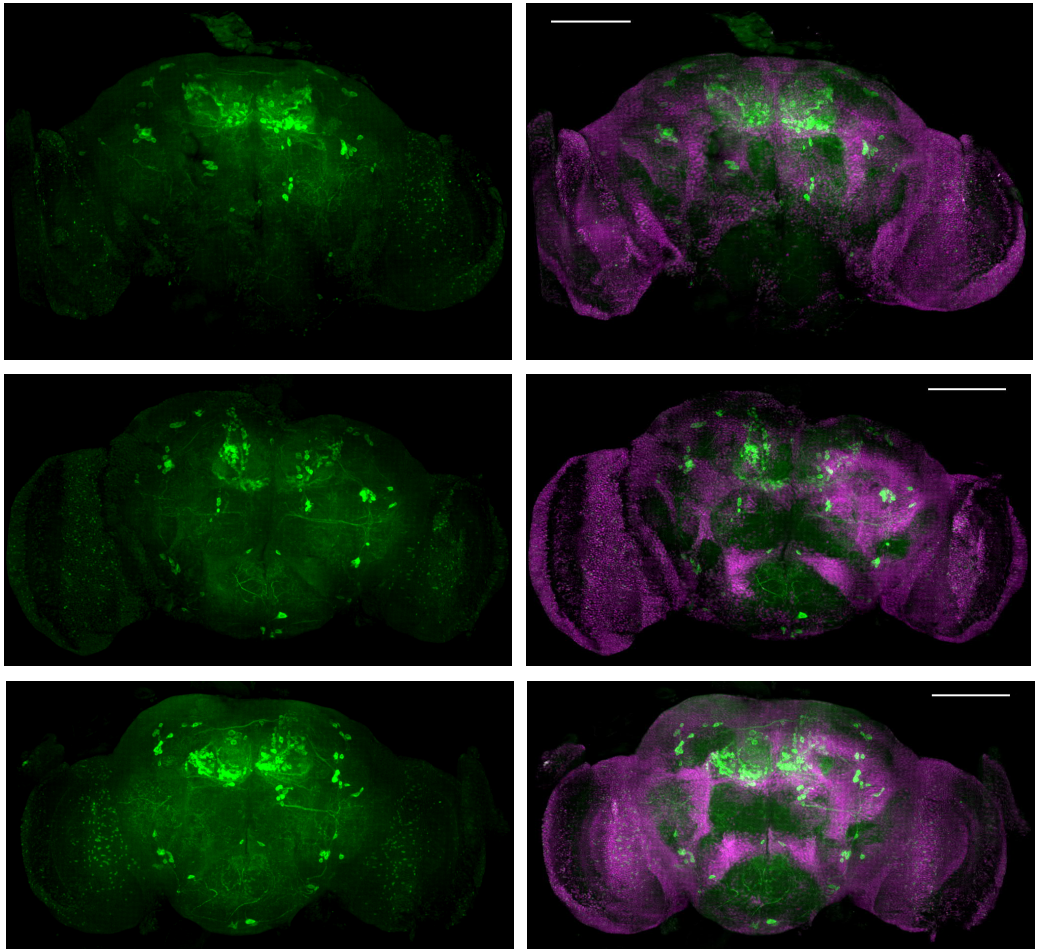

*

R59E04>Dcr2 only

TH

Elav

Yalgin et al, Figure S34

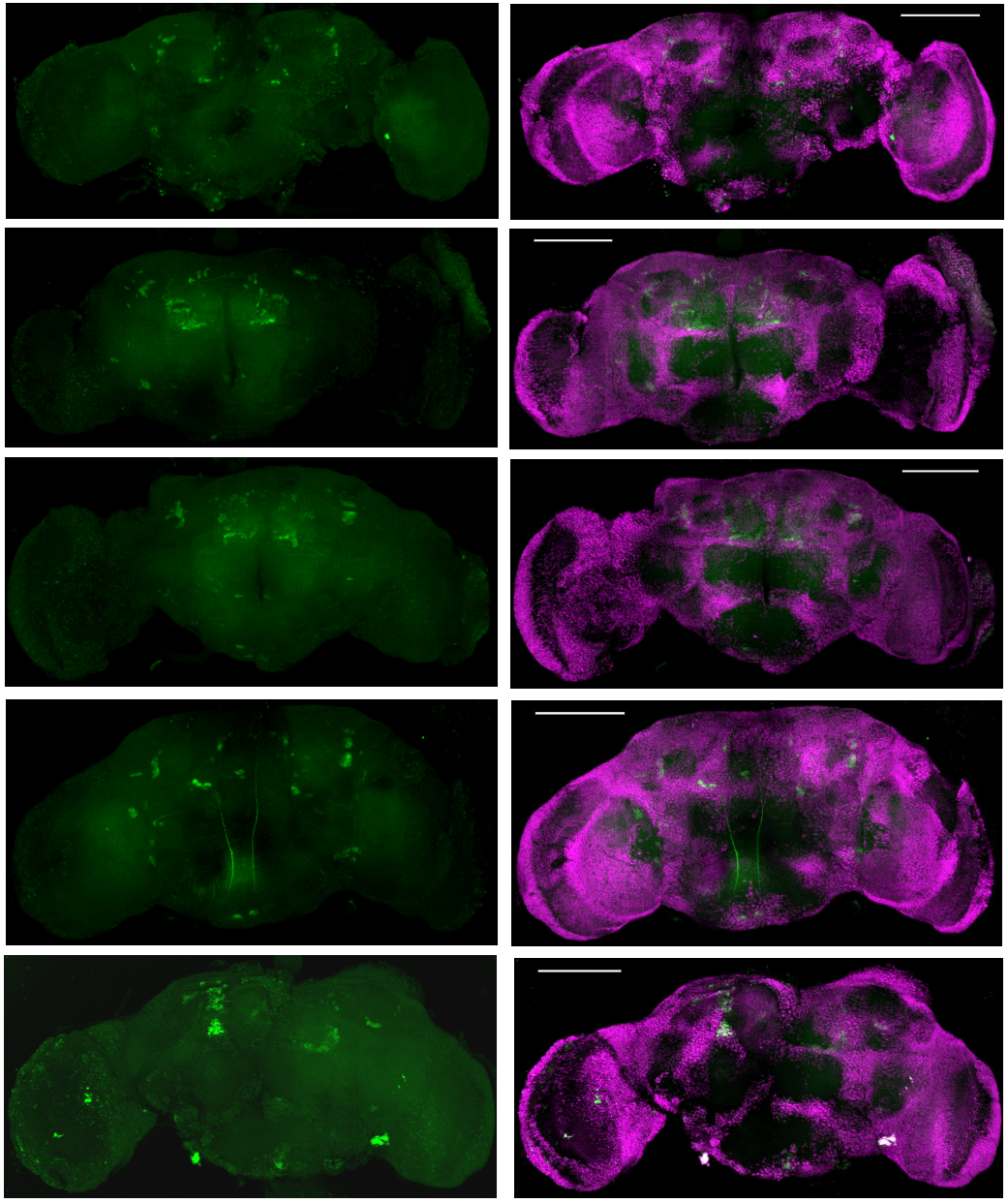

*

R59E04>COX7A-KD

TH

Elav

Yalgin et al, Figure S35

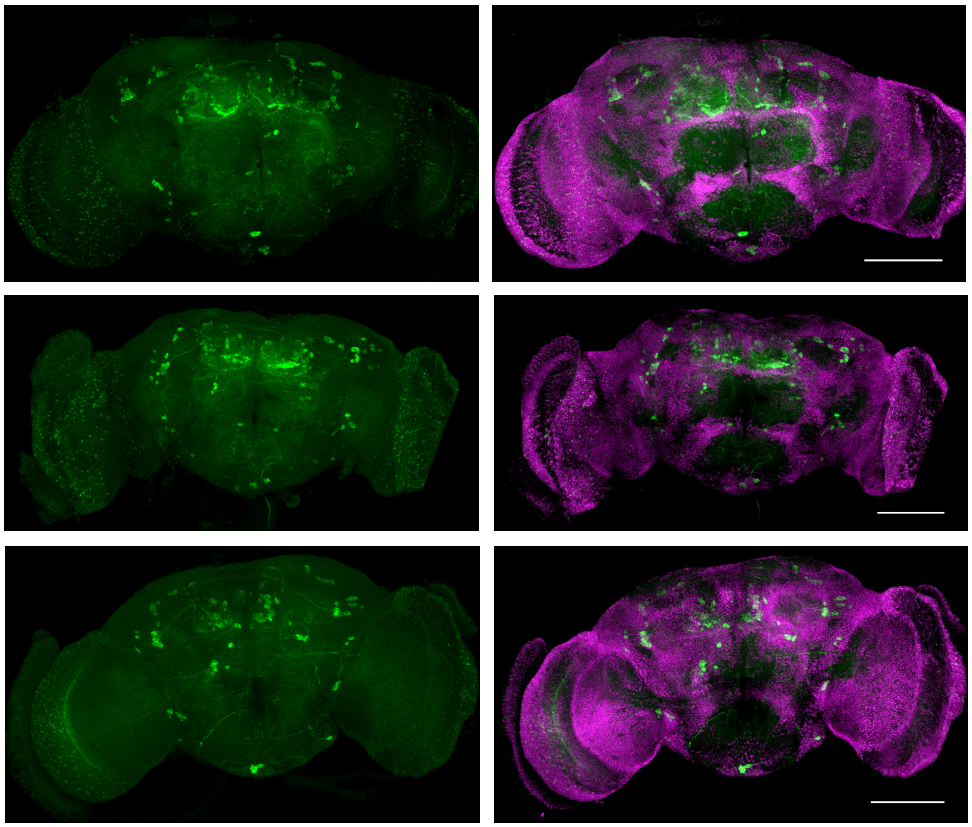

R52A01>Dcr2 only

TH

Elav

Yalgin et al, Figure S36

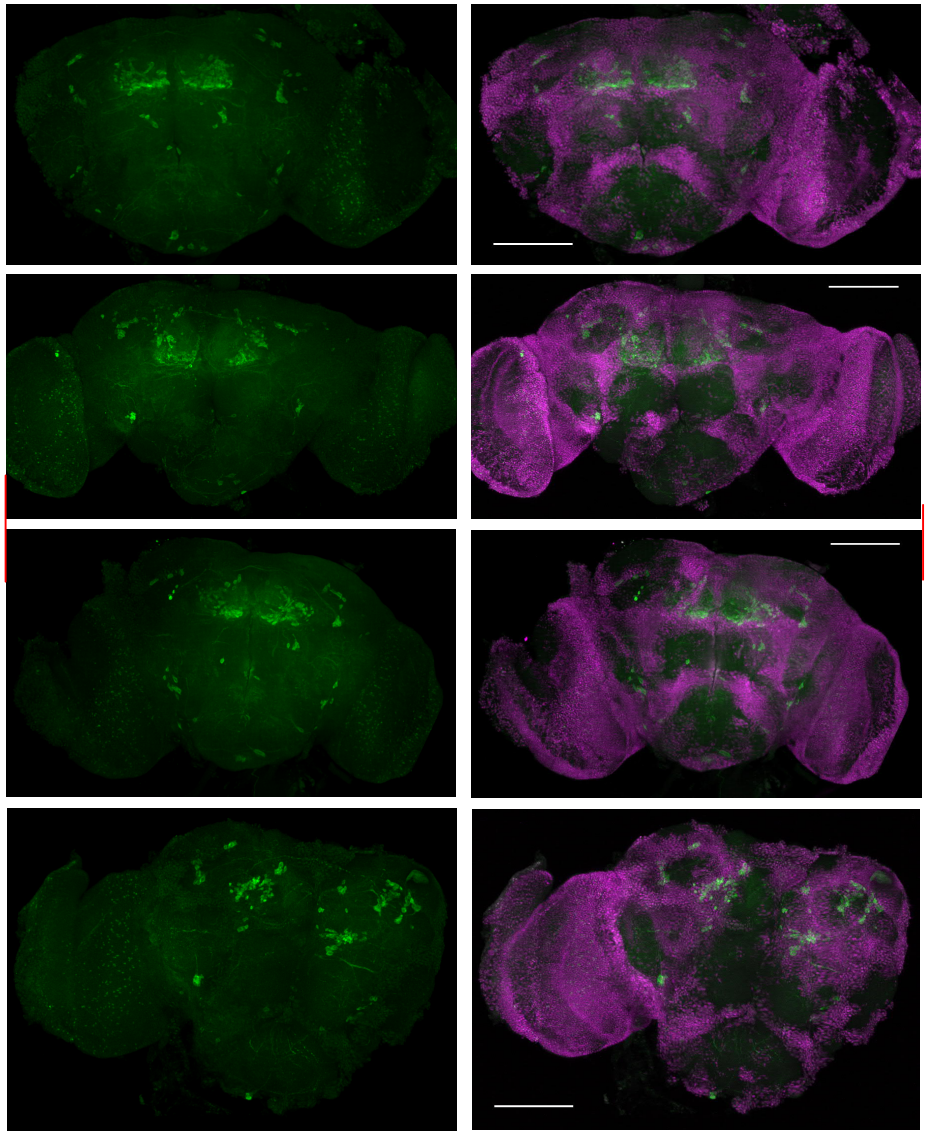

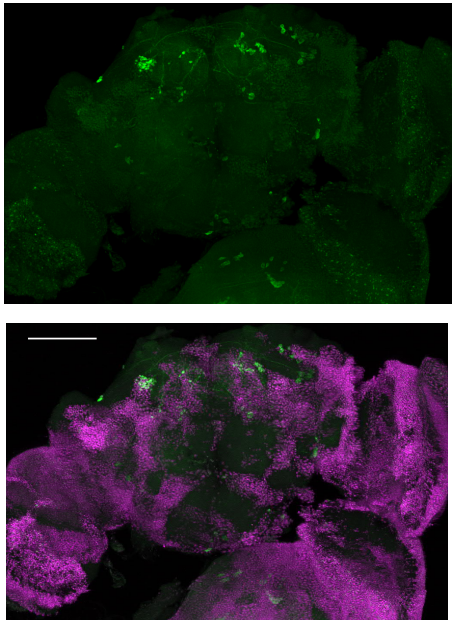

R52A01>COX7A-KD

TH

Elav

Yalgin et al, Figure S37

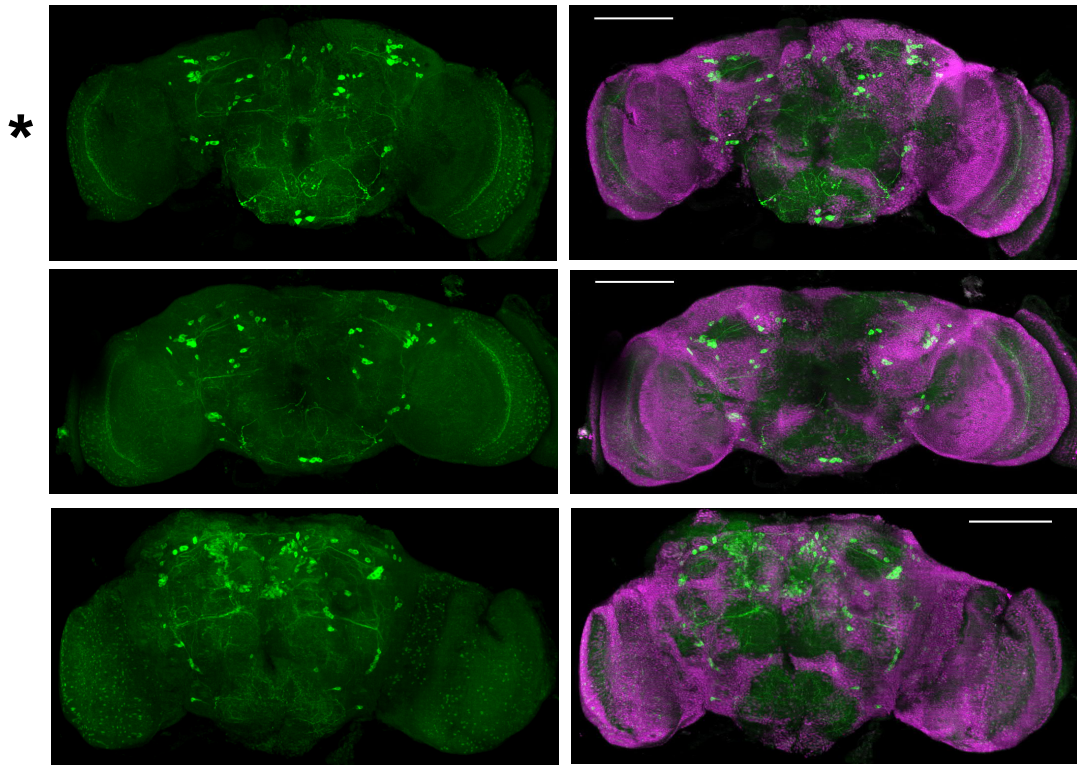

R51C09>Dcr2 only

TH

Elav

Yalgin et al, Figure S38

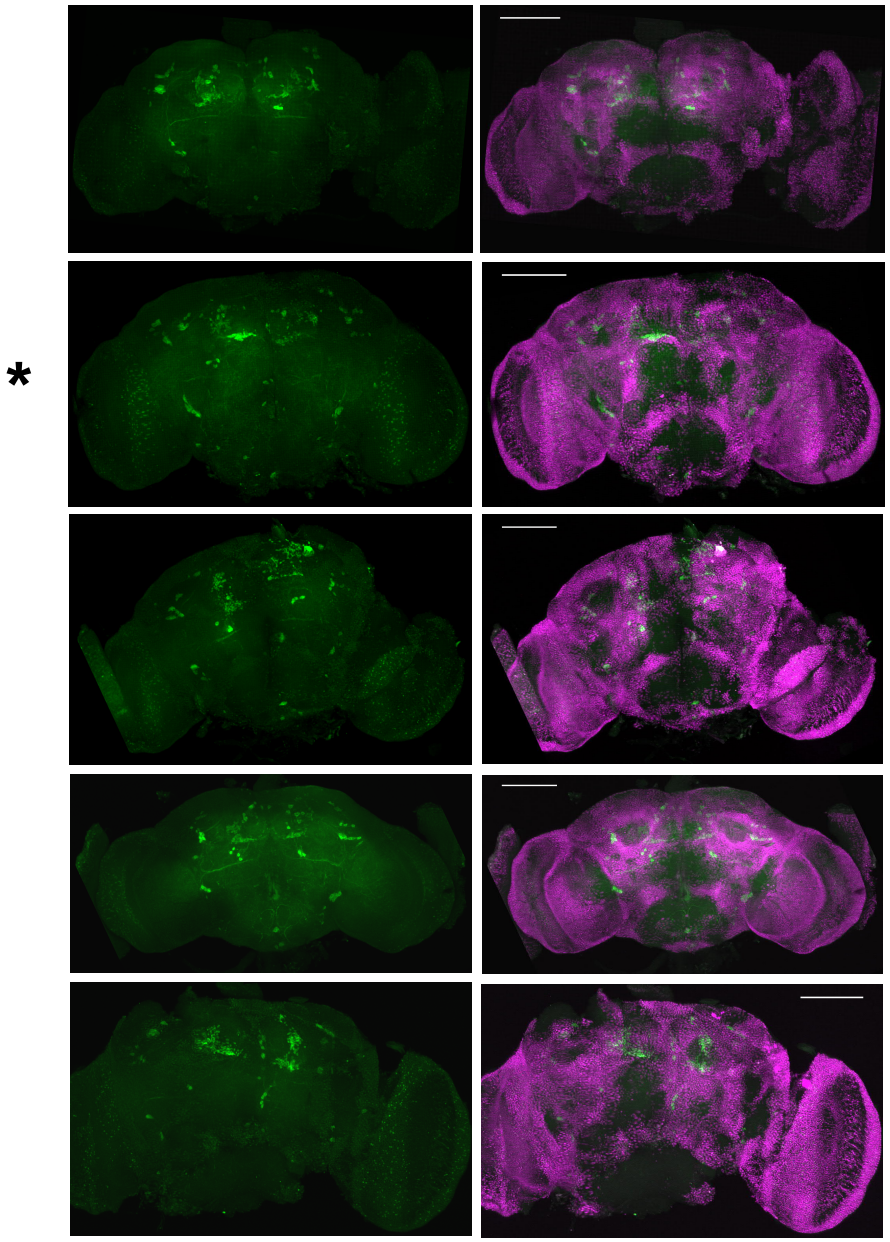

*

R51C09>COX7A-KD

TH

Elav

Yalgin et al, Figure S39